University of Bergamo
Department of Engineering and Applied Sciences

Elastoplastic fracture behaviour of pipeline steels in hydrogen embrittlement promoting environments

electrochemical, gaseous, and mechanical interactions governing hydrogen embrittlement

Academic Supervisors:

Prof. Marina Cabrini

Prof. Tommaso Pastore

Doctoral Dissertation of:

Luca Gritti

ID: 1034920

Industrial Supervisor:

Eng. Luca Bacchi
(Snam Rete Gas)

PhD Cycle: XXXVIII

Academic Year: 2024/2025

To all those who have supported me throughout this journey,
with my sincere gratitude.

Declaration

I hereby declare that except where specific reference is made to the work of others, the contents of this dissertation are original and have not been submitted in whole or in part for consideration for any other degree or qualification in this, or any other university. This dissertation is my own work and contains nothing which is the outcome of work done in collaboration with others, except as specified in the text and Acknowledgements.

Gritti Luca
February 2026

Acknowledgements

I would like to express my sincere gratitude to all those who have supported me throughout the course of my doctoral research.

First and foremost, I am deeply grateful to my supervisors, *Marina Cabrini* and *Tommaso Pastore*, for their continuous support, encouragement, and guidance. Their insightful advice, critical perspectives, and constant motivation have been essential in helping me navigate the complexities of research and develop ideas independently and rigorously. I am also grateful to *Sergio Lorenzi* for his constructive feedback and for introducing me to laboratory work during my Master's thesis.

I would like to acknowledge the *Department of Engineering and Applied Sciences* at the *University of Bergamo* for providing an excellent research environment. I am particularly grateful for the financial support provided by *SNAM Rete Gas*, and to *Luca Bacchi* for his invaluable assistance, without which this project would not have been possible.

I am also grateful to the *University of Manchester*, where I had the opportunity to carry out part of the experimental work. In particular, I am grateful to *Fabio Scenini* for welcoming me into his research group and for his constant support and guidance throughout my stay.

My sincere thanks go to my colleagues and new friends in the *MaSTeR Lab – Materials Science and Technology Research Laboratory*, with whom I have shared both scientific and non-scientific discussions. Their perspectives, enthusiasm, and friendship have enriched my experience and lightened even the heaviest or most monotonous days. I would also like to thank all my friends who have stood by me, offering kind words whenever needed, whether through words of encouragement or a simple shared joke.

Finally, my heartfelt gratitude goes to *my family*. I am profoundly thankful for their love, patience, and belief in me; their support has been a constant source of strength. I would also like to thank *Sara*, who has always stood by me, in the best of times as well as in the most challenging ones, and who continues to do so.

Preface

The aim of this thesis is to evaluate the behaviour of pipeline steels under hydrogen exposure, introduced both electrochemically and from the gas phase, with a focus on characterising the hydrogen diffusion parameters and the fracture propagation.

Chapter 1 describes the issues related to hydrogen compatibility, framing the problem within the existing literature and assessing the microstructural effects that control hydrogen uptake under both electrochemical and gas charging. These parameters are essential for understanding how hydrogen interacts with the material when mechanical loading acts synergistically with hydrogen ingress, as further discussed in the literature review of Chapter 2.

The experimental section begins with Chapter 3, which introduces the materials employed in this study, together with a description of the environments used to charge the samples either by cathodic polarisation or by exposure to hydrogen gas.

Chapter 4 focuses on the analysis of the apparent hydrogen diffusion coefficient and hydrogen concentration, describing both the experimental setup and the data-driven model developed to estimate the diffusible hydrogen content.

This information is essential for assessing the conditions under which spontaneous hydrogen desorption occurs at room temperature and atmospheric pressure over time, as discussed in Chapter 5. In this chapter, the model predictions are compared with permeation experiments, evaluating the effect of the applied cathodic overpotential. These measurements are then correlated with the equivalent hydrogen pressure corresponding to the same charging concentration. The validity of this relationship is further assessed by applying the data-driven optimisation model to hydrogen gas–charging experiments.

Finally, Chapter 6 investigates the mechanical behaviour during slow plastic deformation, assessed through J-integral tests performed in the presence of hydrogen. The fracture mechanics results obtained under electrochemical hydrogen charging are correlated with those from gas-phase charging, enabling an evaluation of crack-growth behaviour under different strain rates and charging conditions.

In Chapter 7, these effects are further analysed and compared for both materials to understand how hydrogen influences crack-propagation rates.

Abstract

The reduction of atmospheric emissions can be pursued through several approaches, such as CO_2 storage and the adoption of new solutions based on alternative energy carriers, for example green hydrogen produced from renewable sources. Owing to its potentially low cost, the direct transport of hydrogen in the current pipeline network may become attractive, provided that material compatibility is guaranteed.

The presence of atomic hydrogen within the metal lattice can induce hydrogen embrittlement phenomena in steels. Atomic hydrogen may be generated by electrochemical reduction under external cathodic protection, which is employed to prevent generalised corrosion of pipelines, or by the dissociation of hydrogen gas inside the pipe. Once absorbed, hydrogen is in the atomic state and can diffuse through the material lattice, and its effects are independent of the source. In any case, there is no reasons for assuming that hydrogen originating from electrochemical processes behaves differently from hydrogen introduced in the gaseous state. Methods used to quantify the amount and characteristics of hydrogen absorbed in metals include permeation tests performed with the Devanathan–Stachurski cell, as well as tests to measure hydrogen uptake in the material. It is therefore possible to correlate electrochemically introduced hydrogen with gaseous hydrogen by estimating an equivalent pressure –derived using Sieverts' law– corresponding to the hydrogen uptake achieved under cathodic polarisation.

However, pipeline steels are generally considered immune to hydrogen embrittlement. More than fifty years of experience have shown that cathodically protected gas pipelines do not experience hydrogen-induced failure. Nevertheless, failures have occurred when slow plastic deformation has been present. Only the synergistic effect of slow plastic strain and continuous hydrogen supply (whether gaseous or electrochemical under cathodic polarisation) can promote hydrogen embrittlement. This particular condition can be studied using slow strain rate tests with in-situ charging. However, to realistically simulate the behaviour of a defect that could propagate longitudinally along the pipe, which is the most critical scenario, an elastoplastic fracture mechanics

approach with in-situ charging is required. This approach enables realistic simulation of service conditions and the identification of defect sizes, propagation conditions, and crack growth rates. Knowledge of this allows informed and practical intervention. Defects can be monitored and their location determined, enabling appropriate and targeted maintenance actions.

This doctoral thesis evaluates the behaviour of hydrogen in two pipeline steels subjected to electrochemical charging under cathodic protection and overprotection conditions, as well as to gaseous hydrogen charging. The study focuses on parameters characterising hydrogen diffusion processes: the apparent diffusion coefficient and hydrogen uptake. These were estimated by developing a data-driven optimisation model, which also enabled the evaluation of spontaneous desorption under room temperature and atmospheric pressure. The results were compared with permeation tests to assess the influence of surface conditions on hydrogen diffusion behaviour and on cathodic potentials. By applying Sieverts' law, an equivalent pressure was estimated as a function of the applied potential for a given hydrogen uptake. This information was then used to define a characteristic pressure for gaseous hydrogen charging tests. The results were validated through gas-phase hydrogen uptake tests, in which the hydrogen content was measured.

Once the level of cathodic polarisation and the total pressure of gaseous hydrogen required to introduce a comparable amount of atomic hydrogen into the metal had been assessed, elastoplastic fracture mechanics tests with both electrochemical and gaseous hydrogen charging were carried out on the two steels. The corresponding crack propagation mechanisms and effects were correlated using the J-integral approach. The analysis was extended to assess the mechanical and geometric characteristics of defect propagation. Crack growth rates and crack-tip strain rates were evaluated to correlate all tests conducted under all conditions. This enabled the introduction of a parameter describing susceptibility to hydrogen-assisted defect propagation, allowing the assessment of how hydrogen influences crack growth under the various conditions and in the different materials studied.

- Renewable energy;
- Discontinuous energy supply;
- Energy surplus

- Electrolyzer;
- Producing H_2 with water electrolysis

- Transport H_2 in currently pipelines present in the territory;
- Blending with methane

COMPATIBILITY & QUALIFICATION

COMPATIBILITY between hydrogen and pipeline materials;

QUALIFICATION of materials;

Define parameters about Hydrogen Embrittlement

Pipeline steels are immune to HE under cathodic protection in normal operating conditions;

material sensitivity · promoting environment · mechanical stress · HE

Mechanism of entry and diffusion of hydrogen

Identification of the critical concentration of hydrogen for HE;

From pipeline:
- Steel A
- Steel B

Effect of stress on hydrogen absorption;

Data-Driven Model

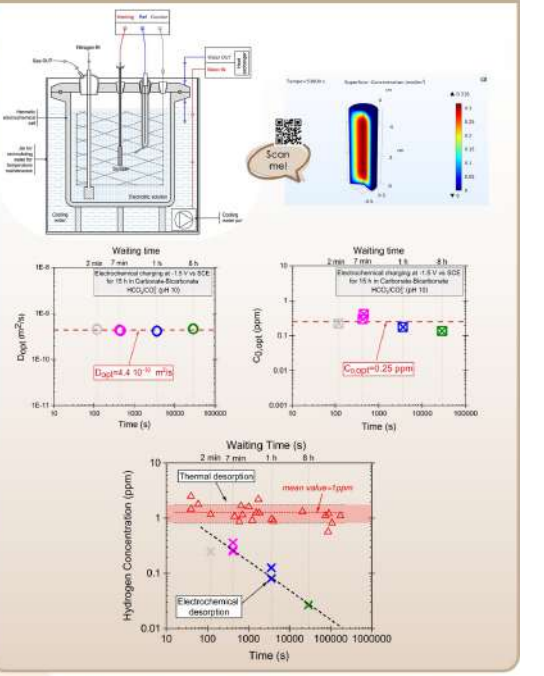

Permeation

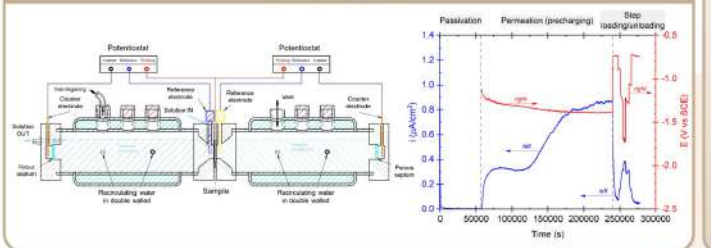

Mechanical Fracture Tests

Sievert's law

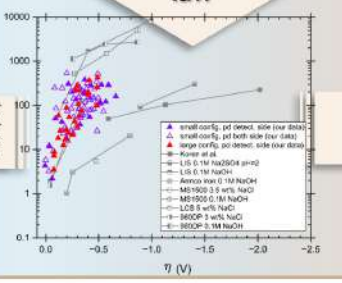

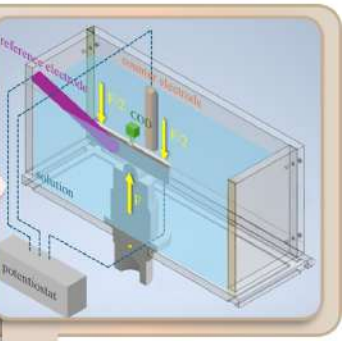

Gas Charging

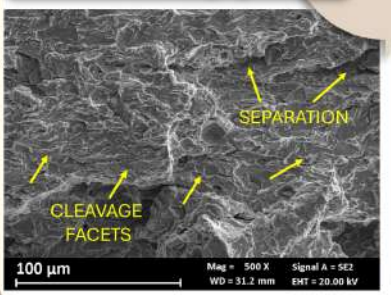

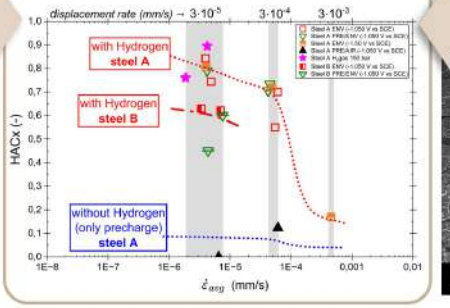

Cathodic Charging

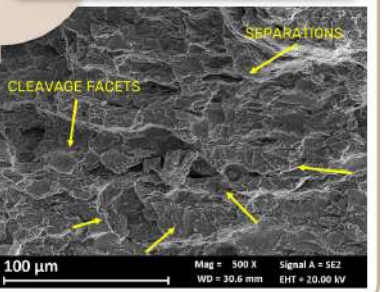

Table of contents

List of figures

List of tables

Nomenclature

Roman symbols

a_{final}	Crack length after pre-cracking
a_{initial}	Crack length at the end of the mechanical test
a_i	Crack length at the i-th cycle
B	Thickness of the specimen in a mechanical fracture test
$\hat{C^*}$	Dimensionless concentration, adjusted for passivity contribution
C_0	Concentration in equilibrium condition - hydrogen uptake
C_0^*	Homogeneous Hydrogen concentration (initial)
C_{res}	Residual Hydrogen concentration in the sample
C_{res}^*	Average residual Hydrogen concentration in the sample
C_s	Superficial Hydrogen concentration
CLL	Compliance in a mechanical fracture test
D	Apparent diffusion coefficient
D_{opt}	Diffusion coefficient optimised via Matlab
da/dt	Crack growth rate
E	Young's modulus
E_0^H	Equilibrium Potential
E_c	Electrochemical Potential
E_0	Standard potential
E_{appl}	Electrode potential applied
E_{eq}	Equilibrium potential
f_{eq}	Equivalent fugacity of electrochemical hydrogen corresponds to an equivalent hydrogen pressure at the metal surface
f_{H_2}	Hydrogen Fugacity
$\tilde{i}$	Normalised permeation transient current density
I	Current measured
i_0	Initial value of hydrogen permeation current density
i_∞	Permeation steady-state current density
I_{adj}	Current, adjusted for passivity contribution
I_{pass}	Passivation current
J	Energy for crack propagation
J_{el}	Elastic component of energy for crack propagation
J_{pl}	Plastic component of energy for crack propagation
J_Q	Initiation energy for crack propagation
K	Stress intensity factor
K_{JQ}	Stress intensity factor at J_Q initiation

L	Thickness of the sheet for permeation test
M_∞	Mass estimate in the steady-state condition
M_{Hadj}	Mass of Hydrogen, value adjusted
M_{res}	Residual Hydrogen mass in the sample
M_{sample}	Sample mass
p	Partial pressure of hydrogen gas
P_i	Load during the i-th cycle of the mechanical test
Q_{Hadj}	Charge of Hydrogen, value adjusted
r_p	Plastic radius
S	Sievert constant
Sp	Span of the SE(B) specimen
$\hat{T}$	Dimensionless time
W	Width of the specimen in a mechanical fracture test
X	Vertical crosshead displacement

Greek symbols

α	Total rotation angle of mechanical specimen
α_p	Plastic component of α
Δa_i	Crack growth during the i-th cycle
ΔC_H	Concentration difference across the sheet in the permeation tests
δ	CTOD (Crack Tip Opening Displacement)
$\dot{\varepsilon}_{(\delta)}$	Strain rate estimated from CTOD
$\dot{\varepsilon}_{(\gamma)}$	Strain rate estimated from CTOA
η	Overpotential
γ	Half CTOA (Crack Tip Opening Angle)
ν	Poisson's ratio
σ_{uts}	Ultimate tensile strength
σ_{ys}	Yield strength
θ	Fraction of surface covered by hydrogen
φ	Outflow flux of hydrogen

Abbreviations/Acronyms

BC	Boundary Conditions
COD	Crack Opening Displacement
CTOA	Crack Tip Opening Angle
CTOD	Crack Tip Opening Displacement
FEM	Finite Element Method
HACx	Hydrogen Assisted Crack Index
HAZ	Heat Affected Zone
HER%	Hydrogen Embrittlement Ratio (%)
HER	Hydrogen Evolution Reaction
HE	Hydrogen Embrittlement
IC	Initial Conditions
MILD	Moderate or Intense Low-oxygen Dilution
OCP	Open Circuit Potential
SCE	Saturated Calomel Electrode

Chapter 1

Hydrogen compatibility and diffusion in pipeline steels

This chapter outlines the role of hydrogen in the energy transition and examines the challenges associated with its use, particularly the problem of compatibility of hydrogen with existing pipeline steels. The discussion is framed within the current scientific literature and evaluates the microstructural factors that govern hydrogen uptake under both electrochemical and gaseous charging conditions.

1.1 Integrating hydrogen into the decarbonisation strategy

The continuous growth in global energy demand, coupled with the worsening of environmental issues, has led to the establishment of international agreements aimed at limiting and reducing carbon dioxide (CO_2) emissions into the atmosphere. The United Nations Paris Agreement set the ambitious goal of controlling the rise in the average global surface temperature of the Earth [1]. To achieve this target, global CO_2 emissions (GCE) must be reduced by 50–85% compared to the emission levels of the year 2000 [2, 3], in order to counteract the opposing international trend shown in Figure 1.1 [4].

There are various strategies to reduce CO_2 emissions, such as Carbon Capture Utilisation and Storage (CCUS), as well as the introduction of new clean energy

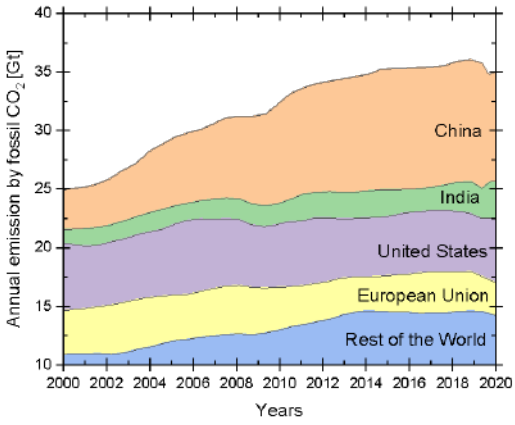

Figure 1.1: Global CO_2 emissions from fossil fuels by regions, 2000–2021 adapted by [4].

carriers, like hydrogen, aimed at limiting the release of fossil fuel-derived emissions into the atmosphere.

CCUS, involves capturing carbon dioxide directly from the exhaust streams of industrial processes, thereby preventing its emission into the atmosphere. Once captured, the CO_2 is compressed into a fluid state to facilitate transportation. In this form, it can be utilised in Enhanced Oil Recovery (EOR) or permanently stored in geological formations, such as depleted oil and gas reservoirs. A critical aspect of the CCUS chain is the safe and efficient transport of CO_2 to utilisation or storage sites, ensuring that the gas is either securely sequestered or effectively repurposed without re-entering the atmosphere.

Nevertheless, the most promising and forward-looking strategy involves the integration of new energy carriers, most notably hydrogen, to progressively replace natural gas. According to the literature, experimental findings indicate that increasing the hydrogen content significantly affects combustor stability. However, there are different combustion regimes that respond differently to hydrogen addition. One such regime is MILD (Moderate or Intense Low-oxygen Dilution) combustion, which demonstrates stable operation across a wide range of hydrogen concentrations, from pure methane to pure hydrogen, highlighting its notable fuel flexibility and adaptability under MILD conditions [5]. Hydrogen addition may reduce the oxygen reaction rate, which is advantageous for achieving and sustaining MILD combustion. In other words, MILD combustion exhibits higher thermal efficiency when fuelled with hydrogen rather than

methane [6]. These characteristics make hydrogen a highly promising fuel for advanced low-emission combustion systems, positioning it as a key contributor to the energy transition.

However it does not naturally occur in its pure form and must be produced through various technologies. It is most commonly obtained for industrial use from natural gas via a thermochemical conversion process that generates CO_2, resulting in what is known as *grey* hydrogen. By incorporating carbon capture and storage technologies into this process, it is possible to produce low-carbon or *blue* hydrogen. Another method of hydrogen production is electrolysis, in which electricity is supplied to an electrolytic cell to split water molecules, producing hydrogen in a sustainable manner without releasing carbon dioxide, thus generating *green* hydrogen [7–9]. This latter approach to hydrogen production, aimed at converting surplus energy that cannot be absorbed by the electrical infrastructure, may prove to be a promising solution. At present, only around 4–5% of global hydrogen is produced in this way. However, the abundant availability of renewable energy in Northern Europe, combined with targeted financial policies and investment in the sector, could significantly accelerate the development of this technology and support the energy transition. Hydrogen, used as an alternative energy carrier, can subsequently be utilised to generate electricity via fuel cells or directly employed in combustion processes to aid in reducing emissions (MILD combustion).

1.2 Towards the qualification of compatibility in existing pipelines

For the introduction of hydrogen into the energy chain to be advantageous, it must be economically competitive with other technologies. To maintain low costs, the strategy involves transporting it directly through the existing pipeline network, as constructing a dedicated hydrogen transport infrastructure would be too expensive. Moreover, the current gas distribution system is widespread across the territory. Thus, the idea is to inject hydrogen into the existing pipeline network, possibly starting with hydrogen-enriched methane blends [10]. The transmission of hydrogen gas through metallic pipelines has been practiced worldwide for more than 80 years. By 2012, around 3200 km of hydrogen transmission pipelines were in use, operating at pressures of up to 10 MPa [11]. Numerous engineering standards and technical guidelines have been established for components involved in hydrogen transport and storage [11], and extensive research has been dedicated to evaluating the practicality of injecting

hydrogen into existing natural gas pipelines made of carbon steel [7, 12–16]. Among the relevant projects, the HIGGS initiative (H2020 GA 875091) assessed the feasibility of hydrogen injection into carbon steel pipelines by analysing the infrastructure of the European gas transmission network [17]. Ensuring compatibility between this emerging energy carrier and the existing infrastructure is essential to support a safe and efficient energy transition [18].

It is well established in the literature [19–26] that metals in contact with hydrogen sources may undergo changes in their mechanical properties and may be susceptible to a phenomenon generally known as *hydrogen degradation*.

1.3 Hydrogen embrittlement in pipeline materials: onset and root causes

Hydrogen-assisted mechanical degradation of structural materials represents one of the most complex forms of metallic degradation, primarily due to the introduction of numerous unknowns in the kinetics of the degradation process compared to hydrogen free environments. The presence of hydrogen can significantly compromise the mechanical performance of metallic materials, including steels, potentially leading to premature failure [11, 27].

Consequently, a range of hydrogen-induced damage mechanisms are commonly observed in industrial components exposed to hydrogen. The term *hydrogen damage* is widely used as a general descriptor encompassing various degradation phenomena and mechanisms arising from the interaction between hydrogen and metals. These include mechanical degradation processes facilitated by hydrogen, environmentally assisted failures, microstructural transformations, and other hydrogen–material interactions. However, there remains considerable vague aspects regarding the classification and fundamental nature of individual hydrogen damage mechanisms [11, 28–31].

Hydrogen embrittlement (HE) is one of the most recognised forms of hydrogen-induced damage. It refers to the deterioration of mechanical properties, such as reduced ductility and tensile strength, often resulting in decreased fracture toughness and the initiation of sub-critical cracking due to dissolved hydrogen. HE in iron, steel, and their alloys is of particular concern, given their widespread industrial applications. Despite extensive research efforts, no comprehensive and practically applicable predictive physical model for HE currently exists [32–35]. This is supported by numerous studies worldwide that confirm the complexity and variability of the phenomenon. Several mechanisms have been proposed to explain the observed forms of hydrogen

embrittlement [20, 32–36]. However, hydrogen embrittlement phenomena share the common feature of developing under specific conditions, as illustrated in Figure 1.2.

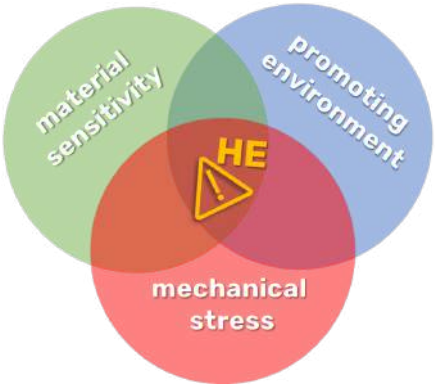

Figure 1.2: Diagram of the synergistic effects necessary for the development of hydrogen embrittlement (HE) in metallic systems.

It is well-established in the literature [16, 37–41] that the manifestation of HE requires the synergistic interaction of three critical factors: the material's susceptibility, a hydrogen-promoting environment, and the presence of slow mechanical loading. The simultaneous occurrence of all three conditions is essential for the initiation and propagation of hydrogen embrittlement. As a result, a multidisciplinary approach incorporating advanced experimental techniques, theoretical modelling, elastic and elastic-plastic fracture mechanical analysis, macro and micro scale investigations, atomistic adsorption simulations, is often employed to improve understanding of the complex and often concurrent mechanisms involved in HE [20, 33–35].

Consequently, determining the root causes of hydrogen embrittlement in real-world applications remains a complex task. In the current pipeline infrastructure, all three synergistic factors are present. Direct hydrogen transport through pipelines raises concerns regarding hydrogen embrittlement, as the pipelines are subjected to a hydrogen-rich environment. Additionally to protect against corrosion, these pipelines are often equipped with a cathodic protection system. As a result, hydrogen generated through the electrochemical reduction of water in the surrounding soil contributes to overall hydrogen ingress by diffusing into the pipe wall, which can then penetrate the metal lattice and compromise its mechanical properties.

Moreover buried pipelines, are subject to significant and sustained stress due to factors such as ground movement, bradyseism or artificial tunnelling beneath the pipeline alignment, potentially leading to changes in its trajectory [42]. Ground movement

causes axial loads in the pipeline, which gradually decrease as the surrounding soil resists the movement outside the deformation zone. In these unaffected areas, the pipeline layout often includes bends, joints, or connections to equipment and other components, which typically offer lower resistance to axial loading than straight sections of pipe. These features modify the stress distribution both within the affected section and along the length of the pipeline [43]. The slow, continuous, and non-perfectly static soil loading acts as a second key factor in the development of HE phenomena long the pipes.

However, although the conditions that promote hydrogen embrittlement are present, the metals commonly used in pipeline construction are generally considered to be highly resistant (or even immune) to HE under such conditions. This is supported by over 50 years of monitoring data from pipelines protected by cathodic protection systems, with no reported incidents specifically attributed to hydrogen generated by this method. Nevertheless, it remains important to investigate the introduction of hydrogen gas in the current context could alter this condition, in order to ensure material compatibility and support a safe energy transition.

1.3.1 Comparative investigation of hydrogen entry: electrochemical vs gaseous environments

Hydrogen may be present on both the external and internal surfaces of a pipeline, arising from electrochemical water reduction associated with cathodic protection or from the dissociation of transported gas, respectively. In both cases, hydrogen atoms produced by electrochemical reactions or by molecular dissociation can enter the steel and subsequently diffuse through the lattice. Their presence reduces the material's plasticity and strength and may ultimately promote cracking or even brittle failure [44–46].

However, hydrogen introduced into steel via electrochemical reactions is generally assumed to behave identically to hydrogen introduced from a gaseous environment. There is no theoretical basis to suggest that hydrogen retains any dependency on the production process that would influence its interaction with the metal. Consequently, hydrogen generated through electrochemical processes is expected to exhibit the same effects as hydrogen absorbed from a gaseous phase. Conducting investigations under conditions that closely replicate real service environments is essential for applying existing expertise, derivates by cathodic protection, and predicted the behaviour in high-pressure gaseous exposure establishing a correlation of two environments. Thus it may be possible to leverage the cathodic protection knowledge under these conditions

to study the long-term behaviour of metals in the presence of hydrogen. Moreover electrochemical cathodic charging represents a more accessible and controlled method for investigating hydrogen-related phenomena.

Therefore, it is interesting a comparative investigation of hydrogen phenomena induced by gaseous hydrogen exposure and those induced via electrochemical charging. The equivalence of hydrogen production by both methods can be considered valid at room temperature, provided that each results in the same level of hydrogen activity within the steel near its surface during the charging process. Several studies [47–49] explored this equivalence under conditions of constant potential and identical temperature.

Hydrogen gas-metal interaction

In the interaction between hydrogen and metal, where the metal surface is directly exposed to the gas phase, hydrogen dissolves into the metal. This dissolution process involves four distinct stages as shown in Figure 1.3: physical adsorption (*physisorption* Equation (1.1)), chemical adsorption (*chemisorption* Equation (1.2)), surface penetration (*absorption* Equation (1.3)), and bulk diffusion in Equation (1.3). Initially, hydrogen gas molecules migrate towards the metal surface and undergo physisorption, driven by weak van der Waals forces acting between the hydrogen atoms and the metal ions within the matrix. Subsequently, during chemisorption, dissociation of the hydrogen molecules occurs as a result of stronger chemical interactions between the gas and the solid surface. Hydrogen atoms that successfully overcome the energy barrier at the surface are then absorbed into the metal. Once inside, these atoms diffuse through the metal lattice [50].

$$H_{2(gas)} \rightleftharpoons H_{2(ads)} \quad ① \quad \text{Physical adsorption} \tag{1.1}$$

$$H_{2(ads)} \rightleftharpoons 2H_{(ads)} \quad ② \quad \text{Chemical adsorption} \tag{1.2}$$

$$2H_{(ads)} \rightleftharpoons 2H_{(abs)} \quad ③ \quad \text{Absorption} \tag{1.3}$$

$$2H_{(abs)} \rightleftharpoons 2H_{(diff)} \quad ④ \quad \text{Diffusion} \tag{1.4}$$

In some cases, hydrogen atoms may penetrate the topmost atomic layer of the metal and occupy sub-surface potential wells. These sites are energetically intermediate between pure surface adsorption and bulk absorption. Structural defects and impurities within the metal surface introduce a variety of adsorption sites, influencing the adsorption process. There is broad agreement in the literature that surface impurities

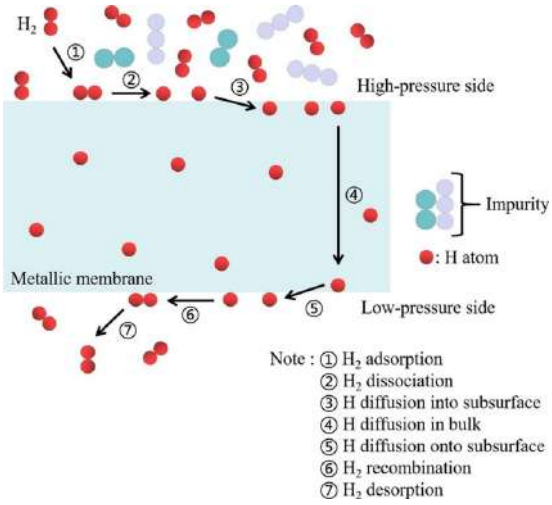

Figure 1.3: Schematic representation of hydrogen gas interaction with a metallic sheet from [50].

significantly alter the adsorption dynamics. Gaseous contaminants can block dissociation sites and compete with hydrogen for adsorption, even at very low concentrations. As a result, more reactive species such as O_2 and CO can substantially inhibit hydrogen uptake and thereby reduce the risk of hydrogen embrittlement [51].

Penetration of hydrogen atoms through the surface can lead to accommodation of hydrogen under the surface, which is often referred to as "sub-surface adsorption". Figure 1.4 shows the variation of potentials for two separate hydrogen atoms and the hydrogen molecule near the gas-solid interface.

A potential minimum beneath the surface is typically present and differs from both the potential in the bulk metal and that in the vacuum region far from the surface. This intermediate potential can be interpreted as sub-surface chemisorption. When a hydrogen molecule is located far from the surface, it remains electrically neutral. However, if the tails of its molecular orbitals extend sufficiently close to the Fermi level of the metal surface, electron tunnelling occurs, allowing metal electrons to populate the molecule's antibonding orbitals. This results in the weakening of the internal H–H bond and causes a broadening and downward shift of the molecular orbital energies, bringing them below the Fermi level of the metal. At this stage, the molecule enters a chemisorbed molecular state, in which the covalent H–H bond is weakened but not fully broken. Dissociation requires additional energy to overcome the activation barrier, leading to the formation of individual chemisorbed hydrogen atoms. Following

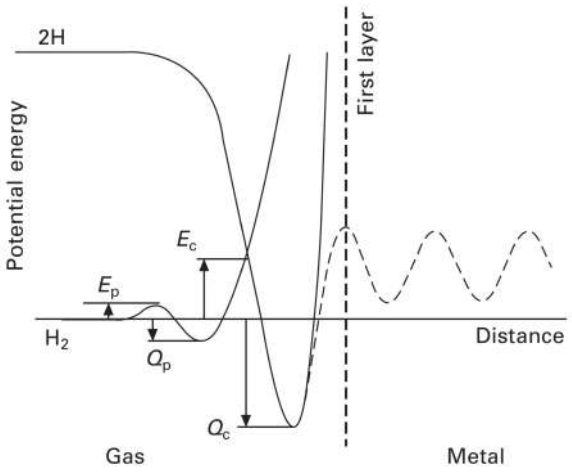

Figure 1.4: Potential energies of two free atoms and a molecule near the gas-solid interface. The classic Lennard-Jones diagram [52] is gives by solid lines. The dashed line gives the potential energy of an atom passing through the metal surface. E_p and E_c are the activation energies for physical adsorption of the molecule and chemical adsorption of two dissociated atoms, while Q_p and Q_c are the heat of adsorption of molecules and atoms, respectively [53]

dissociation, the electrons of the two hydrogen atoms interact independently with the metal substrate, each forming a separate chemical bond with the surface [53].

Hydrogen electrochemical-metal interaction

The interaction of hydrogen produced by electrochemical processes is complex and depends on the specific environment considered. In this case, additional parallel reactions may occur, which differ from the mechanism typically observed for gaseous hydrogen. To simulate the real-world conditions of pipeline under cathodic protection, the electrochemical processes considered in this case involve in alkaline environment. It is applied a cathodic potential through the water naturally present in the the soil as the electrolyte solution. This environment is usually near-neutral but can become alkaline under overprotection conditions, especially when coating defects allow stagnant water to accumulate. This localised environment can become increasingly alkaline due to the hydrogen evolution reaction (HER) described in Equation (1.5).

$$2H_2O + 2e^- \rightarrow H_2 + 2OH^- \tag{1.5}$$

Under cathodic hydrogen charging conditions, it is possible to correlate the electrochemical potential E_c and hydrogen activity (corresponding to fugacity f_{H_2}) as described in the literature [47, 54–57]. The relationship between hydrogen fugacity and the applied cathodic overpotential is given by:

$$f_{H_2} = A \cdot \exp\left(\frac{-\eta F}{\zeta RT}\right) \tag{1.6}$$

where: A and ζ are constants dependent on the hydrogen evolution mechanism and must be derived through iterative approaches [58], T is the temperature, F is the Faraday constant, R is the universal gas constant, η is the applied overpotential. The overpotential η is defined as:

$$\eta = E_c - E_0^H \tag{1.7}$$

The equilibrium potential E_0^H is given by the Nernst equation:

$$E_0^H = -0.059 \cdot \mathrm{pH} \tag{1.8}$$

The overall reaction of hydrogen evolution on a metal surface, as described in Equation (1.5), can be further examined through a series of elementary steps outlined

in Equations (1.9) to (1.11), as reported in the literature [47, 59–63] and summarised in the Figure 1.5.

$$H_2O + M + e^- \rightarrow MH_{ads} + OH^- \quad \text{(A)} \tag{1.9}$$

$$2MH_{ads} \rightarrow H_2 + 2M \quad \text{(B)} \tag{1.10}$$

$$MH_{ads} + H_2O + e^- \rightarrow H_2 + OH^- + M \quad \text{(C)} \tag{1.11}$$

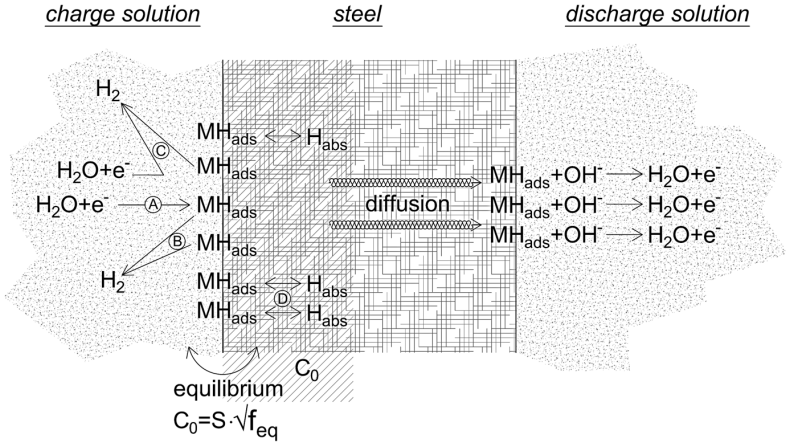

Figure 1.5: Representation of electrochemical reactions of steady-state of hydrogen charging in alkaline environment on sheet steel metal.

As illustrated in Figure 1.5, Equation (1.9) describes the electrochemical discharge of hydrogen from a water molecule at the metal surface (M), resulting in the formation of a hydrogen atom adsorbed onto the metal surface, denoted as MH_{ads}. This step, known as the *indirect mechanism* [64] , involves the initial adsorption of hydrogen on the electrode surface via the Volmer reaction. This contrasts with the *direct hydrogen absorption* pathway, in which hydrogen protons are directly reduced and incorporated as subsurface absorbed hydrogen [65–68]. The indirectly absorption is typically occurs is associated at conditions of low overpotential [59, 69–71]. The adsorbed hydrogen atom is mobile on the metal surface and may migrate until it encounters another adsorbed hydrogen atom (pathway B in Figure 1.5). These two atoms can subsequently recombine via Equation (1.10) to form a hydrogen molecule, which then desorbs from the surface as molecular hydrogen (H_2), entering the gaseous phase as bubbles that

detach from the metal surface. As the surface coverage by hydrogen increases, the probability of electrochemical desorption via Equation (1.11) also increases. Under such conditions, the adsorbed hydrogen atoms can leave the metal surface through either of the two mechanisms described by Equations (1.10) and (1.11). It is important to note that the overall reaction represented by the combination of Equations (1.9) and (1.10) is equivalent to that of Equation (1.5). Likewise, the combination of Equations (1.9) and (1.11) also yields the same net reaction as Equation (1.5). However, the adsorbed hydrogen (MH_{ads}) can also be absorbed into the metal lattice to form MH_{abs} according to the equilibrium in Equation (1.12) and diffusing in the metal lattice (pathway *D* in Figure 1.5).

$$MH_{ads} \rightleftharpoons MH_{abs} \tag{1.12}$$

Application of Sievert's law to gaseous and electrochemical hydrogen ingress

When hydrogen is dissolved in the sublayer of the metal lattice, it can accumulate to a certain concentration, denoted as C_0. Under equilibrium conditions, this concentration can be evaluated using Sievert's law:

$$C_0 = S \cdot \sqrt{f_{eq}} \tag{1.13}$$

where S is the Sievert constant, representing the hydrogen hydrogen uptake in the material at equilibrium [72], f_{eq} is the hydrogen fugacity at equilibrium.

Regrettably, the Sievert constant S shows considerable variability across the literature, as summarised in Table 1.1. Furthermore, many of the reported values do not accurately represent the actual state of the material, thereby introducing additional uncertainty and limiting the applicability of this relation.

Table 1.1: Literature value of Sievert constants (S).

Material	Sievert Constant (S)		Temperature	Ref.
	Value	Unit		
Plain Carbon Ferritic Steels	41.98 – 202.4 13.28 – 64.00	$mol/(m^3\sqrt{MPa})$ $mol/(m^3\sqrt{bar})$	500–900 K	[72]
3.5NiCrMoV steel	$1.511 \cdot 10^{-6}$ $2.72 \cdot 10^{-2}$	$mol/(m^3\sqrt{bar})$ $wppm/\sqrt{bar}$	–	[73]
X65 steel	$1.25 \cdot 10^{-2}$	$wppm/\sqrt{bar}$	–	[74]
Pure Iron (ref.)	$5.3 \cdot 10^{-4}$	$wppm/\sqrt{bar}$	–	[75]
Pure Iron (ref.)	$3.8 \cdot 10^{-3}$ $2.96 \cdot 10^{-2}$	$mol/(m^3\sqrt{atm})$ $wppm/\sqrt{bar}$	25°C	[58, 73]

In fact, the applicability of Sievert's law in Equation (1.13) is limited by the range of pressures over which it remains valid. At sufficiently high pressures, the behaviour of the gas deviates from ideality, as illustrated in Figure 1.6. Under such conditions, the pressure term must be replaced by the fugacity f_{H_2}, which is related to the pressure through the Abel–Noble equation of state (Equation (1.14)) [76].

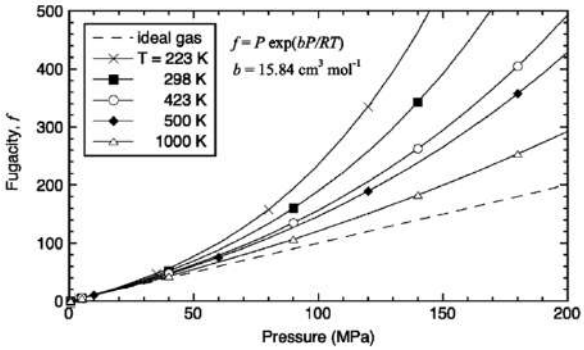

Figure 1.6: Correlation between pressure and fugacity of hydrogen from [77].

$$f_{H_2} = p\, e^{\left(\frac{pb}{RT}\right)} \tag{1.14}$$

p is the pressure, b is the molar volume parameter usually equal to 15.84 cm^3/mol, T is the temperature, and R is the universal gas constant [77]. Thus, Figure 1.6 illustrates the fugacity of hydrogen as a function of pressure for different temperatures. For instance, at 273 K and a pressure of 200 MPa (2000 bar), the fugacity is approximately four times the applied pressure, emphasising the importance of fugacity corrections at high pressures. Consequently, the equilibrium fugacity f_{eq} may be considered equivalent to the hydrogen partial pressure only at relatively low pressures (typically $\lesssim$ 30 MPa=300 bar) [77]. Under these conditions, it becomes feasible to relate the hydrogen concentration obtained through cathodic charging to an equivalent hydrogen pressure.The pressure dependence tends to become linear (and essentially coincident with the fugacity) because the active surface is no longer fully covered by the gas. This behaviour is consistent with the theoretical Langmuir chemisorption model described in Equation (1.15).

$$\theta = \frac{pb}{1+bp} \tag{1.15}$$

θ is fraction of surface covered, p is the hydrogen pressure and b a constant. Adsorption on the surface is a preliminary step preceding the absorption of gases into the bulk of solids. This process occurs exclusively at the gas–solid interface, within a region typically only a few nanometres thick [53].

1.4 Influence of microstructure on hydrogen diffusion and uptake in typical pipeline steel

Pipeline steels exhibit a range of microstructures depending on their manufacturing processes. Ferrite/pearlite microstructures with varying grain sizes are typically produced via hot rolling of steel plates. More complex microstructures—such as acicular ferrite, fine pearlite, bainite, and martensite—can develop during hot rolling combined with accelerated cooling. In the case of seamless pipes, normalization is commonly applied, yielding ferritic and fine pearlitic structures. Alternatively, oil quenching followed by tempering can produce a tempered martensitic microstructure. In general, tempered steels exhibit a sorbitic microstructure.

In ferrite/pearlite steels, grain boundaries play a crucial role in influencing the hydrogen diffusion coefficient. These boundaries can enhance hydrogen diffusion by providing preferential diffusion paths and alter the hydrogen uptake in the material. Conversely, they may also inhibit hydrogen mobility by acting as reversible trapping sites, particularly at triple junctions and grain boundary nodes increasing the amount of hydrogen uptake [78–81]. Owing to these opposing effects, the hydrogen diffusion coefficient reaches a maximum at an optimal grain size, reported to be approximately 45 μm [82–84]. Higher values of effective diffusion coefficients have been observed in steels with coarse grains and a high density of manganese sulphide (MnS) inclusions [85–87]. Furthermore, the orientation of MnS inclusions has been shown to significantly affect hydrogen diffusivity.

The microstructural anisotropy of hot-rolled steels also influences hydrogen diffusion. Pearlitic bands in these steels serve as diffusion barriers, resulting in a highly anisotropic diffusion behaviour [88]. In contrast, tempered martensitic microstructures are more homogeneous and do not exhibit such anisotropy. In as-quenched martensite, hydrogen diffusivity reaches a minimum but increases with higher tempering temperatures [89].

Gadgeel and Johnson [90] reported that in normalized carbon steels, both permeability and diffusivity decrease with increasing carbon content. They further noted that

hydrogen permeability is largely independent of heat treatment, whereas diffusivity is maximized in quenched and tempered conditions and minimized in normalized microstructures.

Regarding welded joints in pipes, the density of hydrogen traps is generally higher in both the weld metal and the heat-affected zone (HAZ) than in the base metal. This is attributed to a greater number of precipitates and elevated residual stress levels, which act as effective hydrogen traps increasing the hydrogen uptake [82, 91, 92].

1.5 Hydrogen diffusivity and uptake evaluation methods

Currently, several approaches are employed in extensive experimental research to evaluate hydrogen diffusion into metals for pipeline applications, particularly regarding gaseous hydrogen, both in its pure form and when mixed with other gases [7, 93], as well as to assess the susceptibility of metal alloys to hydrogen embrittlement [25, 26]. The evaluation of diffusible hydrogen is crucial: hydrogen-induced brittle fracture is closely associated with diffusible hydrogen, especially under conditions of slow strain and plastic deformation [94–98].

Various methods have been developed to investigate the hydrogen diffusion coefficient and uptake, including thermal desorption spectroscopy [99–101], melt extraction, vacuum extraction [102], silver micro-printing [103], tritium autoradiography, gas chromatography [104], and electrochemical impedance spectroscopy [105].

A widely adopted strategy to evaluate hydrogen uptake and diffusion coefficients relies on electrochemical methods using a Devanathan–Stachurski permeation cell [106, 107]. These methods employ a double-compartment cell with a thin metallic sample separating the two semi-cells. One side of the sample is cathodically polarised to charge it with hydrogen, while the other side is maintained under anodic polarisation, keeping the surface hydrogen concentration effectively zero. Consequently, diffusible hydrogen fluxes from the cathodic side to the anodic side. The diffusion coefficient can be estimated using different approaches, such as the lag time (t_{lag}), breakthrough time, or the slope method [108].

A more recent, simplified approach for estimating hydrogen uptake and the diffusion coefficient uses a single-compartment cell [109]. This methodology involves a two-step procedure: an initial electrochemical charging phase, in which the metallic sample is saturated via cathodic polarisation at potentials below the equilibrium potential for hydrogen evolution, followed by a discharging phase under anodic polarisation at

potentials above the equilibrium potential. The time evolution of the anodic current during discharging reflects the flux of diffusible hydrogen exiting the sample. This flux depends on the initial concentration of diffusible hydrogen (i.e., the hydrogen uptake), the diffusion coefficient, and the elapsed time between the end of charging and the start of discharging. Analytical solutions can be applied to the current transient measured during anodic/cathodic pulse polarisation to derive both the diffusion coefficient and hydrogen concentration [110, 111]. In most cases, it is necessary to ensure strictly one-dimensional hydrogen flow, since the majority of diffusion models, including those that account for trapping phenomena, rely on the assumption of a well-defined, oriented one-dimensional transport path.

Chapter 2

Mechanical fracture behaviour of pipeline steels in the presence of hydrogen

In this chapter, the parameters described in Chapter 1 are discussed with respect to their effect on the material when mechanical loading acts synergistically with hydrogen ingress, as further elaborated in the literature review.

2.1 The role of mechanical stress on diffusion of hydrogen

Hydrogen can penetrate into the material and diffuse through it; naturally, the ability of a material to permit hydrogen transport depends on its intrinsic properties, as discussed in Section 1.4. However, the diffusion coefficients, and consequently the amount of hydrogen that permeates the material, are significantly affected by the presence of an applied stress field.

In the analysis of hydrogen diffusion in steels under mechanical stress, it is necessary to distinguish between two situations:

- the application of stress followed by hydrogen ingress;
- the simultaneous occurrence of hydrogen diffusion and mechanical loading.

In the first case, the influence of strain hardening on hydrogen diffusion must be considered. It is widely recognised that cold working affects hydrogen permeation: plastic deformation increases the density of dislocations, which act as hydrogen traps, thereby enhancing hydrogen uptake while simultaneously reducing the hydrogen diffusion coefficient in steels [59, 91, 112–119]. These findings were primarily obtained through electrolytic hydrogen charging. The effect of plastic straining on gaseous hydrogen absorption under high-temperature and high-pressure conditions in hot-rolled *S30408* steel was reported by Qu et al. [120], who observed that the hydrogen diffusion coefficient initially decreases with strain up to approximately 20%, before increasing with further plastic deformation. This behaviour is governed by two mechanisms associated with dislocations and strain-induced martensite, which dominate at different stages of deformation.

In the second case, the effect of hydrogen diffusion depends on the nature of the loading cycle: constant load (elastic or plastic), monotonic loading at either constant or variable strain rates, or cyclic loading with various waveforms (sinusoidal, triangular, square, etc.), as commonly encountered in corrosion-fatigue studies. Several authors have investigated the effect of constant load on hydrogen permeation through metal membranes. Beck and Bockris [121] reported different responses under elastic and plastic loading: in the elastic regime, the permeation current increases due to enhanced hydrogen uptake in the distorted lattice, while the diffusion coefficient D remains largely unchanged. Under plastic deformation, new dislocations are generated, which act as traps for hydrogen. This initially reduces the hydrogen flux until the traps become saturated, after which the flux returns to its original steady-state value [114, 122, 123].

Dislocations generated during plastic straining can also serve as preferential pathways for hydrogen diffusion, effectively increasing the apparent diffusivity. The processes of trapping and transport by dislocations are therefore competing mechanisms. A kinetic model proposed by Tien et al. [124] describes hydrogen transport by dislocations surrounded by Cottrell atmospheres, where dislocations drag or sweep clouds of hydrogen atoms and deposit them at microstructural sites critical for fracture, such as grain boundaries, inclusions, and microvoids [125]. Several subsequent theoretical models have further refined this description [126–132], and three-dimensional finite element simulations have been used to study hydrogen distribution as a function of the stress field at the crack tip of SE(B) specimens [133].

The influence of strain rate on hydrogen embrittlement reflects the balance between dislocation generation and hydrogen diffusion. Similar behaviours have been observed in API 5L X52 steel, high-strength X100 steel [122, 123, 134], and nickel [135].

Apparent hydrogen diffusivity decreases with increasing average load under cyclic loading in the plastic regime [136, 137]. Permeation measurements conducted under very slow strain rates ($< 10^{-6}$ s^{-1}) show minimal effect from dislocation trapping, as the traps become fully saturated, leading to similar behaviours across different steels. At higher strain rates (higher than 10^{-5} s^{-1}), dislocation-induced trapping plays a significant role in hydrogen transport, establishing a clear link between hydrogen mobility and susceptibility to embrittlement.

2.2 Mechanical stress in pipelines and its experimental simulation

Hydrogen embrittlement phenomena require the synergistic action of slow plastic deformation in the presence of hydrogen, as discussed in Section 1.3. Such conditions commonly occur in pipelines due to soil movements, as reported by [138]. However, there is no universal mechanism to simultaneously describe and take into account all forms of the HE [20, 32–34, 36]. Most often, a multidisciplinary approach based on the use of different advanced experimental-laboratory methods, theoretical and quantum mechanical models, modern micro-and nano-research, micro-fracture mechanics, atomistic investigations and solidstate physics, provides conditions for a much better understanding of extremely complex, multiple and often simultaneously active mechanisms of the HE [20, 33–35]. In laboratory studies, these conditions are typically reproduced using slow strain rate (SSR) tests or elastic-plastic mechanical fracture (EPMF) tests, which simulate the presence of defects, combined with *in situ* hydrogen charging. During these experiments, hydrogen charged can migrate to the crack tip through two primary mechanisms: either by mobilising hydrogen already present within the material or by external uptake. Both processes lead to the formation of a hydrogen-enriched zone around the crack, thereby increasing the material's susceptibility to embrittlement. The diffusive hydrogen moving through the metal lattice and concentrating in regions of lower hydrogen content. The formation of new surfaces during crack propagation modifies the lattice and generates hydrogen-poor regions that further attract hydrogen from surrounding areas. Under such conditions, atomic hydrogen tends to accumulate preferentially in the most highly stressed regions, i.e., in the close of defects, as reported by [139]. This localised enrichment of hydrogen reduces the material's toughness, diminishes both plasticity and strength, and can ultimately lead to crack initiation or brittle fracture [44–46, 140–142].

2.2.1 Slow strain rate approach

The presence of continuous plastic deformation is essential to trigger HE, as demonstrated by interrupted slow strain rate (ISSR) tests conducted in solution with concurrent cathodic polarisation. No crack formation was observed at potentials down to -1.05 V vs SCE [139]. In these tests, specimens were initially loaded at a strain rate of 10^{-5} s^{-1}. After reaching the maximum load, the applied load was reduced by 5% and the elongation was paused, leaving the specimens under constant deformation in the test solution for one week. The micro-cracks only at -1.5 V vs SCE, particularly in the highest strength steels produced via controlled rolling and accelerated cooling.

HE was mainly observed during dynamic SSR tests and slow bending experiments carried out under continuous plastic deformation at low strain rates. The severity of hydrogen embrittlement increased with cathodic polarisation exceeding a critical threshold, leading to a measurable reduction in ductility compared to reference specimens tested in air. The critical potentials for the initiation of HE were found to depend on both the strain rate and the tensile strength of the material [139], with susceptibility increasing markedly at very negative cathodic potentials and at low strain rates. Similar trends were observed in slow bending tests [85].

2.2.2 Elastoplastic fracture mechanics approach

Slow strain rate tests only simulate uniaxial tensile stresses, which do not fully represent real service conditions. It is therefore necessary to reproduce the presence of defects on the pipe wall, as these may lead to perforation of the pipeline with leakage of the transported fluid. In more severe cases, such defects can trigger rapid propagation along the longitudinal direction (the most critical scenario), as it may result in extensive splitting of the pipe over long distances.

It is therefore essential to evaluate the effects of defect propagation in the longitudinal direction (the most severe case) under realistic conditions. Conducting a critical experiment that accurately replicates the kinetics of hydrogen-induced damage, in line with the actual behaviour of pipeline exposed to hydrogen during service, is extremely challenging [143].

Pipelines are constructed from materials that exhibit high tenacity and resilience, allowing for substantial plastic deformation. Moreover, hydrogen embrittlement effects are observed primarily under slow plastic deformation within the plastic regime. Consequently, it is necessary to perform *elastoplastic fracture mechanics* (EPFM) tests to accurately characterise the material behaviour under these conditions.

Such tests allow for the estimation of the energy required to initiate a defect, using different approaches (e.g., compliance, direct current potential drop, etc.). This methodology enables assessment of the overall defect initiation behaviour, taking into account the plastic response of the material. Moreover, to evaluate the influence of hydrogen-promoting environments on mechanical behaviour, it is essential to perform *in situ* experiments where hydrogen charging and mechanical testing are carried out simultaneously.

Through elastoplastic fracture mechanics, it is possible to study defect initiation and propagation under realistic service conditions, simulating environments such as cathodic protection or internal exposure to transported hydrogen gas. Several mechanisms have been proposed to explain defect propagation under these conditions, including hydrogen-enhanced decohesion (HEDE) and hydrogen-enhanced localized plasticity (HELP) [33, 34, 144, 145]. Dislocation mobility is observed to increase across a wide range of hydrogen concentrations, indicating that the HELP mechanism is active, with its effect depending on the local hydrogen content [146]. In contrast, the HEDE mechanism only occurs when the hydrogen concentration reaches a sufficiently high, or "critical", level, weakening the atomic lattice and producing a sharp ductile-to-brittle transition with significant loss of ductility [146, 147].

2.3 Mechanical behaviour of pipeline materials in hydrogen

Pipeline steels with yield strengths ranging from conventional API 5L X52 (TYS = 360 MPa) to more recent X100 grades (TYS = 700 MPa) generally exhibit substantial resistance to hydrogen embrittlement under constant load conditions and typical cathodic protection levels, even at strongly negative potentials. Nevertheless, it remains necessary to assess the conditions associated with the transported hydrogen gas and to determine the possible critical values linked to its presence. Failures have nonetheless been reported due to localised microstructural heterogeneities, such as hard spots [148, 149], slow plastic deformation [150], mechanical damage, or geotechnical events such as landslides [151].

Laboratory studies have been performed to identify the critical conditions for HE initiation as a function of applied potential and strain rate, particularly for high-strength grades such as X80 and X100 [24, 85, 152]. X100 steel is of particular interest for long-distance, high-pressure gas pipelines. These findings have been further corroborated by full-scale testing [153]. In constant-load experiments conducted at a stress level

equal to the tensile yield strength, no specimen failure was observed, even under overprotection conditions at -1.5 V and -2 V vs SCE at room temperature [24]. The observed resistance to HE was further confirmed by mechanical fracture tests on pre-cracked, modified WOL specimens, which showed no crack propagation from the fatigue pre-cracks under axial constant load.

The mechanical properties of these steels have been optimised through minor adjustments in chemical composition and thermo-mechanical processing parameters. The lower critical potential observed for steels with relatively low ultimate tensile strength (UTS) is associated with the finer pearlite–ferrite microstructures typical of rolled and controlled-rolled products. In contrast, the behaviour of higher-strength steels, such as X80 and X100 grades, is closely linked to their acicular microstructures. The presence of hard phases, including untempered martensite, significantly diminishes the material's resistance to hydrogen embrittlement [81].

Chapter 3

Materials and environments investigated

This chapter introduces the experimental work, beginning with a description of the materials used in this study, followed by an overview of the environments employed to charge the samples, either through cathodic polarization or hydrogen gas exposure.

3.1 Materials

In this thesis, two steels from gas and oil transmission pipelines are analysed: a more recently manufactured, non-operated material referred to as *steel A*, and an older, in-service material referred to as *steel B*.

Steel A is a high-strength low-alloy (HSLA) steel, API 5L X60 grade, obtained from a 14.3 mm thick hot-rolled, longitudinally welded pipe with a nominal diameter of 24”, intended for gas and oil transport. The pipe had never been in service and was produced relatively recently, around the early 2000s.

Steel B consists of a section of API 5L X60 pipe manufactured in 1970 and later removed from service. This pipe had a nominal diameter of 26” and a wall thickness of 11.3 mm. A comparison of the chemical compositions of the two materials is reported in Table 3.1. No substantial differences were detected, except for slightly higher manganese and sulphur contents in steel B.

Table 3.1: Chemical composition of steels A and B.

Steel	Element	C	Mn	Si	P	S	Nb	Mo	V	Cu	Ni	Cr	Ceq
A	[%wt]	0.09	1.64	0.24	0.003	0.002	0.049	0.002	<0.0001	0.011	0.017	0.031	0.366
B	[%wt]	0.19	1.24	0.23	0.0075	0.014	0.0475	0.0035	<0.0001	0.0155	0.01275	<0.0001	0.395

The microstructure of steel A (Figure 3.1) is typical of hot-rolled plate, characterised by ferrite–pearlite banding aligned along the rolling direction, as shown in the detailed view in Figure 3.1-c. The grain size falls within the ASTM 10.5–11 range (Figure 3.2).

The microstructure of steel B is consistent with the manufacturing practices of the time, displaying a ferrite–pearlite structure with banding along the rolling direction (Figure 3.3). The grain size corresponds to ASTM 10–10.5.

In steel B, the grains are slightly smaller. Inclusion-rich regions are also present, locally interrupting the pearlite–ferrite banding, as shown in Figure 3.4.

These areas correspond to manganese sulphide (MnS) inclusions, enriched in manganese and sulphur and depleted in iron, as confirmed by the EDS analysis in Figure 3.5.

Such features are likely associated with the production technologies available at the time, which did not provide the same degree of process control as modern manufacturing routes.

The tensile properties of steel A, determined from specimens extracted parallel to the pipe axis and tested in accordance with UNI EN ISO 6892-1:2020, exhibit a yield strength in the range 400–440 MPa and an ultimate tensile strength of 533–565 MPa, as shown in Figure 3.6. In contrast, steel B exhibits a yield strength of 423–461 MPa and an ultimate tensile strength of 561–596 MPa; all reported mechanical properties, including a reduction of area of 26–31 %, are derived from the material documentation.

3.2 Environments investigated

3.2.1 Solution for electrochemical charging

Two alkaline test solutions were considered for electrochemical charging under applied cathodic polarisation:

- 0.1 M sodium hydroxide solution
- Carbonate–bicarbonate solution

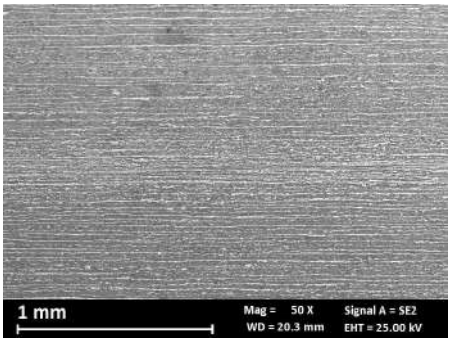

(a) Surface macrograph after etching.

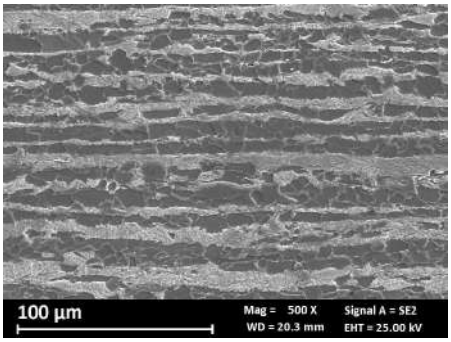

(b) Detail of ferrite–pearlite banding.

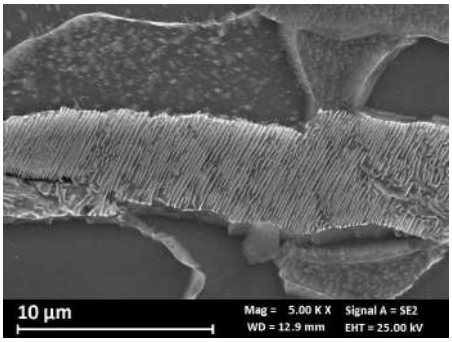

(c) Pearlite region showing characteristic lamellae.

Figure 3.1: Metallographic details of steel A after etching.

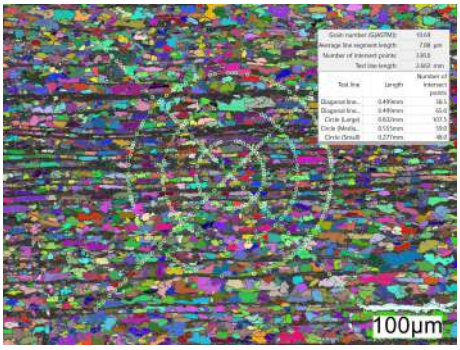

Figure 3.2: Average grain size analysis according to ASTM standards for steel A.

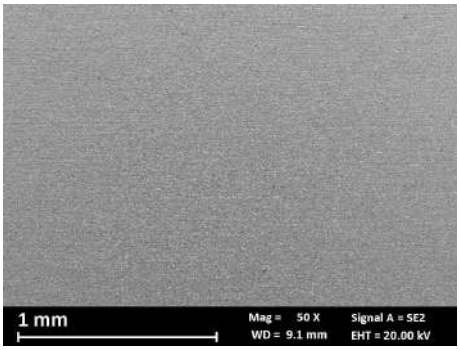

Figure 3.3: Surface after acid etching of steel B.

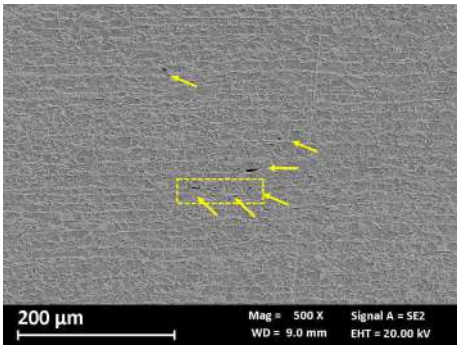

Figure 3.4: Etched surface showing banding and inclusion-rich areas in steel B.

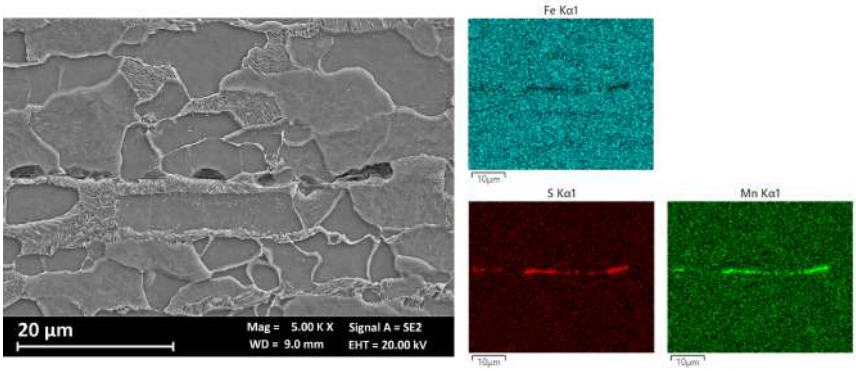

Figure 3.5: EDS analysis of inclusion-rich regions in steel B.

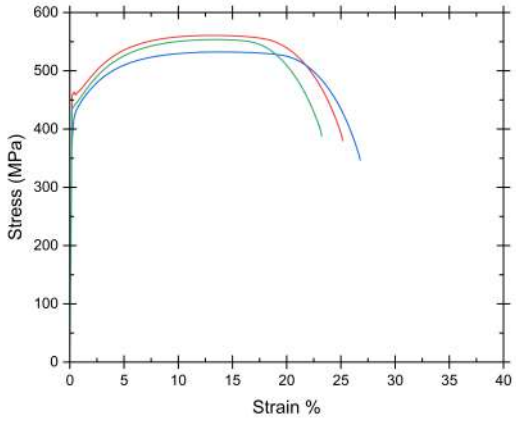

Figure 3.6: Tensile curves of steel A.

The first was a 0.1 M sodium hydroxide solution, used as a reference environment, while the second was a carbonate–bicarbonate solution consisting of 26.5 g/L Na_2CO_3 and 42 g/L $NaHCO_3$, with a pH of 10. This latter solution was selected to simulate conditions representative of real pipeline environments where cathodic protection is employed to prevent general corrosion. Cathodic protection applies a cathodic potential using naturally occurring soil moisture as the electrolyte. Although such environments are typically near-neutral, they may become alkaline under overprotection conditions, particularly when coating defects allow stagnant water to accumulate. Under these circumstances, water reduction occurs on the steel surface, generating atomic hydrogen that can diffuse into the pipe wall. This solution was previously used by [154] to simulate soil moisture in studies concerning stress corrosion cracking.

3.2.2 Gaseous charging

Gaseous hydrogen charging was performed at the laboratories of the University of Manchester. The specimens were charged in an autoclave supplied with high-purity hydrogen gas (99.9999%), delivered from a 50 L cylinder. The charging procedure employed is detailed in Sections 5.6 and 6.5.

Chapter 4

Hydrogen uptake and diffusion: an electrochemical data-based model

Chapter 4 focuses on the analysis of the apparent hydrogen diffusion coefficient and hydrogen uptake, describing both the experimental setup and the data-driven model developed to estimate these parameters under three-dimensional flux conditions for the pipeline steels discussed in Chapter 3. The procedural details are explained in Appendix A.

4.1 Experimental

4.1.1 Sample geometry used

The test was performed using the same geometry for both materials investigated (steels A and B, as described in Chapter 3). Cylindrical specimens were used, with a diameter of 13 mm and a height of 45 mm. An M3 thread was machined on the top surface of each cylinder to allow attachment to the sample holder, which consisted of a threaded rod. Only a few threads were engaged in order to minimise any alteration of the initial geometry. For all analyses, the specimens were ground with abrasive papers up to 1200 grit and subsequently degreased with acetone.

4.1.2 Experimental lay-out

The electrochemical single-compartment cell is shown in Figure 4.1.

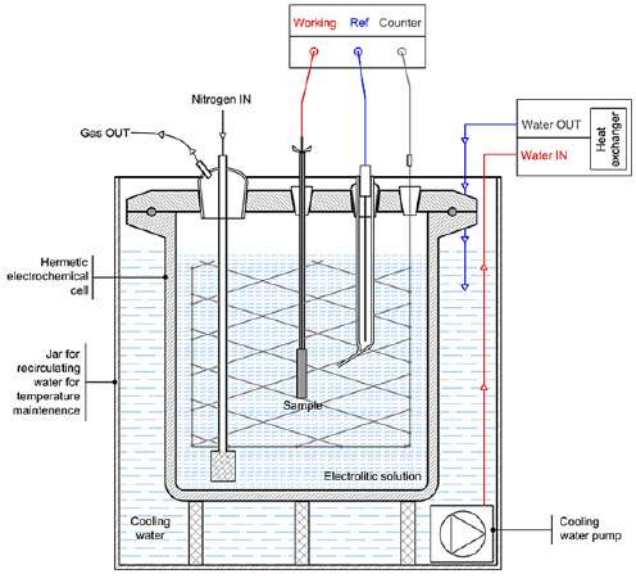

Figure 4.1: Scheme of the electrochemical charging/discharging cell with a single compartment.

The sample was positioned at the centre of the cell to ensure uniform current distribution from the counter-electrode. It was connected to the working electrode via a threaded rod, which was insulated by a glass tube. An activated titanium mesh basket was used as the counter-electrode. The potential was measured using a saturated calomel electrode (SCE) reference electrode with a lugging probe. The cell was filled with the test solution, which was maintained at a constant room temperature of approximately 23 ± 0.1°C using a thermostatic bath. Prior to the experiment, the solutions were deaerated for 12 h through nitrogen bubbling and maintained during the entire testing time.

4.1.3 Experimental procedure

The experimental procedure was conducted in different phases. Initially, after sample assembly and nitrogen flushing, the test cell was filled with the deaerated solution. The specimens were then polarised at +0.306 V versus SCE to obtain the passivation curve. The passivation potential was assumed to be equal to that recommended by the

ISO17081 standard for the detection side of the Devanathan–Stachurski cell operating in the 0.1 M sodium hydroxide solution expressed versus SCE. This potential was also applied to the tests conducted in the carbonate–bicarbonate solution at pH 10. As confirmed by the potentiodynamic test in Figure 4.2, this value was within the passivity range of steel for this environment.

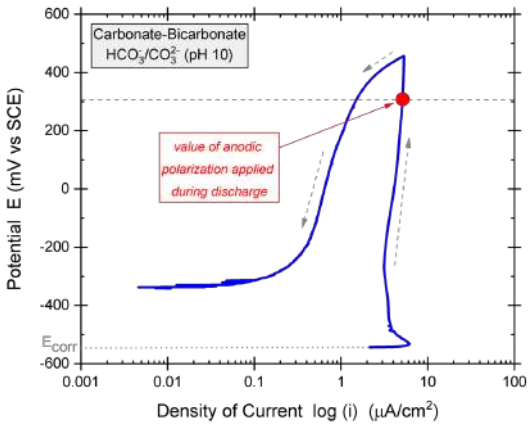

Figure 4.2: Forward and reverse potentiodynamic polarisation curve in a deaerated solution of carbonate–bicarbonates (pH 10). This test was executed at room temperature with a scan rate of 10 mV/min from -0.2 mV to + 500 mV vs. OCP.

Hydrogen charging was conducted through potentiostatic cathodic polarisation in the range of -1 to -1.8 V versus SCE for 15 h, which was sufficient time for the specimens to achieve a homogeneous hydrogen concentration at a typical value of diffusivity reported for low-carbon steel [21, 155]. During this step, part of the hydrogen produced on the surface was absorbed into the steel. At the end of the charging phase, polarisation was immediately inverted to apply the anodic polarisation again at +0.306 V versus SCE for 15 h to measure the discharging current curve. The discharging anodic current represents the passivity current enhanced by the current due to the oxidation of hydrogen egressing from the metal. To estimate the net current due to hydrogen oxidation, the experimental value of the discharging current was depurated by subtracting the passivation current curve measured during the early phase. The integration of the net hydrogen current over the testing time allows for the estimation of the charge $Q_{Hadj}(t)$ due to the oxidation of diffusible hydrogen mass egress from the sample. Finally, the mass of hydrogen outgoing ($M_{Hadj}(t)$) from the sample can be derived using Faraday's law.

The residual mass of hydrogen that remains in the sample $M_{res}(t)$ is given by the following relation:

$$M_{res}(t) = M_{\infty} - M_{Hadj}(t) \tag{4.1}$$

where M_{∞} is the steady-state value of the outgoing mass discharge of hydrogen. The average concentration of residual diffusible hydrogen that remains in the sample $C_{res}(t)$ at time t can then be evaluated by dividing the residual mass of hydrogen by the sample mass (M_{sample}), as shown in (4.2)

$$C_{res}(t) = \frac{M_{res}(t)}{M_{sample}} \cdot 10^6 [ppm] \tag{4.2}$$

4.2 Theory and Calculation: FEM simulation

To simulate electrochemical discharge correctly, it was necessary to model the actual geometry of the specimen used during experimental tests in similar discharging conditions. Thus, tri-dimensional diffusion of hydrogen from the sample during electrochemical discharge was simulated through the FEM model using *COMSOL Multiphysics* in cylindrical coordinates. The specific cylinder geometry of the sample adopted in this work was considered. The diffusion process in the metal is described by Fick's second law (4.3), where C and t are the hydrogen concentration and time, respectively.

$$\begin{cases} \dfrac{\partial C}{\partial t} - D\nabla^2 C = 0 \\ C_0^* = \text{constant}, \quad D = \text{constant} \quad \text{(I.C.)} \\ C_s = 0 \quad \text{on surfaces} \quad \text{(B.C.)} \end{cases} \tag{4.3}$$

The model includes the initial conditions (*I.C.*) of homogeneous hydrogen concentration C_0^* and constant diffusion coefficient D. During discharging, the boundary condition (*B.C.*) on the metal–solution surface imposes the concentration C_s to be equal to zero. This condition describes the behaviour of anodic polarisation imposed during electrochemical discharging on the specimen. In fact, during discharge the atomic hydrogen in the lattice that spread up to the surface it is immediately sequestered on the surface. This due to the hydrogen atoms can react with further discharging H^+ ions producing hydrogen molecules and leave the surface for alkaline environment [156]; therefore it is possible to consider the superficial hydrogen concentration equal to zero. The simulations conducted varying diffusion coefficients D between $1 \cdot 10^{-12}$ and

$1 \cdot 10^{-9} \frac{m^2}{s}$ and initial concentrations C_0^* between 0.3 and 10 ppm. The flux of hydrogen leaving all sample surfaces is then obtained using Fick's first law (4.4), given the concentration gradient normal to the external sample surface.

$$\phi^*_{egress} = -D \cdot \nabla C \tag{4.4}$$

The mole of egress hydrogen ($n^*_{egress}(t)$) was obtained through the integration of the flux over time. Thus, to obtain the average residual concentration (C^*_{res}) that remains in the sample at a certain time, considering an initial concentration C_0^* at the end of charging, the following evaluation is necessary:

$$C^*_{res}(t) = \sum_{t=0}^{\infty} \frac{n^*_{egress}(t=\infty) - n^*_{egress}(t)}{Volume} \qquad \left[\frac{mol}{m^3}\right] \tag{4.5}$$

4.3 Results and discussion

4.3.1 Elaboration of FEM simulations

Figure 4.3 shows the distribution of the hydrogen concentration inside the cylinder sample, modelled at $1 \cdot 10^{-12} \frac{m^2}{s}$ diffusivity, 2 $\frac{mol}{m^3}$ initial homogenous concentration with superficial concentration equal to 0 ppm as B.C, after $3 \cdot 10^6$ s.

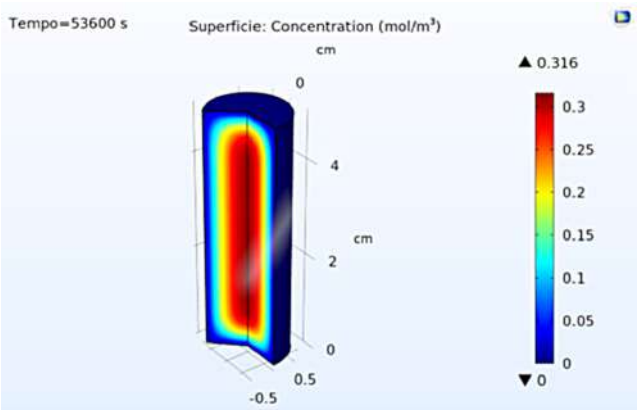

Figure 4.3: Simulation result of a cylinder with diameter of 13 mm and a height of 45 mm (the geometry is exactly the experimental ones) of the hydrogen egress to $D = 1 \cdot 10^{-}12 \frac{m^2}{s}$ and $C_0^* = 0.347 \frac{mol}{m^3}$. The colour map represents the distribution of the hydrogen concentration in mol/m^3 after 12440 s. It was used 1647 quadrilateral elements. The grade of freedom is 2009, which is used as an integration step equal to 60000 s.

To discretise the geometry, it was used the axial symmetric property of the problem thus it was built a grid mesh only on a single rectangular section with side coinciding with the axis of the cylinder. The mesh is automatically built via the "quadrilateral mesh generator" that create not strictly only quadratic elements, but in places of the geometry where it judges it as necessary, it could be also create triangular elements. In this case, the plane of studied was composed by 1647 quads. The simulation solves the 2009 grades of freedom, with an integration step equal to 60000 s. It should be noted that the flux comes from all surfaces.

Figure 4.4 shows the average concentration of residual hydrogen that remains in the sample (C^*_{res}) that can diffuse during the discharging period estimated via simulations.

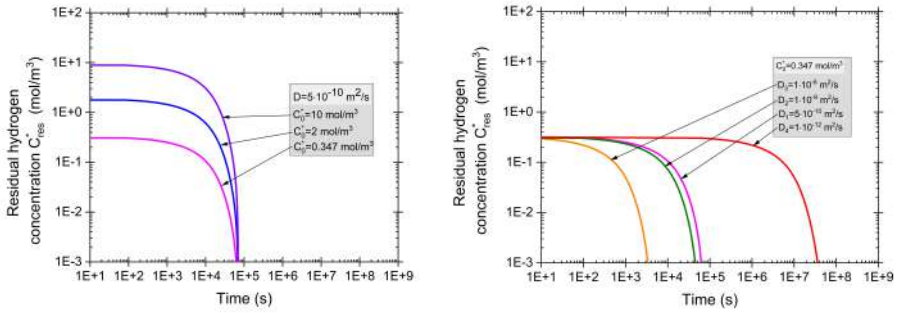

(a) Curves obtained by different initial concentrations.

(b) Curves obtained by different diffusion coefficients.

Figure 4.4: Simulation curves of the residual average concentration C^*_{res} vs. discharging time.

At the end of all simulations, the flux tended close to zero. Thus, it can be assumed that there is no residual diffusible hydrogen in the metal. Nevertheless, changing the initial concentration of the simulations implies the modification of the initial point of the residual concentration curve, but constant diffusivity guarantees that all branches begin to come closer to zero at the same time. Varying the diffusion coefficient at a constant initial concentration involves large variations of egressing time to achieve a low residual concentration at the end of the simulation. Increasing the diffusion coefficient means having a faster hydrogen outflow and vice versa.

All the simulated curves can be described according to a unique curve (dashed line in Figure 4.5)

by introducing the dimensionless time $\widehat{T}$ and the dimensionless concentration $\widehat{C}^*(t)$ defined as follows:

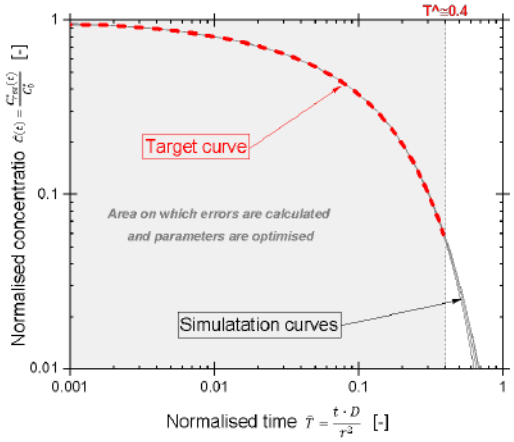

Figure 4.5: Target curve obtained from the overlapping of the different normalised simulation curves.

$$\widehat{T} = \frac{t \cdot D}{r^2} \tag{4.6}$$

$$\widehat{C*}(t) = \frac{C^*_{res}(t)}{C^*_{res}(t=0)} \equiv \frac{C^*_{res}(t)}{C^*_0} \tag{4.7}$$

where r is the radius of the cylinder. The unique target curve is the result of the overlapping of the first branch of all simulated curves truncated at $\widehat{T} = 0.4$. Investigating the values of the average residual concentration under 1/100 of the initial concentration is not significant because the values are extremely low. Moreover, the first branch of the target curve has the largest amount of hydrogen flux, accounting for the most significant part of interpolating the experimental discharging curves. This curve is independent of the diffusion coefficient and the initial concentration.

4.3.2 Experimental curves and physically driven optimisation steel A

Figure 4.6 shows an example of the experimental curves related to the carbonate–bicarbonate solution.

It compares the passivation curve obtained in the early phase with the potentiostatic polarisation discharging at +0.306 V versus SCE after cathodic charging at different potentials. It can be noted that the passivation current is low but not negligible, with

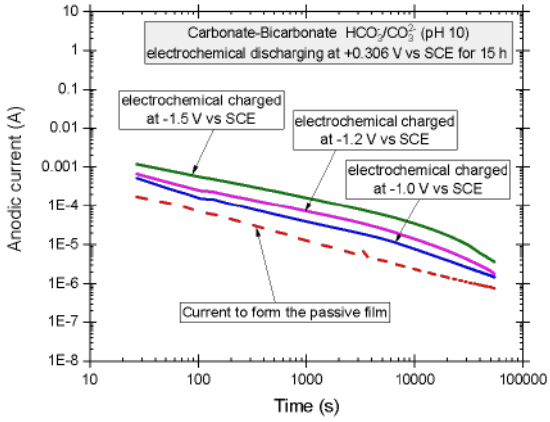

Figure 4.6: Comparison between the passivation and discharging curves at +0.306 V vs. SCE of the test in carbonate–bicarbonate solution.

respect to the discharge current, even at a high level of hydrogen charging. Thus, it is necessary to depurge the discharging current measured by the passivation contribute, subtracting from discharging curves the passivation curve.

Integrating the net discharging current over time obtains the charge evolution $Q_{Had\,j}$ in time. The net charge increases over time due to the egress of hydrogen, and after 15 h of discharge, it achieves a stationarity behaviour (Figure 4.7).

In fact, 90% of the total charge pass in 8 h. Thus, in the remaining time, the value of the charge pass is very low, and the variation can be assumed to be stationary. Therefore, after 15 h, it is possible to consider that the egress of diffusible hydrogen is complete. The last part of the branch can be assumed to define the stationarity conditions at an infinite time.

The charge trend calculates the mass of the diffusible hydrogen flow through the surface using Equation (4.1), assuming that the last point is stationary. Thus, the curves of the average residual hydrogen concentration $C_{res,\ \ ad\,j}(t)$ can be estimated over time using Equation (4.2).

The normalisation approach can be used to estimate the initial hydrogen content C_0 charged, the diffusion coefficient D and the elapsed time t between the end of charging and the initial discharging step through the experimental curves. The experimental data can be normalised in time and concentration using Equations (4.6) and (4.7) by imposing the adequate C_0, D and t_0. In the first attempt, the parameters should be evaluated using empirical rules. Thus, it is possible to adapt the normalised experi-

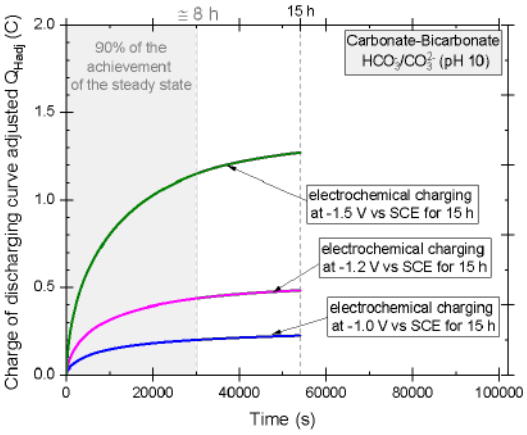

Figure 4.7: Charge of the discharging curve at +0.306 V vs. SCE after charging at different cathodic polarisations in carbonate–bicarbonate.

mental data overlapping the unique target curve by changing the parameters C_0, D and t_0 of normalisation. Optimisation minimises the relative error function estimated as the difference between the two above curves. As previously noted, the calculation of the error to optimisation is estimated along the target curve up to the normalised time under 0.4.

This procedure was implemented using a *Matlab Code* and is available on the data in brief [157] and can be downloaded via Mendelay data. This iteration procedure exploits the *fminsearch* function, a nonlinear programming solver that uses the Nelder–Mead simplex. It is a simplex of n+1 points, which are sorted according to the descending value of the function. It discards the worst value and replaces it with a new point according to some criteria.

Figure 4.8 illustrates an example of the iteration results for the test in the carbonate–bicarbonate solution with a charging polarisation of -1.5 V versus SCE.

The results obtained by interpolation represent the best values of the parameter search D_{opt}, $C_{0,opt}$ and t_0, which allows the matching of the experimental curve with the target curve.

4.3.3 Hydrogen residual concentration and apparent diffusion coefficient in the steel A

Different cathodic polarisations have been studied, as shown in Figure 4.9, for the carbonate–bicarbonate solution.

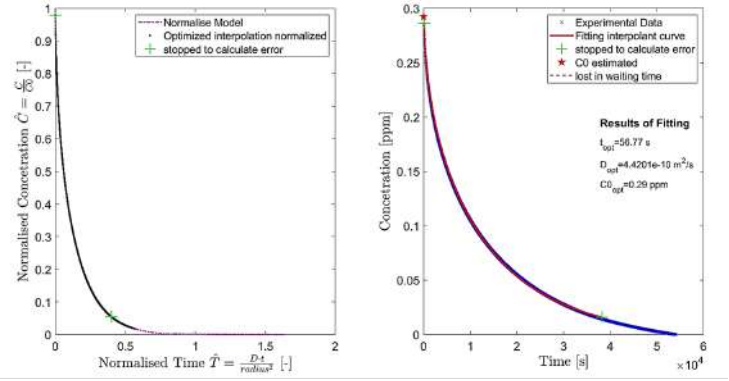

Figure 4.8: Estimation of the diffusion coefficient and hydrogen uptake due to the interpolation of the experimental results with the target curve. This test was conducted in the carbonate-bicarbonate solution, with a charging cathodic polarisation of -1.5 V vs. SCE.

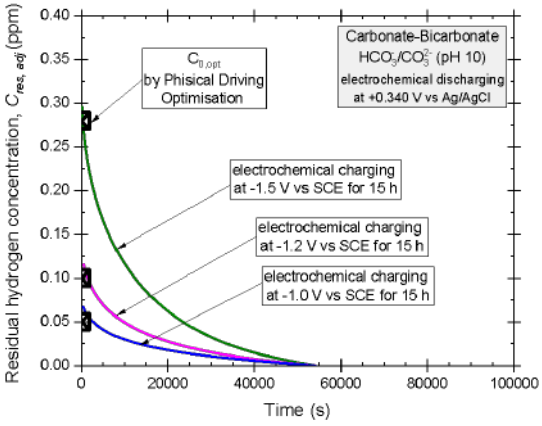

Figure 4.9: Residual hydrogen concentration during the discharging step after cathodic charging and hydrogen uptake through physically driven optimisation.

The average residual hydrogen content decreases over time due to sample emptying, and the curves start from an increasingly high concentration with increase the cathodic potential applied. The first experimental value of concentration does not correspond with the true total initial concentration C_0 charged. Part of the hydrogen is lost during polarisation reversal due to the inertia of the electrochemical system and the changing of the pH diffusion layer surrounding the sample. Thus, it is not known when the first atom of hydrogen egresses from the sample, and there is an uncertainty in the initial values of the current (elapsed time t_0). Moreover, it is impossible to estimate the concentration of hydrogen spread into the sample C_0 through the charging curve. This represents the total circulating current during cathodic charge, but it is impossible to quantify the share of the current responsible for the hydrogen chemisorption process. Thus, even if the elapsed time between the end of charging and the start to discharge is close to zero, consistent with the experimental execution, the initial concentration through the physically driven optimisation and the first value of the experimental curve do not coincide perfectly. Nevertheless, if the elapsed time between charge and discharge is negligible, the initial diffusible concentration corresponds approximately to the area under the discharging curve. Thus, it is possible to compare the results obtained through physically driven optimisation ($C_{0,\,opt}$) by integrating the residual hydrogen concentration curves ($C_{integral}$), as shown in Table 4.1. The differences are extremely small, on the order of hundredths of ppm.

Table 4.1: Comparison of hydrogen uptake obtained using different methods.

Test Solution	**Charging Polarisation**	$C_{integral}$	$C_{0,opt}$
	[V vs SCE]	[ppm]	[ppm]
Sodium hydroxide $0.1M$	-1.2	0.11	0.08
	-1.5	0.26	0.24
	-1.8	0.25	0.22
Carbonate–bicarbonates 26.5 g/l of $Na_2CO_3 + 42g/l of NaHCO_3$	-1	0.08	0.05
	-1.2	0.14	0.10
	-1.5	0.31	0.28
	-1.3	0.11	0.09
	-1.5	0.19	0.14
	-2	0.30	0.21
	-1.2	0.06	0.05
	-1.5	0.14	0.11
	-1.8	0.22	0.18

The reproducibility of the estimated initial hydrogen concentration across multiple tests and methods was good; however, the minor variations observed may be attributed to the microstructure of the steel, which can influence the measurement of such small quantities of hydrogen.

Figures 4.10 and 4.11 show the diffusion coefficients and concentrations estimated by optimisation versus overpotential.

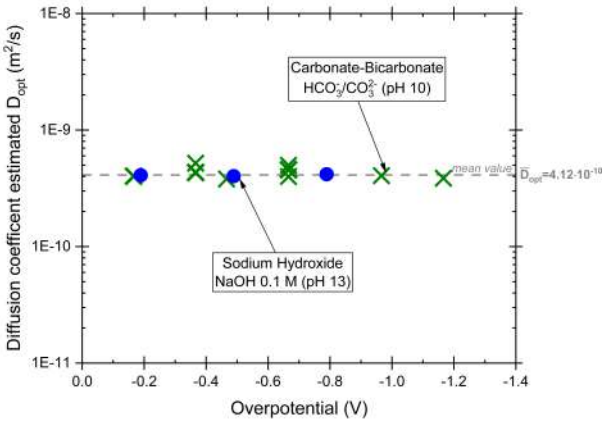

Figure 4.10: Optimised diffusion coefficient estimated using the interpolant method for different cathodic overpotentials and several pH values.

Overpotential represents the available energy for hydrogen evolution reactions [158] and it is estimated according to the definition of Equation (4.8).

$$\eta = \left|E_{appl} - E_{eq}\right| = \left|E_{appl} - (E_0 - 0.059 \cdot pH)\right| \tag{4.8}$$

E_{appl} is the potential applied during charging polarisation, and E_{eq} is the equilibrium potential defined by the Nernst equation and is the function of E_0 (standard electrode potential of hydrogen) and pH value of the solution.

As shown the Figure 4.10, the diffusion coefficient estimated is completely independent of the overpotential (thus polarisation is applied) and environments investigated. The mean value of this material is close to $4.12 \cdot 10^{-10} \frac{m^2}{s}$, consistent with literature on similar steels [158] and similar environmental conditions [119].

The estimate of diffusion coefficient reflects only the contribution of diffusible hydrogen at room temperature in these experimental conditions (apparent diffusion coefficient). During the discharging step, only diffusible hydrogen can diffuse from the

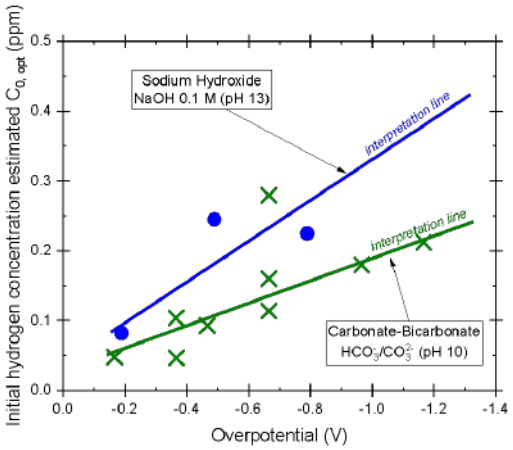

Figure 4.11: Initial hydrogen concentration estimated using the interpolant method for different cathodic charging polarisation and several pH values.

sample due to the experimental conditions used in this study. Anodic polarization ensures that the surface hydrogen concentration remains zero throughout the discharging process. Maintaining room temperature during testing allows the interaction between diffusion and trapping phenomena to be minimised. The hydrogen that is trapped inside the irreversible traps during the charging phase is not released during discharge, and therefore does not participate in the diffusion process. In general, the trapping and detrapping activation energies that alter the flow of hydrogen depend in the first instance on temperature. The energy peaks required to activate these phenomena and induce observable changes in the flow mechanisms are located at temperatures above room temperature [159, 160]. This considering the same material thus with comparable microstructural conditions of vacancies, inclusions and interstitial elements that can altered the trapping phenomena [81, 161, 162]. In this way, it is possible to control diffusion conditions in three-dimensional flux under Fick's second law and to investigate the apparent diffusion coefficients. The latter must be dependent only on the material and independent of the applied polarisation and testing environment. Therefore, the initial hydrogen concentration estimated using this method indicates the diffusible hydrogen (hydrogen uptake) in this specific material and in certain experimental conditions. Specifically, the initial hydrogen concentration is strongly dependent on overpotential, and increased polarisation increases the initial hydrogen concentration in all environments tested, as shown in Figure 4.11. Changing the pH value changes the equilibrium potential during charging polarisation, as indicated in Equation (4.8),

even if the actual applied overpotential is altered by the formation of a local alkalinisation layer at the cathode. This effect is contrasted with the buffering property of carbonate-bicarbonate solution. About the sodium hydroxide solution, the high pH value presents an elevated quantity of OH^- ions that contrasts the H^+ formation, while for the carbonate-bicarbonate solution at pH 10, the buffering capacity that counteracts the cathode alkalinisation must be considered. In all cases, the interpretation lines do not pass through zero because of the persistent mass diffusion layer on the sample surface caused by the alkalinisation reaction.

Through the optimisation presented, it is possible to estimate the apparent diffusion and hydrogen uptake, even in complex geometries or situations in which it is not feasible to extract a tiny plate for a traditional permeation test system. There are no constraints regarding thickness or shape; the only experimental requirement is to guarantee the homogeneous electric field distribution surrounding the sample. It is sufficient to simulate the studied geometry using software (current software capabilities can handle this well), build a characteristic model curve, and use the proposed interpolation method. Moreover, this approach provides possibilities to estimate the diffusion coefficient and hydrogen uptake, and the elapsed time between the end of charging and the initial discharging step is not negligible. Thus, in each case, when it is impossible to make a discharging step immediately (e.g. after gaseous charging in autoclave or in post-charging tensile tests), this approach can be used to correctly evaluate the diffusion coefficient and hydrogen uptake.

4.3.4 Hydrogen residual concentration and apparent diffusion coefficient in the steel B

To validate the data-driven methodology developed, the same experimental procedure and analysis were carried out on the other material investigated. In this case, the analysis was conducted only in the carbonate–bicarbonate solution because, as previously discussed, it is representative of a critical real-world condition.

Figure 4.12 shows the residual hydrogen concentration as a function of time. The values of $C_{0,\mathrm{opt}}$, evaluated through the physically based data-driven optimisation, are in good agreement with the experimental curves.

However, for all polarisation conditions, the values are generally lower than those of the steel A, and the curves appear more flattened. This behaviour is consistent with the apparent diffusion coefficient estimated using this approach, shown in Figure 4.13 as a function of the overpotential (evaluated according to Equation (1.7)).

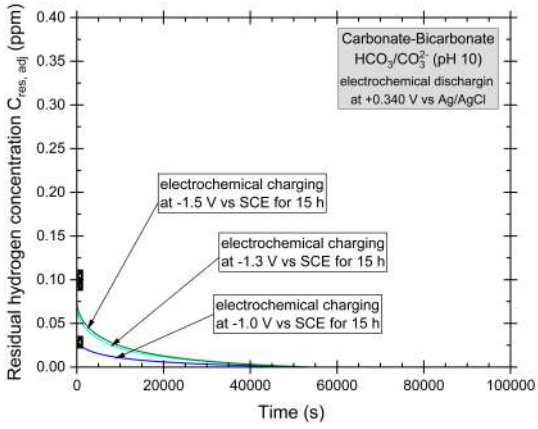

Figure 4.12: Residual hydrogen concentration during the discharging step after cathodic charging and hydrogen uptake obtained through the physically based optimisation applied to the steel B.

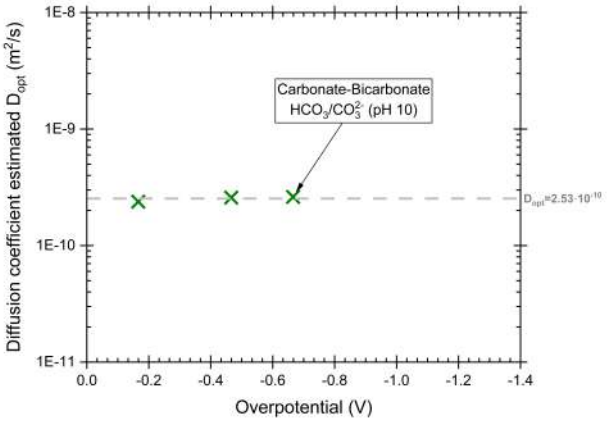

Figure 4.13: Optimised diffusion coefficient estimated using the interpolant method for different cathodic overpotentials.

The diffusion coefficients are approximately half of those obtained for the steel A, indicating a significantly slower diffusion process. Diffusion is therefore more limited in this material. This observation is further confirmed by the variation in the initial hydrogen concentration in the material (Figure 4.14).

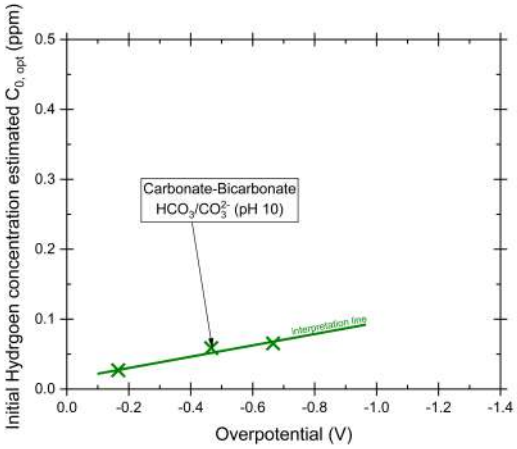

Figure 4.14: Initial hydrogen concentration estimated using the interpolant method for different cathodic charging potentials.

In this case, the variation with overpotential is slightly smaller than that observed for the steel A. The behaviour of both the apparent diffusion coefficient and the hydrogen concentration would thus be consistent with the microstructural analysis. It is well established that grain size and the presence of inclusions can create local zones of hydrogen accumulation around inclusions and alter the apparent diffusion coefficient, thereby affecting the hydrogen concentration [158]. In the measurements performed, the parameters estimated are representative of the overall, macroscopic behaviour of the specimen and do not capture local mechanisms. Additionally, the variation in the initial concentration due to cathodic charging would be limited, as the presence of defects and inclusions would restrict the amount of hydrogen that could be electrochemically introduced into the lattice. This is because the increased number of interfaces between grains can hinder hydrogen diffusion and promote local hydrogen accumulation [84].

Chapter 5

Model application, permeation tests and fugacity

In this chapter, the spontaneous desorption behaviour of both types of pipeline materials following electrochemical charging, is examined through hydrogen uptake tests. A data-driven optimisation models, introduced in Chapter 4, is employed to determine the hydrogen diffusion coefficient, hydrogen uptake, and effective waiting time. These parameters are then compared with results obtained from permeation experiments conducted in the same solutions. The influence of the oxide layer on the permeation flux is also investigated. An equivalent hydrogen pressure corresponding to the applied overpotential is estimated, and the results are confirmed through the evaluation of the data-driven model for gas-charging hydrogen uptake tests.

5.1 Materials and solutions used

Hydrogen uptake samples

The hydrogen uptake tests were conducted using the same cylindrical specimens described in Chapter 4, with a diameter of 13 mm and a height of 45 mm, extracted from the pipe wall thickness. Both materials introduced in Chapter 3 were employed for these measurements.

Permeation samples

For the permeation tests, thin sheet specimens of the steel A (Section 3.1) with a thickness of 1 mm were used in the electrochemical permeation experiments. The specimens were extracted normal to the radial direction to reproduce hydrogen transport through the pipe wall (Figure 5.1). Prior to testing, the surfaces were polished using emery papers up to 1200 grit and subsequently degreased in acetone.

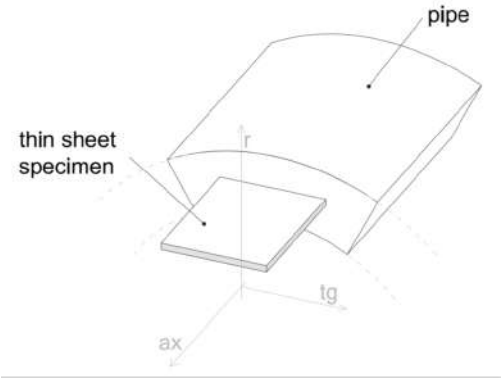

Figure 5.1: Direction of samples extraction to permeation tests.

The permeation tests were performed on uncoated specimens and on specimens with palladium coating on single side or both sides. The coating procedure involved pickling in an acid bath of 37% hydrochloric acid for 3–5 seconds to activate the surface and promote the adhesion of the Pd coating. Afterward, the specimens were rinsed with distilled water, dried, and immediately placed in the palladium electrodeposition cell. The cell was filled with 5 g/L of palladium chloride solution in 30% ammonia by volume (pH 13.5), as described by Vucko [163]. A cathodic current density of $-3\,\mathrm{mA/cm^2}$ was applied for 210 seconds by an activated titanium mesh counter electrode. The sample was washed with distilled water and the unplated side must be treated with abrasive paper up to 1200 grit to remove the pickling effect.

The electrochemical charging was consistently carried out in a pH 10 carbonate–bicarbonate solution (Chapter 3) for both the permeation and hydrogen uptake tests. The electrochemical discharging was performed in a 0.1 M sodium hydroxide solution, as recommended by International Standard ISO 17081 and ASTM G148.

5.2 Experimental methods

5.2.1 Experimental lay out and procedure of hydrogen uptake tests

The experimental layout for the hydrogen uptake tests is described in previous Section 4.1.2. The temperature-controlled cell, containing 5 litres of solution, was deaerated, exclusively during the charging step. The sample was positioned at the centre, threaded onto the sample holder. A basket of activated titanium served as the counter electrode, and a reference electrode, placed in a Lugging probe, was positioned close to the sample surface.

To compare this approach with the permeation tests, the following procedure was proposed. The specimen was electrochemically charged for 15 hours under constant potential conditions of -1.5 V vs SCE in a carbonate–bicarbonate deaerated solution. Afterward, the specimen was dried using compressed air and left in dry air for different waiting times. To analyse the hydrogen discharge, two approaches were used: electrochemical and thermal. The first approach involved reintroducing the sample into the hydrogen uptake cell but replacing the previously solution with a 0.1 M NaOH aerated. The polarisation was then reversed by imposing +0.340 V vs Ag/AgCl for 15 hours (discharge value according to International Standard ISO 17081 and ASTM G-148), simulating the Devanathan–Stachurski procedure.

For the thermal investigation, the charged sample was studied via thermal desorption using a commercial LECO apparatus. In this case, the sample used during electrochemical charging was reduced in size due to the limited dimensions of the LECO crucible (20 mm in height and 8 mm in diameter). Nevertheless, under the same cathodic charging conditions and duration, the smaller sample reached a steady–state current corresponding to saturation, consistent with that observed for the larger geometry. For analysis, the pre-weighed charged sample was placed in a graphite crucible and rapidly fused in an impulse furnace under an argon carrier gas. During fusion, oxygen present in the sample reacts with the graphite to form CO and CO_2, while hydrogen and nitrogen are released as gases. The carrier gas transports the liberated analytes through a series of detectors. CO and CO_2 are first quantified using non-dispersive infrared (NDIR) cells, then CO is oxidised to CO_2 and hydrogen to H_2O in a heated reagent, with the resulting H_2O and CO_2 detected by additional NDIR cells. CO_2 and H_2O are subsequently removed by scrubbing, leaving nitrogen, which is measured using a thermal conductivity detector (TCD). A Dynamic Flow Compensation (DFC) system maintains a constant carrier gas flow during the scrubbing process. Although the instrument is capable of measuring oxygen, nitrogen and hydrogen, in this work

only hydrogen is reported. Quantification is achieved by comparison with calibration standards, and reference measurements of pure carrier gas are performed prior to each analysis to minimise instrumental drift. The thermal desorption was carried out at a constant temperature of 1250°C for 3 minutes, a duration determined through calibration tests to ensure that, by the end of the analysis, the hydrogen signal had decreased to a value close to zero.

5.2.2 Experimental lay out and procedure of permeation tests

Experimental lay out of permeation tests

The permeation tests were conducted using an electrochemical cell based on the configuration adopted by Devanathan and Stachurski [164] showed in Figure 5.2.

The components were made of polymethyl methacrylate. The temperature kept constant to 23 ± 0.1°C by an external jacket on the cells through which a coolant fluid maintained by a cryostat that cools the working fluid. The cell was composed of two compartments: the charging side and the detection side, joined by a thin sample sheet. In this work, two configurations of the sample exposure area were evaluated: the "small configuration" with the charging side exposure was 1.13 cm^2, while the detection side exposure was 1.02 cm^2. The second one, "large configuration", involved 4.52 cm^2 for the charging side and 4.08 cm^2 for the detection side. In both cases it was guaranteed the 90% area reduction between the two compartments as prescribe by standard. The activated titanium counter-electrodes separate by a porous diaphragm from the adjacent environment were foreseen for each compartment. The silver \silver-chloride (3M KCl) and saturated calomel reference electrode were used in detection and charging side respectively. The metal sheet was used as the working electrode. The detection side was filled with a 0.1 M sodium hydroxide solution, which was aerated under stagnant conditions. The charge compartment utilized a circulated and deaerated carbonate–bicarbonate solution. This compartment was equipped with a solution recirculation system driven by an electric pump, connected to a 5-litre carbonate–bicarbonate solution reservoir. The circulating solution was positioned near the specimen surface to counteract the diffusion of alkalinization effect caused by cathodic polarisation. In this way, the solution, maintained at a controlled pH, gently contacts the surface, while the overflow valve discharges the solution to the opposite side of the cell into the reservoir, minimizing alkalinization within the circulating solution as stated by Nagumo [19]. The reservoir and the charge compartment were

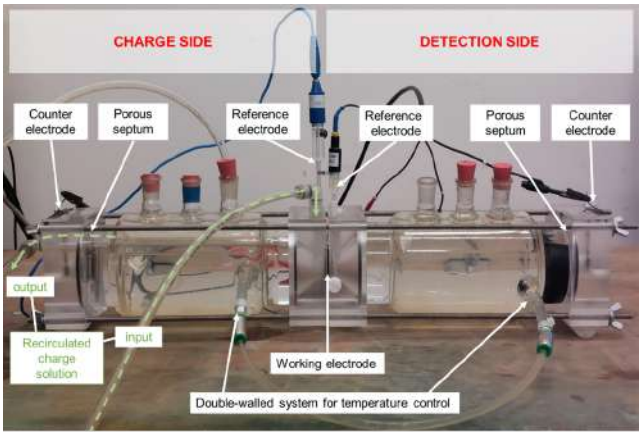

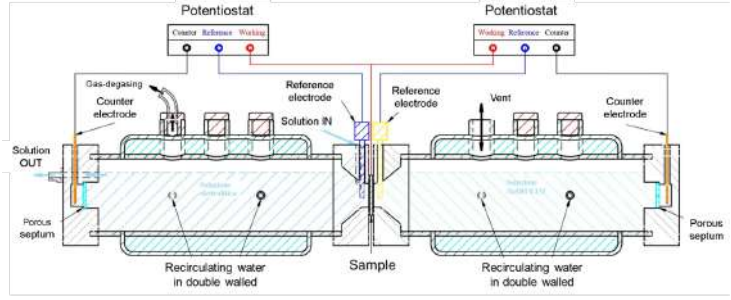

Figure 5.2: Permeation cell setup used in this work, based on the Devanathan and Stachurski configuration. Real experimental setup and schematic draw. This setup was adopted for both configurations, it was replaced the junction near to the sample for modifying the exposed area (large and small configuration).

deaerated by bubbling nitrogen (the oxygen concentration was reduced to about 0.04 ppm).

Experimental procedure of permeation tests

The experimental procedure involved in different phases. The specimen, short-circuited to the two potentiostat, is placed between the two compartments of the semi-cells. A constant potential of +0.340 mV vs Ag|AgCl (3M KCl) is applied on detection side filled with NaOH 0.1 M, inducing the formation of a passivation layer the specimen's surface, which serves as the anode in the electrochemical cell. This step was concluded when the current density measurement reaches the threshold value of 0.05 μA/cm^2 which guarantee a resistant and stable passive layer. This value was determined as a more restricted value that suggested by standard ISO 1081 (0.1 μA/cm^2).

Once the passivation phase is complete, the charging side is activated. The circulating pump filled the semi-cell with the deaerated carbonate–bicarbonate solution from reservoir. A constant current density of -0.50 μA/cm^2 was applied by galvanostat. Hydrogen is formed on the cathode surface, which, through adsorption and absorption mechanisms, penetrates the metal sheet and diffuses to the discharge side. The circulating current on the detection side was measured, and the permeation process was considered complete when a stable and stationary current value was recorded in the detection side.

Subsequently it was imposed several cathodic current values on charging side, as shown in Table 5.1, performing different rise and decay permeation transients.

Table 5.1: Example of polarisation applied on charging side during step of permeation tests.

Step Number		Cathodic current density imposed
		$[mA/cm^2]$
-	0	-0.0051
Rise	A	-0.051
Rise	B	-0.51
Rise	C	-5.1
Decay	D	-0.51
Decay	E	-0.051
Decay	F	-0.0051

Starting from step 0, which serves to reach a low current level as starting point from end of the permeation transient, increasing currents are applied in the subsequent

steps, followed by decreasing currents, maintaining the applied condition until a steady state is achieved, typically within 3000 s.

5.3 Theory and calculation for permeation tests

5.3.1 Estimation of apparent diffusion coefficient

The diffusion coefficients can be estimated from the discharge curve of hydrogen uptake tests, following the approach outlined in [165] and the method described in the [157] Section 4.2. This method using a data-driven optimization on electrochemical discharge curve, which is also valid in cases where hydrogen is lost prior to the start of electrochemical discharging (waiting time).

Alternatively, diffusion coefficients can be determined from permeation transients through tests in Devanathan and Stachurski cell. Liu et al. [58] proposed a way to fit the permeation transient using Equation (5.1) for rise transient and Equation (5.2) for decay transient (steps tests).

$$\frac{i_t - i_0}{i_\infty - i_0} = \frac{2L}{\sqrt{\pi D t}} \sum_{n=0}^{\infty} e^{\left(-\frac{(2n+1)^2 L^2}{4 D t}\right)} \tag{5.1}$$

$$\frac{i_t - i_\infty}{i_0 - i_\infty} = 1 - \frac{2L}{\sqrt{\pi D t}} \sum_{n=0}^{\infty} e^{\left(-\frac{(2n+1)^2 L^2}{4 D t}\right)} \tag{5.2}$$

The decay transient is modelled assuming that the discharged hydrogen exits only on the anodic side of the cell, and desorption effects on the charging side are neglected, with the diffusive flux maintained in the same direction as the permeation flow.

This approach involves the application of an explicit Laplace method to the transient permeation current density measured on the detection side of a sheet sample with thickness L. Here, i_t represents the measured hydrogen permeation current density at time t, i_0 is the initial steady-state hydrogen permeation current density at the start of the transient, and i_∞ is the steady-state hydrogen permeation current density as t approaches infinity. Via MATLAB code was estimated the diffusion coefficient D as numerical iteration.

5.3.2 Estimation of hydrogen uptake and fugacity

The hydrogen uptake, as concentration in stationary conditions within the sub-surface region of the specimen after electrochemical charging, can be estimated both through

hydrogen uptake tests and permeation tests. By the first one method, converting the discharge current subtracted of passivation current, in concentration via Faraday's law and fitting them with experimental data as describe in Section 4.2 and [157, 165].

As for the permeation tests, the stationary hydrogen concentration in the sub-surface on the charging side was estimated using the average stationary current density at the end of each rise and decay ideal transient of the permeation process on exit side. In fact, in an ideal electrochemical hydrogen permeation experiment [166], the hydrogen concentration at the entry surface is directly related to the steady-state current density. In this case the Fick's law, in Equation (5.3), describe the diffusion process and it was possible to apply the formulation presented in [167].

$$\varphi = -D \cdot \nabla C \tag{5.3}$$

The flux φ can be expressed, according to Faraday's law, as being proportional to the stationary current density i_∞ measured on the detection side. Thus, considering the concentration gradient ∇C one dimensional, it was derived the finite hydrogen concentration difference ΔC_H in Equation (5.4) equation *(3.4)*.

$$\Delta C_H = C_0 = \frac{\frac{i_\infty}{F}}{D} \cdot L \tag{5.4}$$

D was apparent diffusion coefficient and L was sample thickness. The hydrogen concentration difference, across the thickness of the metal sheet corresponds to the hydrogen uptake on the charging side C_0. In fact, theoretically all atomic hydrogen diffused to the detection side is recombined into molecular hydrogen, thereby maintaining the hydrogen concentration on the detection side at zero. As a result, the concentration difference matches the charged concentration (hydrogen uptake) on the charging side. This equation was valid if hydrogen absorption at the entry surface was free, there was absence of trapping phenomena in the metal lattice and without obstacles on egress side.

Under the condition of reaching steady state during permeation tests, as previously discussed, Fick's law in Equation (5.4) can be applied, along with Sievert's law as given in Equation (1.13). By equating the concentration terms C_0 the relationship between the steady-state permeation flux and the fugacity, as shown in Equation (5.5), is obtained.

$$i_\infty = \frac{FD}{L} \cdot S \cdot \sqrt{f_{eq}} \tag{5.5}$$

The Sievert constant S, was estimated by literature. Thus, the equivalent hydrogen fugacity during electrolytic charging can be derived.

5.4 Experimental results

5.4.1 Results by hydrogen uptake tests

The analysis of the anodic discharging current curve, as presented in Figure 5.3, was carried out following the procedure described in Sections 4.2 and 4.3.1 and Appendix A.

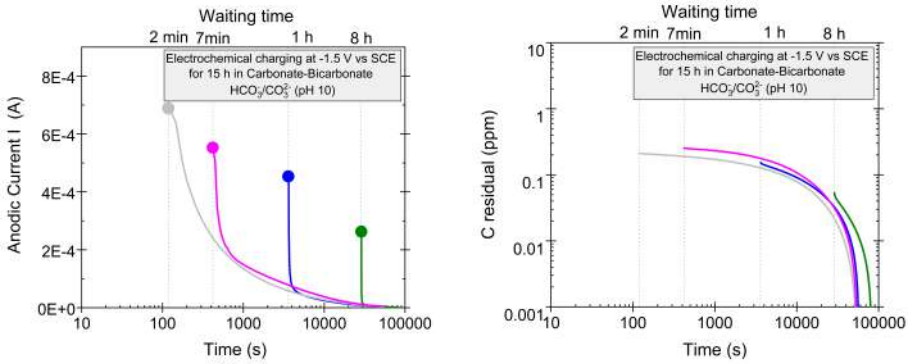

(a) Anodic discharging current curves moved to correct waiting time before starting electrochemical discharging.

(b) Residual average concentration egress from sample during electrochemical discharging.

Figure 5.3: Results from the hydrogen uptake test on steel A.

During electrochemical desorption, the decreasing current associated with hydrogen egress was measured (Figure 5.3-a). It was observed that, with increasing waiting time, the initial point of the curve shifted downwards, despite identical charging conditions, as indicated by the marked points on the curves in Figure 5.3-a. The integral of the discharging current provides the egress charge, which can be converted into residual hydrogen concentration $C_{residual}$ using Faraday's law obtaining the trend in Figure 5.3-b. The variation of concentration was attributed specifically of diffusional hydrogen, because it was mobile in the lattice during discharging.

The integral of this curve, representing the hydrogen flux egress during electrochemical discharging, provides an estimate of the diffusible hydrogen quantity within the sample, as shown in Figure 5.4 (cross symbols).

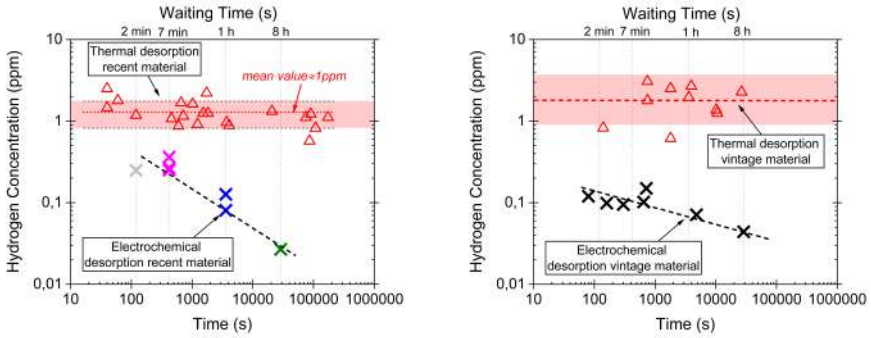

(a) Comparison of results for steel A. **(b)** Comparison of results for steel B.

Figure 5.4: Comparison between the variation of diffusible hydrogen concentration as a function of waiting time and the total hydrogen concentration measured via LECO analysis.

These values were compared with the total hydrogen content in the sample, measured via Leco analysis at 1250 °C (triangle symbols), defined as irreversible and reversible hydrogen quantity. During spontaneous desorption (waiting time) in air at room temperature, only the diffusible hydrogen is expected to be released. As a result, after a relatively short period (approximately 7 minutes of waiting time), the diffusible hydrogen concentration decreases to about one third of the total value. In fact, on similar materials the activation of irreversible traps can be observe at 240°C while the reversable one, which promote diffusible hydrogen phenomena, already 30°C or below [168]. The total hydrogen measured was not affected by the waiting time, while the electrochemically measured diffusible hydrogen was and resulting in a high desorption rate. During the thermal analysis, the variation in the amount of diffusible hydrogen lost relative to the total hydrogen content was minimal. Therefore, the quantity of total hydrogen was significantly greater than the diffusible hydrogen.

In a comparative analysis with the steel B Figure 5.4, it was observed that the total hydrogen measured via LECO analysis is significantly higher, which can be attributed to the differences in microstructure, being more heterogeneous. Moreover, the hydrogen egress during the waiting time exhibits a slower behaviour. This phenomenon is also ascribed to the distinct microstructural characteristics, as further confirmed by the diffusion coefficient estimations discussed subsequently.

5.4.2 Results by permeation tests

Summary of test curve

The result of a complete permeation test was showed in Figure 5.5.

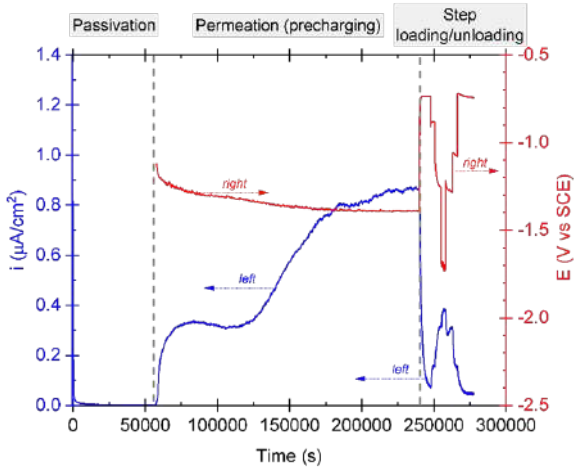

Figure 5.5: Total curve of permeation test composed by passivation, precharging permeation and step charging/discharging.

First, the detection side was passivated to measure the contribution of passivation, which is then subtracted from the current of subsequent transients. The current density decreasing in time as formation the stable passive film. After which permeation transient was executed. This phase exhibited a double knee, which is typical of permeation transients in steel characterised by traps effect due to inclusion or second phases. The permeation was employed to saturate the irreversible traps and minimising it the effect, as reported in the literature [58, 73, 74] thus working as precharging. In this way the trapping effect was neglecting and considering only the diffusible hydrogen flux. In the end, the sheet metal was characterised for rise and decay transient by diffusible flux. The loading/unloading step was executed by different current impose on charging side.

As shown in Figure 5.6, a decay transient was applied to reach a lower current density value (I_0).

In this way, a wider current range could be applied during step of loading/unloading. Thus, the permeation flux measured during the step stayed below the steady-state permeation value reached at the end of the precharging. Therefore, no additional trap

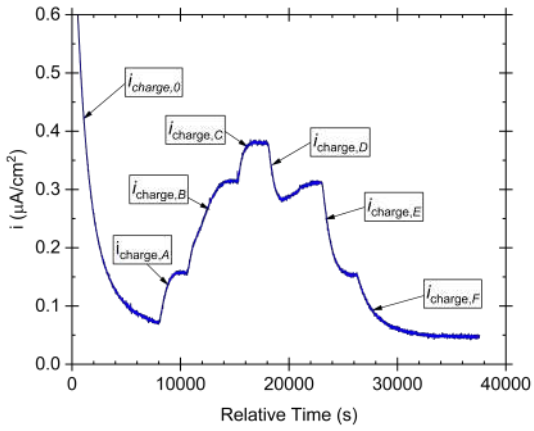

Figure 5.6: Step charging/discharging curve; current imposed on charging side are: $I_0 = 0.0051$ mA/cm^2, $I_A = 0.051$ mA/cm^2, $I_B = 0.51$ mA/cm^2, $I_C = 5.1$ mA/cm^2, $I_D = 0.51$ mA/cm^2, $I_E = 0.051$ mA/cm^2, $I_F = 0.0051$ mA/cm^2.

sites were activated during the final phase of this test. Several upward and downward transients were performed. Increasing on the charging side ($I_{charge,A}$ to $I_{charge,C}$) the current value, increase the measured current on detection side due to increase of variation of diffusible hydrogen flux. At the same behaviour it was observe during decay strategy (by $I_{charge,D}$ to $I_{charge,F}$). Using this strategy, it was possible to perform several permeation transients, allowing for the execution of multiple permeation tests in a consistent manner. Additionally, this approach ensured high reproducibility of the transients. By normalizing the transients according to Equation (5.6) with the steady-state current density i_∞ and the initial current density transient value i_0, the rise and decay transients were successfully overlapped and reproducible as shown in Figure 5.7.

$$\widetilde{i} = \frac{i_t - i_\infty}{i_\infty - i_0} \tag{5.6}$$

As can be seen, the first transient permeation (precharge), represented by black cross symbols in the graph, deviated from the trend observed in the subsequent steps, while the other steps were reproducible.

Dimensional effect of exposed area on charging side

The influence of the exposed charging area is evaluated in Figure 5.8.

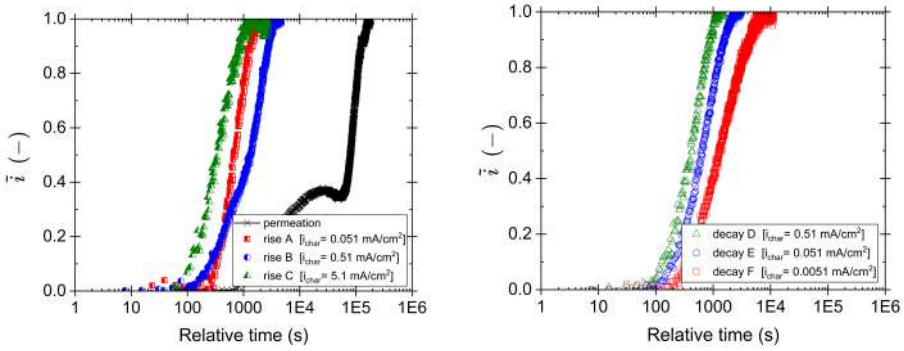

(a) Normalized rise transient. **(b)** Normalized decay transient.

Figure 5.7: Normalised rise and decay transients $\widetilde{i}$ of charging/discharging step.

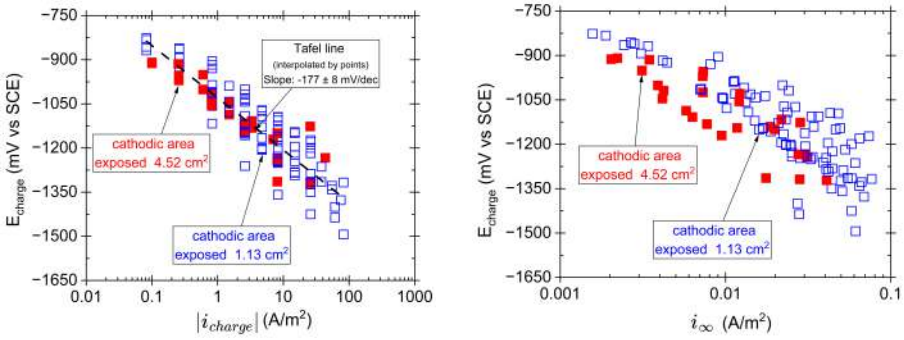

(a) Charging current density applied side versus cathodic potential on charging side. **(b)** Stationary current density estimated on detection side versus cathodic potential on charging side.

Figure 5.8: Comparison between the two configurations with same superficial condition and different exposed charge area.

Both configurations had similar trends. However, as shown in Figure 5.8-a, when using the "larger configuration" which is four times charge area greater than the smaller one, the cathodic current density versus polarization data were closer to the cathodic Tafel line and the data exhibited less dispersion. Moreover, the large area of charging allows to promote the removal of hydrogen bubbles developed on surface better than the small configuration. Thus, the recirculating jet near the surface helps mitigate the shielding effect induced by hydrogen bubble formation. The nature of the bubbles and the extent of the shielding are influenced by the surface potential, illustrating how an increase in potential enhances bubble growth and coalescence, which in turn obstacles the current fields from reaching the sample [169]. Consequently, the large configuration allows to produce a greater amount of hydrogen on charge side. As a result, an increase in the total current signal is observed on the detection side. Although the current density is comparable in the two configurations, in the large configuration the signal is easier to detect reducing the dispersion of results (Figure 5.8-b). In this case, the stationary current density at the end of each permeation step, during both the rise and decay phases, exhibited less dispersion with the larger configuration.

Palladium coating on the exposed surfaces effect

The effect of palladium coating on the surface, applied through electrochemical deposition, was investigated in Figure 5.9 for two cell configurations.

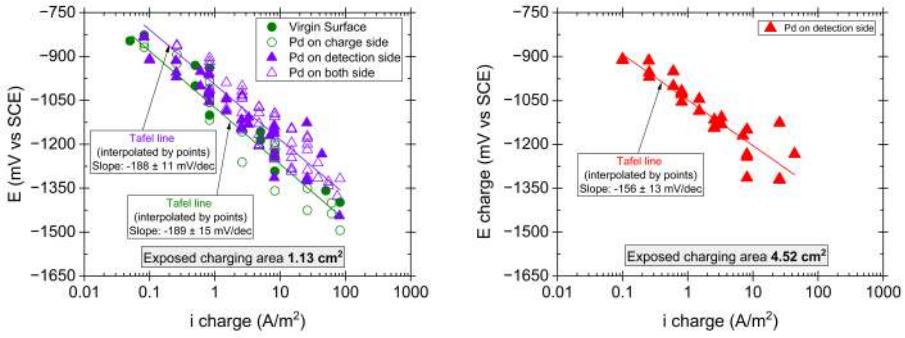

(a) Small charge exposed area. **(b)** Largest charge exposed area.

Figure 5.9: Effect of electrochemically deposited palladium coating on small and large exposed charge areas. Polarisation curves were recorded after completion of Pd deposition, in a charging electrolyte without Pd^{2+}, so that only the hydrogen evolution reaction (HER) was active and measurements were not performed during plating.

About the cell with 1.13 cm^2 of exposed area, the cathodic trend on the charging side highlighted the influence of the palladium coating on the applied potential. In the case of a virgin surface (no coating) or when the coating was applied only to the charging side, the same Tafel line was observed (Figure 5.9-a, circle symbol). However, tests with palladium coating on the detection side or on both sides ((Figure 5.9-a, triangle symbol) exhibited similar behaviour. In both cases, the Tafel slope is close to -180 mV/decade, aligning well with the characteristic behaviour of the hydrogen evolution reaction kinetics in alkaline electrolytes [170, 171]. For alkaline environment higher than pH 10, the Tafel slopes typically reaching values between 140 and 165 mV/dec. For iron, the Tafel slope approaches 180 mV/dec under these conditions, reinforcing the notion that HER kinetics remain relatively stable and unaffected by pH changes within this range.

Applying the coating only to the charging side was not beneficial, as cathodic debonding compromised the integrity and stability of the film, limiting its positive effect. The impact of the palladium coating on the detection side was more pronounced, as it facilitated the egress of the hydrogen flux, as shown in Figure 5.10. Under the specified conditions in the small configuration, this resulted in a variation of approximately one order of magnitude.

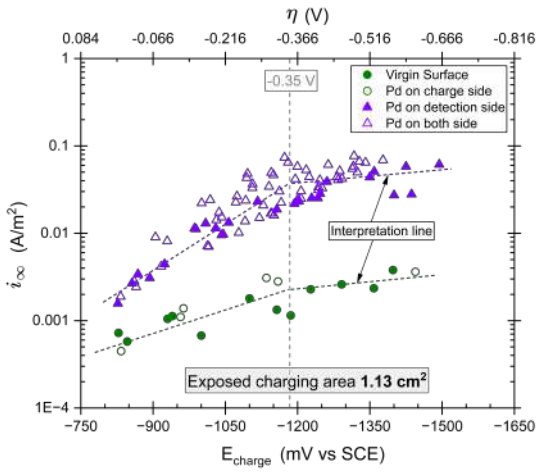

Figure 5.10: Stationary current density measured during step loading/unloading in different palladium cover conditions.

Thus, the kinetics on the discharge side changed as demonstrated by shifting of Tafel line that maintaining the same slope (Figure 5.9). Nevertheless, coating both

sides was not advantageous because the palladium effect on the charging side did not enhance hydrogen entry due to the cathodic debonding. The same results about palladium coating on detection side were observed for the cell with largest charging exposed area as indicated in Figure 5.9-b.

The differences by effect of palladium coating were attributed to the presence (or absence) of an iron oxide layer on the detection side, which represents the main impediment to permeation. An explanation of that can be the hydrogen concentration in the metal at the metal-oxide interface is nearly equal to the hydrogen concentration at the charging side of the metal. The activation energy for hydrogen diffusion in the passivating oxide on iron, is higher than that in metallic iron, due to the Coulombic interaction between atomic hydrogen and partially hydrated and electronegative iron oxide layer [172, 173]. It is well established that the concentration ratio of hydrogen across the metal–oxide interface depends on the electrical potential drop and on the ratio of the hydrogen activity coefficients in the two phases [172, 174]. The electrical potential drop reflects the difference in the chemical potential of electrons between the metal and the oxide [172]. The comparison of the hydrogen flux on the egress side, with and without a palladium coating, confirms that the native oxide layer on the surface limits hydrogen transport [175, 176], as the palladium layer reduces the energy barrier associated with the oxide. The presence of a palladium coating therefore approximates the behaviour of an ideal oxide-free steel surface for hydrogen uptake [177]. Additionally, palladium coating guarantees the equilibrium between the hydrogen and metal surface in agree with Sieverts' law [175, 178]. Moreover, the trend in every case investigated in Figure 5.10, shown a double slope of interpretation line at -0.35 V of overpotential defined as Equation (1.7), Equation (1.8) and in accordance with literature Bockris's works [47, 59]. In conclusion was better largest configuration with palladium coating only on detection side.

5.5 Discussion of results

5.5.1 Diffusion coefficients

Average diffusion coefficient estimated by hydrogen uptake test

To estimate the average apparent diffusion coefficient associated with spontaneous desorption in air at room temperature, the data-driven optimisation approach must be employed (Chapter 4). The target curve was constructed by normalizing the simulated data curves both time $\widehat{T}$ and concentration $\widehat{C}^*(t)$ according to equations Equation (4.6)

and Equation (4.7). This curve is independent by the diffusion coefficient and the initial concentration as previously discussed.

Normalising the average residual hydrogen concentration (Figure 5.3-b) with appropriate waiting time t_0, the diffusion coefficient D and the initial concentration charged C_0^*, it was possible to overlapped fitting the experimental data with target curve via MATLAB fitting procedure (Figure 5.11). Moreover, it was automatically estimated the initial hydrogen concentration charged and waiting time.

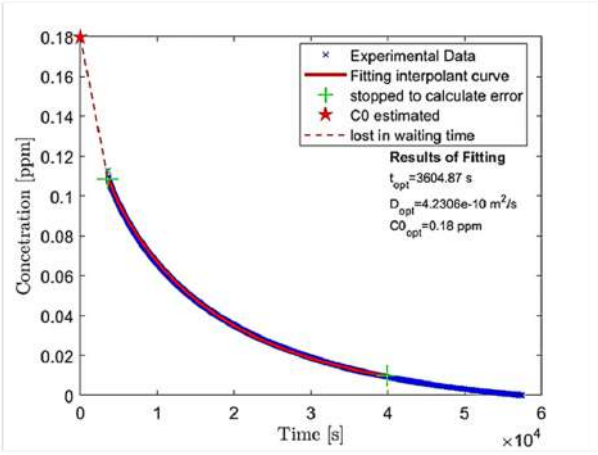

Figure 5.11: Example of data driven optimisation in MATLAB of experimental test with 1h of waiting time.

The average apparent diffusion coefficient in steel A was $4.4 \cdot 10^{-10}$ m^2/s, as shown in Figure 5.12 and comparable to previously estimated in Section 4.3.3.

This parameter remained constant for each test and was independent of the waiting time. The same cathodic charge condition at -1.5 V vs SCE involves in the same amount of hydrogen absorbed. Therefore, during spontaneous desorption in the atmosphere, executed in the same conditions for each test, implicates in reproducible hydrogen loss process. Furthermore, in the anodic discharging step, only diffusible hydrogen can diffuse from the sample due to the experimental conditions employed in this study thank the saturation of the sample during the charge. Therefore, the estimated value represents the average spontaneous attitude of hydrogen freely moving within the metal lattice at room temperature and atmospheric pressure. Maintaining room temperature throughout the testing minimizes the interaction between diffusion and trapping phenomena. Hydrogen trapped in irreversible traps during the charging phase

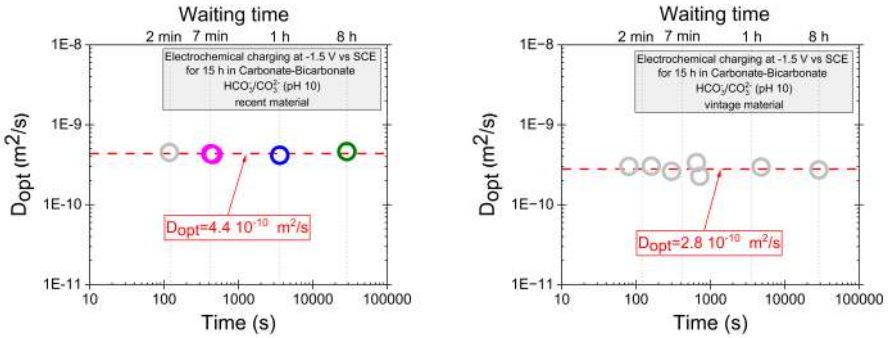

(a) Apparent diffusion coefficient of steel A. **(b)** Apparent diffusion coefficient of steel B.

Figure 5.12: Apparent diffusion coefficients estimated by the data-driven optimisation approach as a function of the waiting time in atmosphere prior to electrochemical discharging for the steel A and B.

is not released during discharge and does not participate in the spontaneous diffusion process.

Generally, the activation energy for reversible and irreversible traps of trapping and detrapping phenomena, are primarily temperature-dependent which must be at least 50-100 °C higher for the first peak in a TDS analysis [159, 160, 179]. Moreover, as described in a previously Chapter 4, this parameter estimated by hydrogen uptake tests depends on the structure of material, the presence of inclusions, and vacancies that influenced the metal lattice.

This interpretation is supported by the comparative analysis with the results obtained for the steel B. In this case, the apparent diffusion coefficient is approximately half of that measured for the steel A Figure 5.12. This reduction can be attributed to the reduced mobility of hydrogen within a microstructure that is more heavily influenced by defects and inclusions. As a consequence, the spontaneous apparent diffusion coefficient decreases, reflecting the slower transport of hydrogen through the steel B.

Apparent diffusion coefficient estimated by permeation tests

The diffusion coefficient was evaluated by the loading/unloading phases of the permeation transient. Each transient was analysed individually and expressed in relative terms by subtracting the initial or final value, thereby setting the start or end point to zero for rise and decay transients, respectively. The relative current density of permeation was fitted by iteratively selecting the diffusion coefficient and applying Equations (5.1)

and (5.2), minimizing the error between the fitted curve and the experimental data as shown in Figure 5.13.

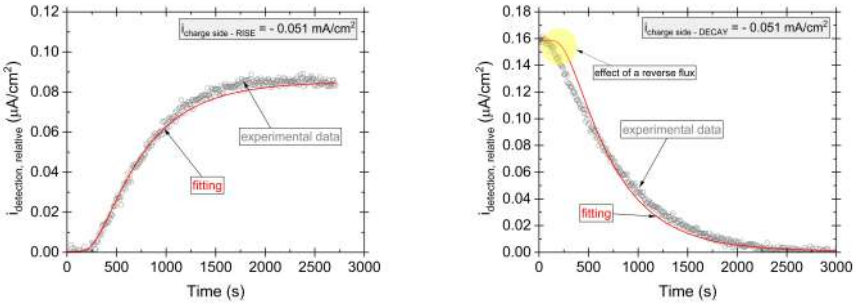

(a) Rise transient fitting. **(b)** Decay transient fitting.

Figure 5.13: Example of experimental data fitting applying the Laplace method in both transients of the loading/unloading step of the permeation test.

This approach provided satisfactory results for the rising transient. However, the decay transient was affected by discrepancies observed at the initial knee of the curve. During the decay phase, the applied polarisation was reduced, leading to a transient redistribution of hydrogen at the entry side. As a result, the boundary conditions potentially could induce a small reverse flux on the opposite side. This aspect was not modelled, in fact the decay transient represents the complementary of rise transient. However, in all testing conditions was applied this method to estimate the apparent diffusion coefficient D_{app} (Figure 5.14).

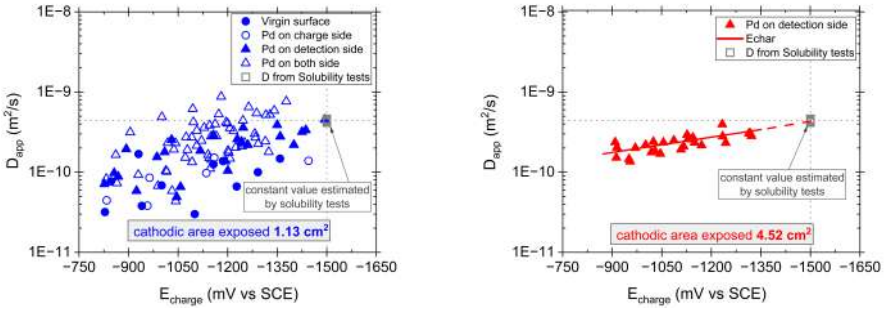

(a) Small charge area configuration. **(b)** Large charge area configuration.

Figure 5.14: Diffusion coefficients estimated via the Laplace method (Liu et al.) for different charge area exposed in the permeation cell configurations.

The apparent diffusion coefficient estimated by cell with a smaller charge-exposed area (Figure 5.14-a) was strongly affected by the charge potential applied. Moreover, the effect of the palladium coating on the surface influences the estimation of the diffusion coefficient. For the virgin surface and the palladium coating on the charge side (represented by the blue circle symbols) resulted in greater variation in the diffusion coefficient. The egress of hydrogen flux was limited by the presence of an oxide layer on the detection side (without palladium), thereby deviating from ideal conditions. While the case where the palladium coating was on the detection side or on both sides (represented by the blue triangle symbols) shown a more restricted variation.

Increasing the surface area improved reproducibility (Figure 5.14-b) by increasing the current signal, thereby reducing variability in the estimated parameters. However, the apparent diffusion coefficient was comparable across different configurations cell thank the experimental apparatus that limited the alkalinisation effect (not in direct contact with the sample surface) via recirculating the buffered high pH solution on charge side.

Comparison of the apparent diffusion coefficient estimated via permeation cell measurements with that obtained from hydrogen uptake tests at the same applied potential (empty squares symbols in Figure 5.14), the value coincides with projection of trend of diffusion coefficient estimated at -1.5 V vs SCE. This potential was not investigated with the permeation cell, as high cathodic potentials cause hydrogen bubbles shielding, which masks the surface and limits the hydrogen reaction, thereby restricting the flux. The trend of diffusion coefficients in function of charge potential applied, was predicted by Griffiths and Turnbull [180, 181] through theoretical calculations, investigating the relationship between hydrogen concentration and apparent diffusion coefficient. It was commonly known that the concentration is proportional to permeation flux, thus a comparable concentration dependence by diffusion coefficient. In this case, if it is considered the diffusion coefficient as concentration dependant parameter, should not be regarded as an intrinsic material property unless the occupancy of trapping sites is negligible [181]. In this case, efforts were made to minimize the disturbance of the equilibrium between lattice hydrogen and trapped hydrogen by applying a full double-step precharging permeation sequence, aiming to limit variations in trap site occupancy [182]. Resulting in more stable trend value of coefficients respect to polarisation as shown in Figure 5.14-b. Nonetheless, even under conditions with limited changes in trap occupancy, the influence of reversible traps was not entirely eliminated maintaining the slightly dependence by polarisation of partial transients.

5.5.2 Estimation of hydrogen uptake and fugacity

Hydrogen uptake

The initial hydrogen concentration at the end of electrochemical charging (hydrogen uptake) was determined by extrapolating the normalized discharging curves at various waiting times to the initial instant. For different waiting times, the hydrogen uptake remained constant as shown in Figure 5.15.

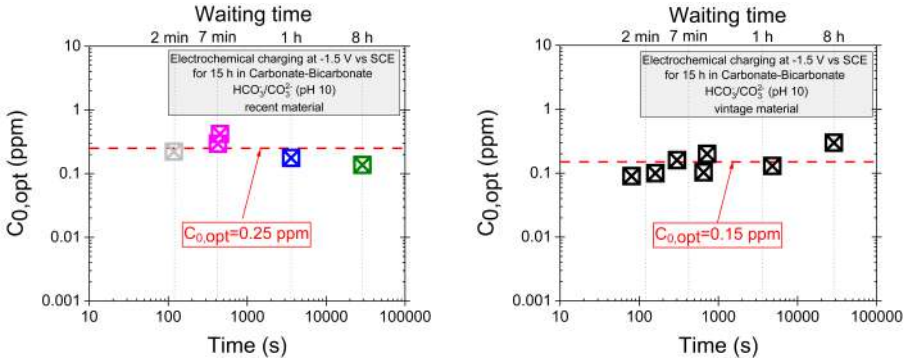

(a) Initial hydrogen concentration for steel A. **(b)** Initial hydrogen concentration for steel B.

Figure 5.15: Extrapolation of the initial hydrogen concentration (hydrogen uptake) via the data-driven optimisation approach applied to hydrogen uptake tests for different materials.

At the same charging conditions, in terms of both duration and applied polarisation, the hydrogen production mechanism on the surface was reproducible. Consequently, the hydrogen coverage was similar for all samples, and therefore the amount of hydrogen adsorbed and absorbed during charging is expected to be equivalent across specimens. This behaviour is also confirmed for the steel B. In this case as well, the hydrogen uptake remains constant as a function of the applied polarisation.

Hydrogen concentration and Fugacity

To apply the Sievert theoretical relation described in Equation (1.13) and Equation (5.4) to the permeation tests, a linear relationship must exist between the steady-state hydrogen current density and the square root of the current density imposed on the charging side [49, 58], as demonstrated in Figure 5.16 for the small configuration cell.

This condition is not satisfied when the virgin surface or palladium is present only on the charging side. In these cases, the egress side covered by oxide mitigates the hydrogen flux (as previously describe Section 5.4.2) and the Fick's Law is not properly

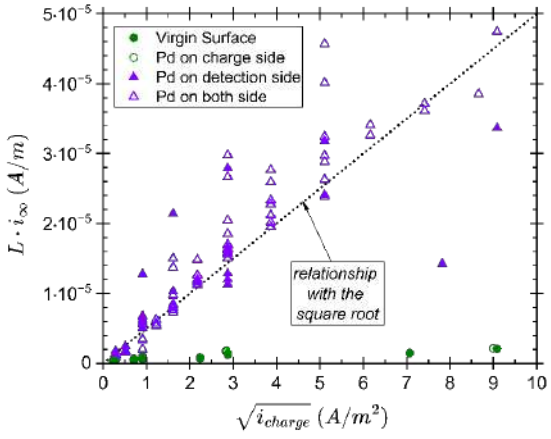

Figure 5.16: Steady–state current density from step charging/discharging permeation tests, multiplied by the sheet sample thickness, as a function of the square root of the imposed charging current density in a small configuration cell under different boundary exposure conditions.

applicable. However, this condition is satisfied when palladium coatings are applied to the detection side or to both sides, due to the higher hydrogen flux involved in these configurations and the more reproducible reactions occurring on charging and detection sides. This suggests that, for the latter two cases, the charging potential and hydrogen concentration estimated using Equation (5.4) based on sheet thickness as shown in Figure 5.17 should be correlated.

This observation aligns with theoretical predictions and supports the findings of literature [59, 109, 183]. Moreover, the hydrogen uptake values estimated through data-driven optimisation of hydrogen uptake tests are consistent with the concentrations obtained from permeation tests (indicated by the grey square cross in Figure 5.17). At the corresponding applied polarisation, the concentrations show good agreement.

The results were consistent with permeation tests simulating the absence of an iron oxide layer on the detection side (presence of palladium on detection side). This can be explained because, during the charging phase of the hydrogen uptake tests, the oxide layer on the sample surface is reduced [184]. As a result, during the initial stages of the discharge phase, hydrogen flux egress was not limited, making the conditions equivalent to those of permeation tests with palladium on the detection side. The oxide layer subsequently reforms during the discharge phase as a passivation film [184]. However, the majority of hydrogen flux egress occurs during the initial stages of discharge. In any

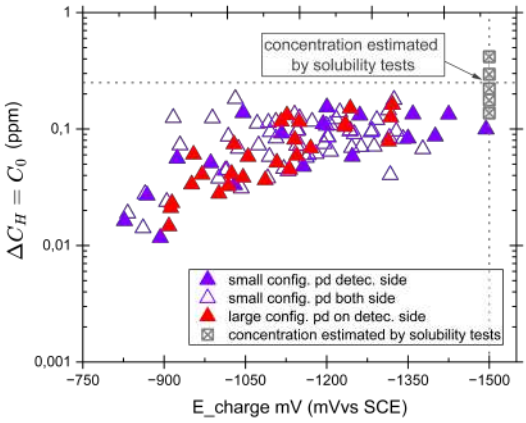

Figure 5.17: Hydrogen concentration determined from permeation tests in small and large charge side configuration cells under different boundary exposure conditions.

case, the contribution of the passivation current was subtracted from the current measured during the discharge phase, thereby compensating for this effect when estimating the current component attributable to hydrogen transport. Additionally, the permeation step of charging and discharging involved relatively rapid changes in cathodic charging conditions during the permeation tests. In fact, the different steps reached only a small plateau, indicating a short steady–state condition that may not have been entirely stable. For longer test durations, variations in flux could be observed due to differing degrees of trap saturation. Furthermore, the hydrogen charging methods differ between the two tests: the hydrogen uptake tests were conducted under potentiostatic control, whereas the permeation tests employed galvanostatic charging. The efficiency of hydrogen entry under potentiostatic conditions appeared to be lower than that under galvanostatic charging [185].

To estimate the fugacity via Equation (1.13), the Sieverts constant must first be determined. Its value reported in the literature is variable, as summarised in Table 1.1. For steel X65, which is very similar to the material studied, a Sieverts constant of $1.25 \cdot 10^{-2}\,\mathrm{wppm}/\sqrt{\mathrm{bar}}$ [74] was assumed. This value was obtained using a modified Devanathan–Stachurski cell, in which hydrogen gas was charged on one side and the flux was discharged electrochemically on the other, thereby establishing a direct relationship between the hydrogen gas pressure during charging and the electrochemical discharge. The steady-state current density and apparent diffusion coefficient resulting

at each step of the loading/unloading process, the equivalent fugacity was calculated from Equation (5.5), as shown in Figure 5.18.

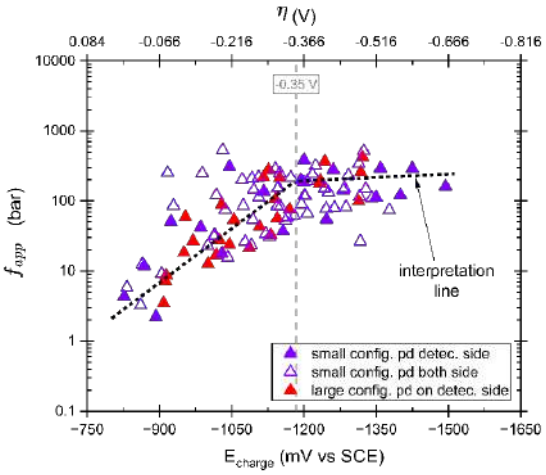

Figure 5.18: Apparent fugacity for Steel A estimated using a Sievert constant of $1.25 \cdot 10^{-2}\,\mathrm{wppm}/\sqrt{\mathrm{bar}}$ [74].

Increasing the polarisation on the charging side leads to an increase in fugacity. Notably, at an overpotential of -0.35 V, the slope of the interpretation line changes, in agreement with literature findings based on Bokris [59, 61] and Liu et al. [58]. Considering the possible combinations of the reaction steps represented by Equation (1.9) to Equation (1.11). Hydrogen evolution mechanism involving a coupled electrochemical discharge and chemical recombination process (coupling of Equation (1.9)-Equation (1.10)) at low overpotentials (<0.35 V). At higher overpotentials (>0.35 V), however, rapid electrochemical discharge (Equation (1.11)) becomes increasingly significant.

When comparing our results with those reported in the literature, the observed trend aligns well, as illustrated in Figure 5.19. This was consistent with the observed trend of variations in hydrogen concentration within steels, where a more negative charging overpotential enhances the hydrogen fugacity at the steel surface, leading to an increased quantity of hydrogen being absorbed into the steel [186] confirming relation explained in Equation (1.13). The fugacity values estimated was coherent with those reported for similar materials in literature [58, 59, 186–188]. The dispersion of the data with respect to the literature may also be attributed to variations in the Sieverts constant reported in different studies.

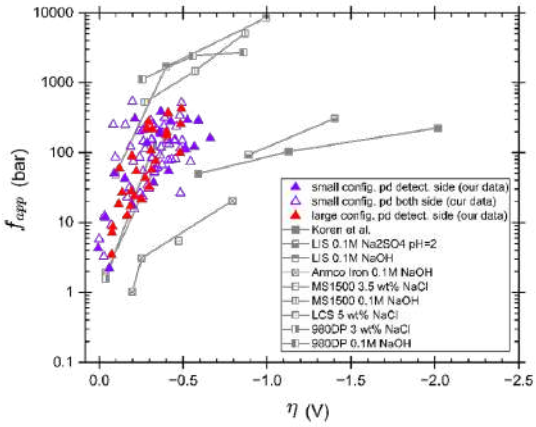

Figure 5.19: Comparison of apparent fugacity estimated using a Sieverts' constant of $1.25 \cdot 10^{-2}\,\mathrm{wppm}/\sqrt{\mathrm{bar}}$ [74] with literature data.

5.6 Equivalence between electrochemical and gaseous hydrogen

5.6.1 Evaluation of equivalent hydrogen pressure

By deriving the equivalent fugacity as a function of the applied potential, as shown in Figure 5.18 for the steel A, it is possible to experimentally estimate an equivalent hydrogen pressure corresponding to a given cathodic polarisation.

For a cathodic potential of -1.050 V vs SCE, the steel A exhibits an equivalent fugacity corresponding to approximately 150 bar. This value can be considered as the equivalent hydrogen pressure because, as described in Section 1.3.1, at low pressures (up to about 200 bar) fugacity and pressure are effectively identical. Therefore, the hydrogen-related effects induced electrochemically at this potential can be regarded as comparable to those obtained under gaseous hydrogen charging at around 150 bar.

$$[H]_{\text{cathodic}} - 1.050\ \text{V (vs SCE)} \iff [H]_{\text{gas}} \approx 150\ \text{bar of } H_2$$

5.6.2 Data-driven modelling applied to gaseous hydrogen charging

To evaluate and correlate the effects of gaseous and electrochemical hydrogen charging, a hydrogen uptake test was carried out in an autoclave at a hydrogen pressure of 150

bar. A cylindrical specimen, with the geometry reported in Chapter 4, was used, and the analysis was conducted by applying the data-driven optimisation procedure described in the same reference.

In this case, the specimen was charged with gaseous hydrogen in the autoclave for 25 hours to ensure full saturation, as assessed using the apparent diffusion coefficient previously estimated from electrochemical charging. Once the charging period was completed, the specimen was discharged electrochemically following the procedure described in Chapter 4. The only difference with respect to the earlier electrochemical tests lies in the charging phase, which was performed in gaseous hydrogen instead of by cathodic polarisation.

Figure 5.20 shows the evolution of the residual hydrogen concentration, obtained by electrochemical discharge after gaseous hydrogen charging.

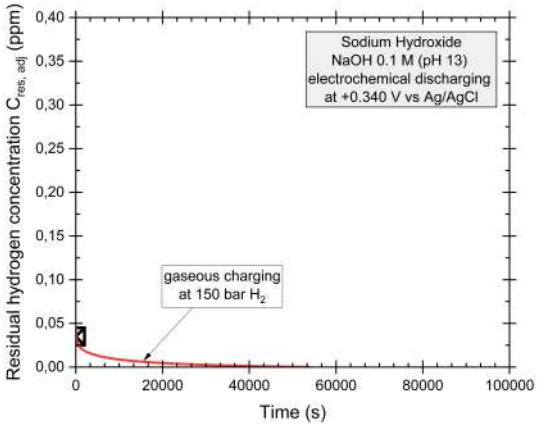

Figure 5.20: Residual hydrogen concentration estimated by electrochemical discharge after gaseous hydrogen charging.

The results are consistent with those obtained under electrochemical charging, independently of the charging environment, as previously discussed. In particular, the values are comparable to those obtained under a charging potential of -1 V vs SCE, which is the closest electrochemical condition to the equivalent cathodic potential considered. It was necessary to account for spontaneous desorption occurring during the time required to depressurise the autoclave and transfer the specimen to the electrochemical cell (approximately 20 minutes). The parameters used for this correction are reported in Table 5.2.

Table 5.2: Estimated waiting time, apparent diffusion coefficient, and hydrogen uptake for gaseous hydrogen charging.

Waiting time (WT) (s)	**Apparent diffusion coefficient** (D_{opt}) (m^2/s)	**Hydrogen uptake** ($C_{0,\text{opt}}$) (ppm)
$1.25 \cdot 10^3$	$4.23 \cdot 10^{-10}$	0.045

The estimated apparent diffusion coefficient and hydrogen uptake are in good agreement with those obtained after electrochemical charging. Although the hydrogen uptake tests were performed using the -1 V vs SCE condition, the close correspondence between the gaseous and electrochemical results confirms that both charging environments can be reliably correlated. This implies that, under appropriate charging conditions (such as those discussed above), equivalent hydrogen concentrations and diffusion parameters can be determined for both gaseous and electrochemical hydrogen. Consequently, hydrogen introduced through either method is expected to modify the mechanical behaviour of the material in a similar manner, as further examined in the subsequent chapters dedicated to fracture mechanics testing.

Chapter 6

Fracture behaviour of steel A under electrochemical charging and gas charging

This chapter presents a detailed characterisation of the mechanical behaviour of steel A under synergistic hydrogen charging via both electrochemical and gaseous methods. SE(B) samples were used for electrochemical charging within the electrochemical cell mounted on the tensile testing machine. In contrast, mechanical tests under gaseous hydrogen charging require an autoclave, which has limited internal space; therefore, the more compact C(T) geometry was employed. These autoclave tests were conducted at the laboratories of the University of Manchester. The results obtained using the different testing methods are subsequently presented, compared, and correlated.

6.1 SE(B) and electrochemical solution

6.1.1 Specimens geometry

The specimens were designed following the ASTM 1820 as shown in Figure 6.1.

"C-L" crack plane identification was used, as reported by ASTM E399. The crack propagated along a plane parallel to the longitudinal axis of the pipe, in order to simulate the longitudinal propagation of defects, which are considered the most critical

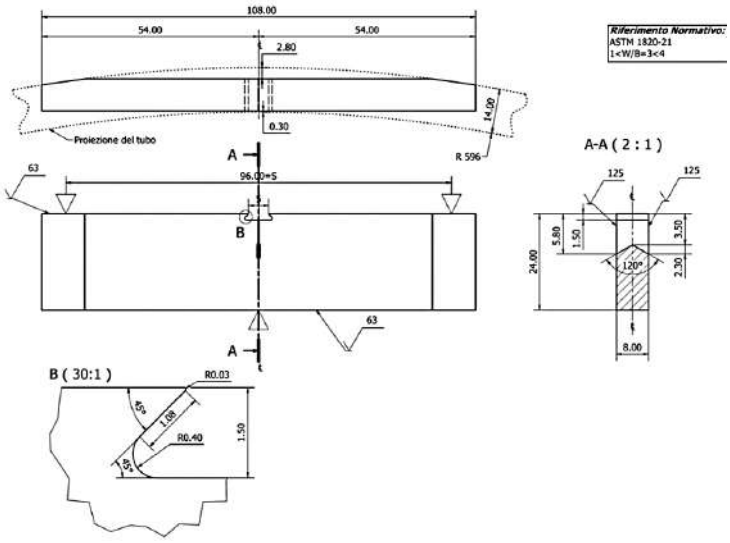

Figure 6.1: Geometry Single Edge Bend SE(B) specimens.

as they can lead to catastrophic rupture or full-thickness failure of the pipe wall [189, 190].

The specimen's dimensions were 8 mm thickness (B) and 24 mm wide (W), the W/B ratio equal to 3 was adopted. The support span (Sp) was 96 mm. The W/B ratio was adopted due to the constraints imposed by the pipe geometry. The specimens were produced by machining while the integrated knives for applying the double-cantilever Clip-In Displacement gage and chevron notch were produced via Electrical Discharge Machining (wire EDM). Both specimen sides were polished up to 1200 grit and degreased in acetone. The M4 thread was made in the thickness of the specimen (away from specimen's holders) for connecting the working pin during electrochemical charging.

6.2 Experimental lay out and procedure on SE(B)

6.2.1 Experimental lay-out

The three-point bend apparatus was produced to measure the fracture toughness of the SE(B) specimens in air and in situ cathodically hydrogen charging. Experimental

setup consists of a polymethyl methacrylate electrochemical cell positioned above the oil-hydraulic traction machine as shown in Figure 6.2.

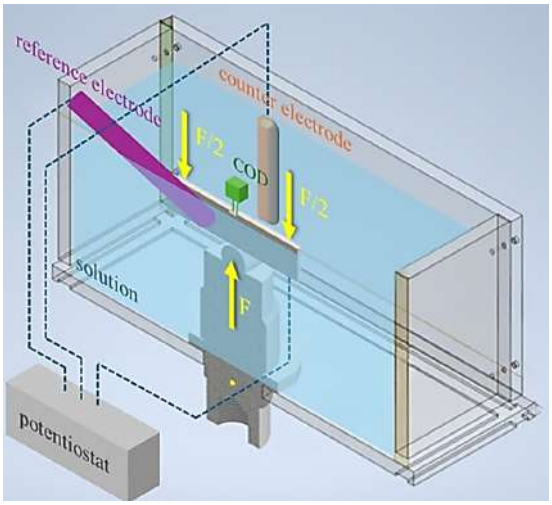

Figure 6.2: Experimental lay-out for fracture mechanic test with SE(B) geometry.

The specimen, acting as the working electrode, is oriented upside down compared to the conventional configuration. This arrangement allows for the attachment of the clip gauge (COD measure) while keeping the specimen fully submerged throughout the entire test, thereby ensuring the maintenance of cathodic polarisation on all surface of the sample. The cell was equipped with a calomel reference electrode positioned near to the crack surface and activated titanium counter electrode.

6.2.2 Experimental procedure SE(B)

The experimental procedure consists of double steps: fatigue pre-cracking procedure and mechanical fracture toughness test.

Precracking

To obtain the reproducibility of pre-cracking it was adopted decreasing ΔK approach imposing the parameter resumed in Table 6.1. It was imposed the notch depth as initial crack size, the final crack length equal to 10.8 mm (it was standard minimum value acceptable estimating as 0.45 W) and the final K value equal 14 $MPa \cdot \sqrt{m}$. These conditions guarantee the sufficient smaller residual load and little plastic radius in the

final crack tip. The pre-cracking configuration involves in load control configuration, producing by cyclically loading at ratio R=0.1 executed at 8 Hz in sinusoidal waveform to guarantee good machine feedback. The compliance was monitored. When the value of experimental compliance estimating as ratio of COD over force was reached, the target value was imposed the next load step.

Table 6.1: Pre-cracking parameter for SE(B) specimen.

Step	K	a_{final}	$a_{initial}$	f(a/W)	P_{max}	P_{min}	ΔP	CLL_{target}	r_p
[-]	$[MPa \cdot \sqrt{m}]$	[mm]	[mm]	[-]	[kN]	[kN]	[kN]	[mm/N]	[mm]
1	27.34	9.5	7.7	1.393076	4.626	0.46	4.164	4.06E-06	0.575
2	21.88	10	9.5	1.45617	3.541	0.35	3.187	4.48E-06	0.368
3	17.50	10.4	10	1.511065	2.730	0.27	2.457	4.87E-06	0.235
4	14.00	10.8	10.4	1.570464	2.101	0.21	1.891	5.31E-06	0.151

Fracture toughness tests

The mechanical fracture toughness tests involved a procedure directed toward evaluation of complete fracture toughness resistance curve using an elastic unloading procedure as described by ASTM 1820 (procedure 2). The tests were performed in displacement mode, with a displacement of 80 µm applied during the loading phase, followed by a 30 µm displacement during the unloading phase, as controlled by the clip gauge. This approach ensured continuous traction on the sample throughout both phases. Three displacement rates were analysed, both kept constant at $3 \cdot 10^{-5}$ mm/s (slow), $3 \cdot 10^{-4}$ mm/s (standard) and $3 \cdot 10^{-3}$ mm/s (fast) respectively. Multiple cycles were conducted for each test, with the test interruption determined based on the experimental curve obtained during each cycle. These mechanical parameters were applied on each scenario tested.

Four different test conditions were investigated. The first was an air test (AIR), in which the mechanical testing was conducted without any hydrogen supply (standard condition). The second involved environmental testing (ENV), the sample was submerged in solution and connected at the potentiostat. The sample was cathodically polarised at -1.05 V vs SCE during the mechanical loading/unloading cycles, thereby ensuring the presence of hydrogen throughout the mechanical test. The third condition (PRECH-AIR) assessed the effect of precharging: the sample was precharged at the same cathodic potential for 24 hours to allow hydrogen saturation, as confirmed in previously study on same material reported in [165], the sample was subsequently mechanically tested in air, without any further hydrogen supply during testing. The

final condition (PRECH–ENV) combined both approaches: the sample was precharged and mechanically tested while maintaining cathodic polarisation. Additionally, a high cathodic polarisation of 1.50 V vs SCE was investigated in the environmental (ENV) test.

At concluded the tests, all samples were opened in liquid nitrogen to identify the ending of mechanical test and measuring correctly the crack lengths on samples surface. The sample tested under cathodic protection was pickled in inhibited hydrochloric acid to remove the oxidize products without damaging the fracture surface.

6.3 Theory and calculations about SE(B)

6.3.1 Estimation of $J-\Delta a$ curve

The J-integral curve represents the strain energy release rate, thus the energy absorbed per unit fracture surface area during crack propagation. The energy J as a path-independent line integral that characterizes near-crack tip stresses and strains under elastic and/or elastoplastic material behaviours [191]. Therefore, from the integral of load/displacement experimental curve, it was possible to estimate the energy to promote a crack propagation J. The J-integral was estimated following the procedure outlined in ASTM E1820-21.

The calculation procedure involved estimating each cycle (loading, unloading, reloading) of load P_i, defined as the last point before unloading, and the crack length a_i, based on the unloading branch (characterised by linear elastic behaviour). The crack length was estimated by compliance CLL_i defined in standard ASTM 1820-21. The J_i for each cycle was defined as sum of elastic $J_{el(i)}$ and plastic contribution $J_{pl(i)}$ (Equation (6.1)).

$$J_{(i)} = J_{el(i)} + J_{pl(i)} \tag{6.1}$$

Defining the elastic component $J_{el(i)}$ as function of Poisson's and Young modules (ν, E) and Stress Intensity Factor K_i in elastic field follows

$$J_{el(i)} = \frac{(K_i)^2 \cdot \left(1-\nu^2\right)}{E} \tag{6.2}$$

and plastic component as follows

$$J_{pl(i)} = \left[J_{pl(i-1)} + \left(\frac{\eta_{pl(i-1)}}{b_{i-1}}\right) \cdot \frac{A_{pl(i)} - A_{pl(i-1)}}{B_N}\right] \cdot \left[1 - \gamma_{i-1} \cdot \left(\frac{a_i \cdot a_{i-1}}{b_{i-1}}\right)\right] \tag{6.3}$$

where $A_{pl(i)}$ was defined as the increment of plastic area under the chosen force versus plastic displacement record between lines of constant plastic displacement between two cycles. Thus considered the increment of energy due to plastic deformation.

From the intersection of the $J-\Delta a$ curve with the construction lines prescribed by the standard, a graphical estimate can be made of the energy value associated with the initial crack initiation, referred to as J_Q. By the definition of J_Q, it was possible to define the equivalent Stress intensity factor in elastic-plastic field as Equation (6.4) in accordance with ASTM 1820-21.

$$K_{J_{Ic}} = \sqrt{E' J_{Ic}} = \sqrt{\frac{E}{1-\nu^2} \cdot J_{Ic}} \tag{6.4}$$

6.3.2 Crack growth rate

In the SE(B) specimens, crack growth rate estimation was based on clip-gauge measurements of crack opening displacement (COD) using the ASTM E1820 unloading compliance method; thus, evaluation of the effective crack opening time was required. Proper propagation occurs only when there is a traction strain field at the crack tip. Therefore, it is necessary to determine the net crack opening time, subtracting from the total opening phase per cycle (Δv_{load}) the phase of unloading periods Δv_{unload} (where the crack can not to propagate). The crack opening time is thus calculated using Equation (6.5).

$$\Delta t_{crack\ opening} = t_{i-1} + \frac{\Delta v_{load} - \Delta v_{unload}}{displacement\ rate} \tag{6.5}$$

The average crack growth rate $\dot{a}$ is evaluated for each cycle as the crack extension (Δa) per cycle divided by the time required to progress from one cycle to the next one $\Delta t_{crack\ opening}$ (Equation (6.6)).

$$\frac{da}{dt} = \dot{a} = \frac{\Delta a}{\Delta t_{crack\ opening}} \tag{6.6}$$

6.3.3 Estimation of CTOD, CTOA and crack tip strain rate on SE(B) geometry

CTOD (δ)

The Crack Tip Opening Displacement (CTOD) is the distance between the opposite faces at the crack tip, measured at the 90° intercept position [192, 193]. It is commonly

determined at the point where the two 45° lines originating from the crack tip intersect the crack faces (Figure 6.3). CTOD expresses the plasticity at the crack tip and is more intuitively defined compared with parameters such as the J-integral.

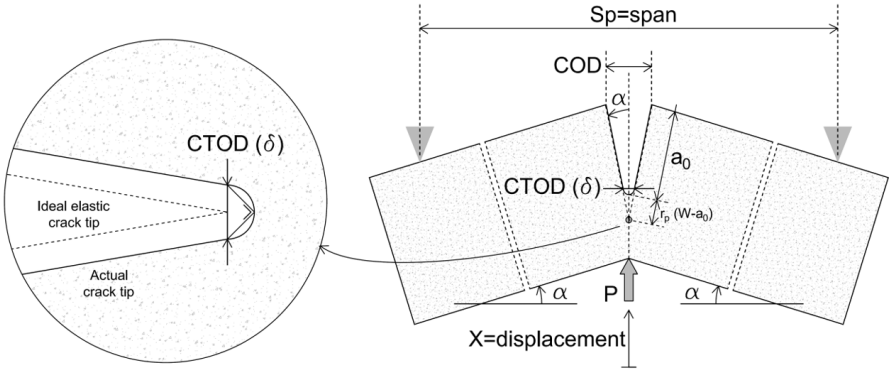

Figure 6.3: CTOD construction and geometrical relations.

Following the standard ASTM 1820-21, the CTOD can be estimated by the J integral for each cycle Equation (6.7)

$$CTOD(P_i) = \frac{J(P_i)}{m \cdot \left(\frac{\sigma_{ys}+\sigma_{uts}}{2}\right)} \tag{6.7}$$

Where m_i is defined as a polynomial function of a/W depending on the specimen geometry. The σ_{uts} and σ_{ys} are ultimate tensile strength and the strain respectively.

Assuming a rigid rotation α of the two arms of the SEN(B) specimen, and based on simple geometrical considerations from Figure 6.3, the strain-rate conditions at the crack tip can be estimated by assuming Equation (6.8):

$$\dot{\varepsilon}_{(\delta)} = \frac{d\varepsilon}{dt} \sim \frac{dCTOD}{dt} \tag{6.8}$$

Defining the CTOD(i) for each cycle as a function of the time required to progress from one cycle to the next one.

CTOA (2γ)

The Crack Tip Opening Angle (CTOA or 2γ) is the angle formed between the two crack surfaces, measured at the crack tip at the moment before the propagation (Figure 6.4). It is possible to correlate easily with the CTOD via geometric relation in Equation (6.9).

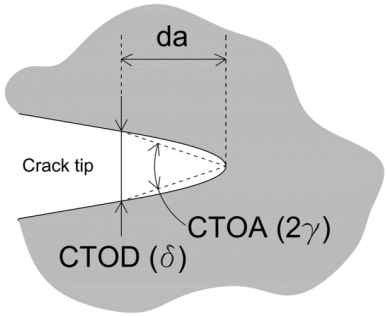

Figure 6.4: Scheme of CTOA at the crack tip.

$$\tan\left(\frac{\text{CTOA}}{2}\right) = tan(\gamma) = \frac{d\delta}{2 \cdot da} \approx \frac{\Delta\text{CTOD}}{2 \cdot \Delta a} \tag{6.9}$$

Hence, the CTOA can be obtained by rearranging the Equations (6.9) and (6.10).

$$\text{CTOA} = 2\arctan\left(\frac{\Delta\text{CTOD}}{2 \cdot \Delta a}\right) \tag{6.10}$$

Based on the concept of a similar stress field, it can be demonstrated [194] that the CTOA remains constant during crack propagation and assumes the same value for two geometrically similar specimens. An "equivalent" CTOA can also be defined from the average profile of a propagating defect, as proposed by Venzi[194, 195]. Thus, is possible to define a CTOA relation by the geometry of sample. According to Venzi's approach, the CTOA can be expressed as:

$$\text{CTOA} = 2\arctan\left(\frac{r_p \alpha_p}{-\ln\left[\frac{W-a}{W-a_0} \cdot \frac{1}{(cos(\alpha_p))^{r_p}}\right]}\right) \tag{6.11}$$

where the $\alpha_p$is the plastic geometrical rotation angle, a is crack length and r_p is the constant plastic radius equal to 0.45. The α_p represent the plastic component of the total rotation angle responsible for crack propagation. It is obtained by subtracting the initial specimen position (first cycle of the test) from the rotation angle of cycle i:

$$\alpha_p = \alpha(P_1) - \alpha(P_i) \tag{6.12}$$

Defining the rotation angle at cycle-i $\theta(P_i)$ as:

$$\alpha = \arctan\left(\frac{2X}{Sp}\right) \tag{6.13}$$

where X is the vertical crosshead displacement and Sp is the specimen span (as illustrated in Figure 6.3).

This relation holds for all specimen geometries and thicknesses, provided that CTOD is properly calculated. Comparing Equation (6.10) and Equation (6.11) for SE(B) specimens yields similar behaviour and consistent values of the stable propagation CTOA. The calculation of deformation rate is therefore independent of the selected CTOA estimation method. This allows demonstrating that the geometrical and energetic aspects of ductile crack propagation, as experimentally verified, are closely correlated.

However, the strain field around the defect can therefore be generalised according to Equation (6.14). Within a finite region surrounding the crack tip (and containing the crack tip point), for two specimens of different sizes (1) and (2), the following relationship holds:

$$\varepsilon_{ij}^{(1)}(x_1, x_2) = \varepsilon_{ij}^{(2)}(K_{12}x_1, K_{12}x_2) \tag{6.14}$$

where $K_{12}$is a scaling factor that does not depend on position of $x_1$or x_2. Therefore, the stress and strain fields of one specimen can be reduced to those of the other through this scaling relationship.

As for the lateral necking contribution on the CTOA estimation, it can generally be neglected. In fact, the necking process is driven by the global deformation field, since necking is a localised phenomenon contained within the broader region affected by global deformation [194]. Therefore, the increase in crack opening due to necking does not depend on the ligament size of the specimen or on any point of the load-displacement curve. This is also implied by the fact that the necking phenomenon is governed by the global deformation field, for which the conditions at the crack tip remain unchanged, since the CTOA associated with global deformation is constant. The energy involved in the crack propagation process is numerically determined by the global deformation field.

In this case, it is also possible to estimate a strain rate derived from the CTOA. It has been shown that the strain rate is approximately equal to the crack tip opening rate in Equation (6.8). By neglecting necking effects, the CTOA can be geometrically defined as the angle subtended by the same CTOD Equation (6.9). Hence, the strain rate can be written as:

$$\dot{\varepsilon}_{(\gamma)} \approx \frac{d(\delta)}{dt} = 2 \cdot \left[\frac{d}{dt} \left(da \cdot \tan(\gamma) \right) \right] = 2 \cdot \left[\dot{a} \cdot \tan(\gamma) + \frac{d}{dt} \left(\tan(\gamma) \right) \cdot \Delta a \right] \qquad (6.15)$$

where $\dot{a}$ is the crack growth rate, $\Delta a$is the crack extension, and $\frac{d}{dt}[\tan(\gamma)]$ represents the time variation of the tangent of the crack tip semi-angle, evaluated numerically from the slope of the plot of the tangent angle versus time.

6.4 Results and discussion SE(B)

6.4.1 Experimental results

The results of the mechanical tests are shown in Figure 6.5 for the slow (a), standard (b) and fast (c) displacement rates.

The maximum load measured in each test is affected by the pre-cracking length, which alters the available ligament for fracture during the test. Nevertheless, the results show good reproducibility. To confirm this, the pre-crack length was measured after opening the samples in liquid nitrogen.

In the initial branch, the curves exhibit a similar trend and are largely overlapping in all cases; however, a clear difference in behaviour emerges after the maximum load is reached. Considering this part, two distinct groups of curves can be identified: AIR, PRECH-AIR and ENV, PRECH-ENV (for different polarisation values). In AIR and PRECH-AIR tests, the load–displacement curves remained relatively constant and flat. In contrast, for the ENV and PRECH-ENV curves, the load drops after reaching the maximum load in monotonic and controlled way. This behaviour is also observed when the displacement rate is increased, although to a lesser extent Figure 6.5-b), and it becomes negligible at higher displacement rates (Figure 6.5-c). In any case, the following analysis will focus on the behaviour of the two groups of curves: AIR/PRECH-AIR and ENV/PRECH-ENV.

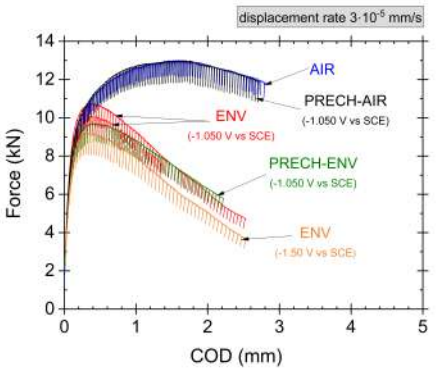

(a) Experimental curves at test rate $3 \cdot 10^{-5}$ mm/s (slow).

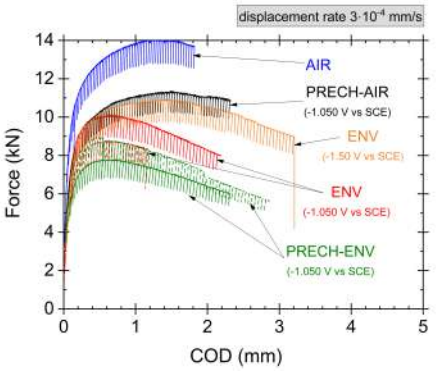

(b) Experimental curves at test rate $3 \cdot 10^{-4}$ mm/s (standard).

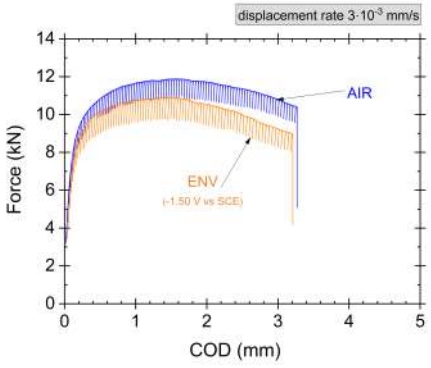

(c) Experimental curves at test rate $3 \cdot 10^{-3}$ mm/s (fast).

Figure 6.5: Experimental results of tests conducted in air, environment (at -1.05 and -1.50 V vs. SCE), precharging–air (at -1.050 V vs. SCE), and precharging–environment (both at -1.050 V vs. SCE) for all test rates.

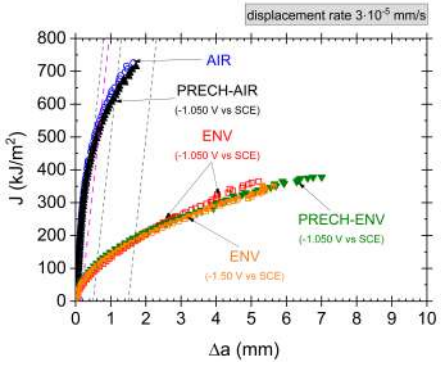

(a) J-integral curves at test rate $3 \cdot 10^{-5}$ mm/s (slow).

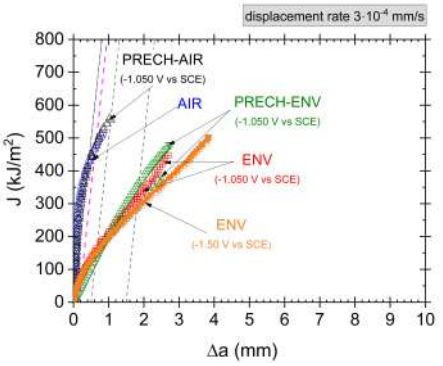

(b) J-integral curves at test rate $3 \cdot 10^{-4}$ mm/s (standard).

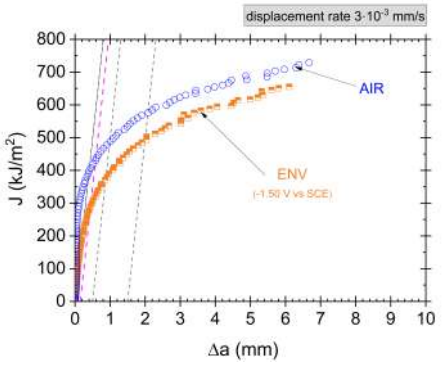

(c) J-integral curves at test rate $3 \cdot 10^{-3}$ mm/s (fast).

Figure 6.6: J-integral curves conducted in air, environment (at -1.05 and -1.50 V vs. SCE), precharging–air (at -1.050 V vs. SCE), and precharging–environment (both at -1.050 V vs. SCE) for all test rates.

6.4.2 J curves

Using the procedure described in Section 6.3.1 according with ASTM E1820 and implemented in a MATLAB code, it was possible to estimate the J-Δa curves for each test scenario presented in Figure 6.6 (a), (b), and (c) from the experimental data.

In this case as well, a clear difference can be identified between the AIR/PRECH-AIR and ENV/PRECH-ENV conditions. At the slow displacement rate of $3 \cdot 10^{-5}$ mm/s (Figure 6.6-a) considering the AIR and PRECH-AIR tests, the J curves were considerably higher, indicating that a greater amount of external work (input energy) was required to promote crack growth. In contrast, the tests conducted under cathodic

polarisation (both with and without precharging) displayed relatively flat J-Δa curves, suggesting easier crack propagation. This behaviour is consistent with the known effect of diffusible hydrogen, which compromises the plastic deformation mechanisms at the crack tip. Specifically, hydrogen reduces the material's ability to absorb energy through plastic deformation of the metal lattice in the crack-tip region [196–198]. Furthermore, the value of polarization has no significant effect, as cathodic charging at -1.050 V vs SCE results in the same behaviour as at -1.50 V vs SCE.

When similar tests were conducted at a displacement rate an order of magnitude higher ($3 \cdot 10^{-4}$), the differences between AIR, PRECH-AIR, and ENV, PRECH-ENV became less pronounced (Figure 6.6-b). This observation applies to both polarisation values used for the ENV and PRECH-ENV conditions. Nevertheless, the hydrogen effect in this case appears to be limited, likely because the higher test speed prevents sufficient interaction between hydrogen and the crack-tip plastic zone. Notably, the AIR and PRECH-AIR tests exhibited slightly lower J values compared with those obtained at the slower rate. Thus indicates that less energy was required to drive crack propagation even in the absence of hydrogen. This behaviour can be attributed to the influence of the increased displacement rate on the plasticity mechanisms at the crack tip, despite the unchanged specimen geometry. Consequently, more external work was required to promote crack growth compared with the corresponding scenarios at the slower rate.

The same observation it is valid if increasing the displacement rate up to $3 \cdot 10^{-3}$ mm/s (Figure 6.6-c). In this case the difference between test conduct in AIR and under the higher cathodic hydrogen charge (ENV) is almost negligible.

This behaviour is confirmed by the fractographic analysis shown in Figure 6.7.

The fracture surfaces of samples conducted at $3 \cdot 10^{-5}$ mm/s in AIR (Figure 6.7-a) and PRECH-AIR (Figure 6.7-b), exhibit similar surfaces characterised by dimples and extensive plastic deformation, indicating a ductile fracture mechanism. In contrast, the surfaces from the ENV (Figure 6.7-c) and PRECH-ENV (Figure 6.7-d) tests display a more brittle appearance. An increase in polarisation does not alter the effect of hydrogen on the surface morphology (Figure 6.7-e). Cleavage facets and separation cracks were observed. The latter are typically associated with laminated thick hot-rolled material subjected to hydrogen embrittlement. These separations are oriented normal to the crack propagation plane and parallel to lamination direction (ferrite/perlite layers).

The lack of hydrogen embrittlement in the PRECH-AIR condition, even under slow strain rate ($3 \cdot 10^{-5}$ mm/s) testing that would be expected to accentuate HE effects, is noteworthy. This behaviour, despite cathodic precharging to saturation, can

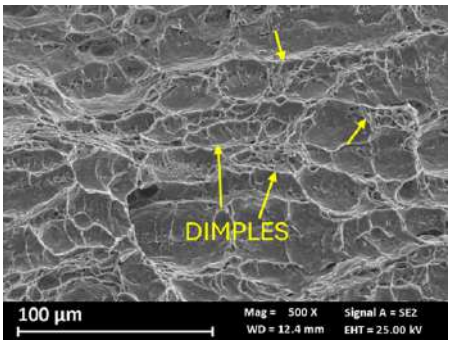

(a) Test in air without the hydrogen "AIR".

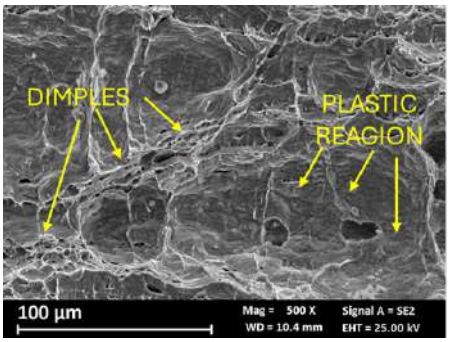

(b) Precharging (-1.050 V vs SCE) and mechanical tested in air "PRECH-AIR".

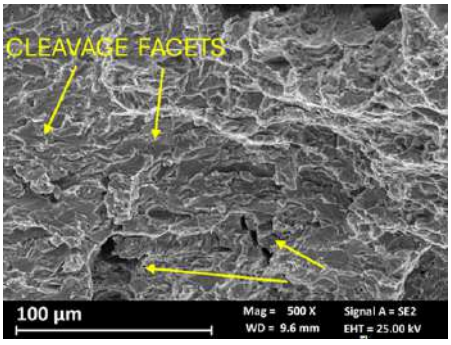

(c) Tested under cathodic polarisation (-1.050 V vs SCE) with hydrogen supply "ENV".

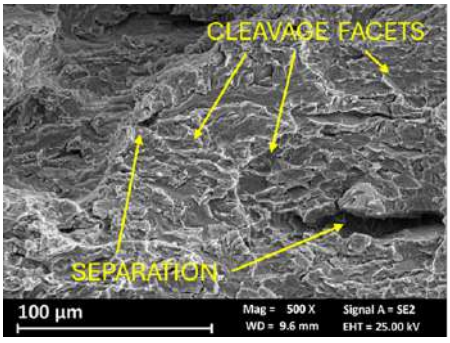

(d) Precharging and maintaining the cathodic polarisation (-1.050 V vs SCE) mechanical tested "PRECH-ENV".

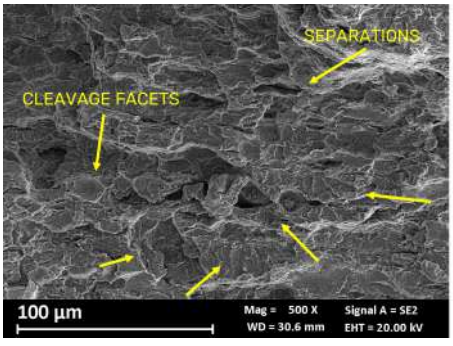

(e) Tested under cathodic polarisation at -1.5 V vs SCE with hydrogen supply "ENV".

Figure 6.7: Fractographic analysis of samples in different scenarios at test rate $3 \cdot 10^{-5}$ mm/s (slow).

be explained by the hydrogen uptake and diffusivity characteristics of the material. Under conditions of spontaneous desorption at room temperature and atmospheric pressure, diffusible hydrogen egress from the sample extremely rapidly. It has been demonstrated that, after only 7 minutes of spontaneous desorption, the concentration of diffusible hydrogen decreases to approximately 1/3 of the total hydrogen content measured [165] Section 5.4.1. In case of $3 \cdot 10^{-5}$ mm/s test rate the mechanical tests lasted for approximately 60 hours, basically all diffusible hydrogen was lost in the very early stages of testing. It is well known that diffusible hydrogen is primarily responsible for hydrogen embrittlement phenomena and crack propagation [20, 21, 137, 139]. Consequently, in the absence of a continuous hydrogen supply at the crack tip, plastic deformation was not limited by hydrogen causing predominance of plastic behaviour.

The fractografic analisis about tests conducted at higher displacement rates are shown in Figure 6.8.

For a displacement rate of $3 \cdot 10^{-4}$ mm/s (Figure 6.8-a), the fracture surfaces exhibit dimples, indicative of ductile behaviour. However, the differences between the surfaces obtained from tests conducted with and without hydrogen, even at -1.50 V vs SCE (Figure 6.8-b), remain relatively minor. The presence of cleavage facets is lower than in samples tested at a displacement rate one order of magnitude lower. Increasing the displacement rate, plastic deformation becomes the predominant mechanism. In this case, lateral contraction of the sample becomes significant and is not inhibited by the presence of hydrogen, as shown by the pronounced lateral contraction observed in Figure 6.9.

For tests at $3 \cdot 10^{-3}$ mm/s , the fracture surfaces are very similar regardless of hydrogen charging, displaying a ductile appearance with little evidence of cleavage, even when hydrogen was supplied during the test under high polarisation (Figure 6.8-d). At this elevated displacement rate, the mechanism is dominated by extensive plastic deformation, leading to pronounced lateral deformation and necking of the specimens (Figure 6.9), regardless of hydrogen presence. The effect of hydrogen remains extremely limited or negligible at this displacement rate, as shown in Figure 6.10 for the test performed at a fast displacement rate under cathodic polarisation at -1.5 V vs SCE.

Analysing the fractographic surface, a clear difference can be observed between the lateral side in contact with the external environment and the more internal region of the sample. This occurs because hydrogen ingress is much slower than the ductile tearing associated with mechanical deformation. As a result, the crack propagates before hydrogen can reach the crack tip and embrittle it. On the external side, some

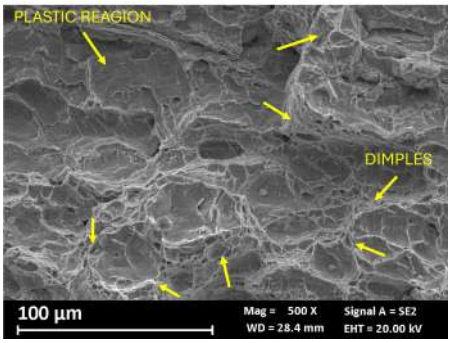

(a) Test "AIR" at $3 \cdot 10^{-4}$ mm/s.

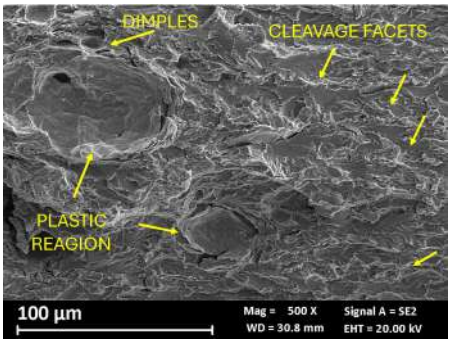

(b) Test "ENV" -1.50 V vs SCE at $3 \cdot 10^{-4}$ mm/s

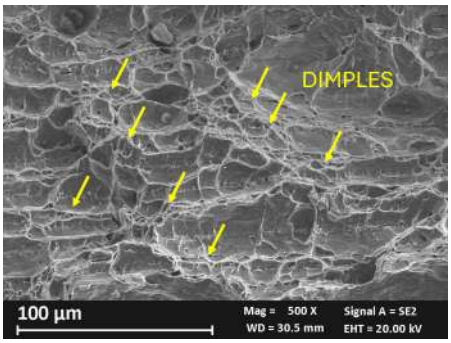

(c) Test "AIR" at $3 \cdot 10^{-3}$ mm/s.

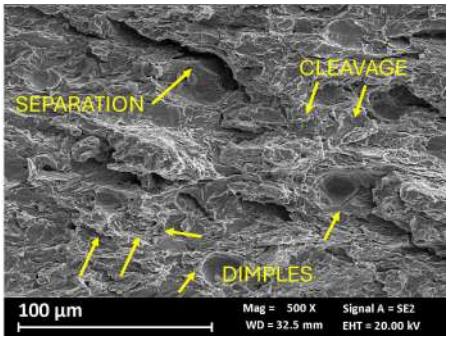

(d) Test "ENV" -1.50 V vs SCE at $3 \cdot 10^{-3}$ mm/s.

Figure 6.8: Fractographic analysis of samples tested at different displacement rates (standard and fast), both without hydrogen and under high cathodic polarisation investigated.

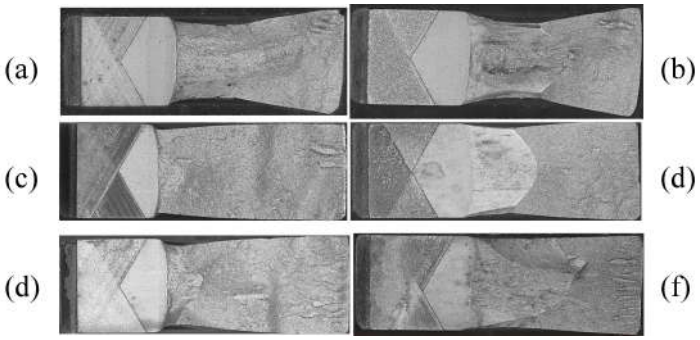

Figure 6.9: Lateral contraction of SE(B) under cathodic polarisation at different displacement rates. (a)$3 \cdot 10^{-3}$ mm/s AIR, (b)$3 \cdot 10^{-3}$ mm/s at -1.50 V vs SCE; (c)$3 \cdot 10^{-4}$ mm/s AIR, (d)$3 \cdot 10^{-4}$ mm/s at -1.50 V vs SCE; (e)$3 \cdot 10^{-5}$ mm/s AIR, (f)$3 \cdot 10^{-5}$ mm/s at -1.50 V vs SCE.

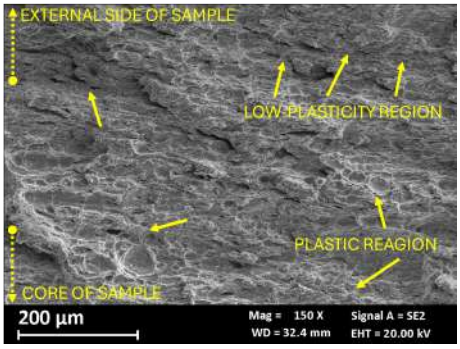

Figure 6.10: Fractographic surface at low magnification of the test performed at a fast displacement rate under polarisation at -1.50 V vs SCE. The external side and the more internal region of the sample can be seen.

low-ductility areas with quasi-cleavage features are visible, while moving towards the core of the sample these limited effects almost disappear, giving way to a markedly ductile fracture surface rich in dimples.

Nevertheless, for all displacement rates analysed, no difference in behaviour was observed on fracture surfaces between the two experimentally identified groups of curves: AIR/PRECH-AIR and ENV/PRECH-ENV. Thus, pre-charging does not appear to be a significant factor for establishing hydrogen embrittlement in this type of metal. Mechanical tests should be performed with *in situ* hydrogen charging (ENV curves) to ensure a continuous hydrogen supply throughout the test, thereby enabling a consistent assessment of hydrogen embrittlement mechanisms. In contrast, cathodic pre-charging followed by *ex situ* mechanical testing (PRECH-AIR curves) may not provide an accurate representation of hydrogen effects under service-relevant conditions.

Furthermore, to adequately analyse the effect of hydrogen on crack propagation, the displacement rate must also be considered. It is a crucial factor in evaluating hydrogen's influence on crack growth: slower testing rates accentuate the hydrogen effect, whereas higher rates tend to diminish it. At slower displacement rates, hydrogen has sufficient time to diffuse into the sample and can inhibit plastic deformation at the crack tip.

6.4.3 J_Q estimation and Hydrogen Embrittlement Ration

In accordance with the standard, the J_Q values for each test were estimated using the prescribed construction line method. Specifically, J_Q was determined as the intersection

point between the dashed construction line (magenta in Section 6.4.2) and the J-Δa curve. The J values at crack initiation are reported in Table 6.2 and summarised in Figure 6.11.

Table 6.2: Evaluation of J_Q and Hydrogen Embrittlement Ratio (HER) for different test conditions.

TEST CONDITION		Displacement rate SLOW ($3{\cdot}10^{-5}$ mm/s)		Displacement rate STANDARD ($3{\cdot}10^{-4}$ mm/s)		Displacement rate FAST ($3{\cdot}10^{-3}$ mm/s)	
		J_Q [kJ/m^2]	HER%	J_Q [kJ/m^2]	HER%	J_Q [kJ/m^2]	HER%
AIR		576	–	484.7	–	445.5	–
PRECH-AIR	Cathodic precharging and mechanical test in air without hydrogen supply	546.4	5%	492	0%	–	–
ENV (-1.50 V vs SCE)	Cathodic charging at -1.50 V vs SCE during the mechanical test (with hydrogen supply)	68.2	88%	91.5	81%	307.5	31%
ENV (-1.050 V vs SCE)	Cathodic charging at -1.050 V vs SCE during the mechanical test (with hydrogen supply)	76.1 59.6	87% 90%	98.9 92.0	80% 81%	–	–
PRECH-ENV	Cathodic precharging and mechanical test maintaining the cathodic polarisation at -1.050 V vs SCE	66.9	88.4%	90.5 100	81% 79%	–	–

Overall, the presence of hydrogen reduces the J_Q values in all cases. For the same scenarios, the lowest values were recorded under slow displacement rate conditions.

Hydrogen-assisted cracking can be quantified by comparing the results obtained in hydrogen and in air using the Hydrogen Embrittlement Ratio (HER%), as defined in Equation (6.16).

$$HER\% = \frac{J_Q(AIR) - J_Q(test\ condition)}{J_Q(AIR)} \cdot 100 \tag{6.16}$$

Under slow displacement rate conditions, the HER% is relatively negligible for the PRECH-AIR test, while it increases significantly, up to nearly 90%, for the ENV test (for both polarisation values). These values are comparable to those obtained for the PRECH-ENV test, confirming that precharging alone does not significantly contribute to embrittlement. This result further demonstrates that a continuous hydrogen supply during mechanical testing is required to observe hydrogen embrittlement effects.

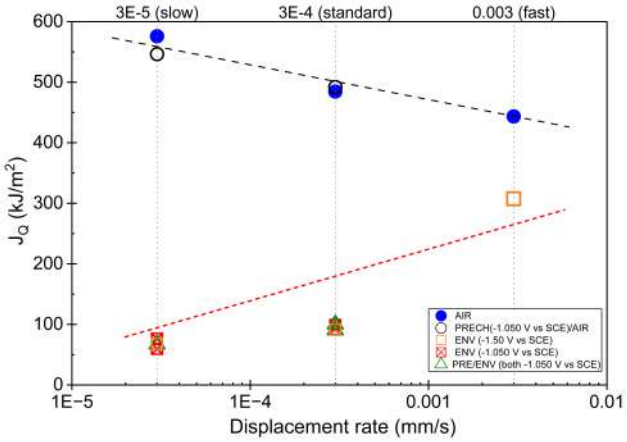

Figure 6.11: Comparison of J_Q values from tests conducted under different conditions, with and without hydrogen charging, and at various displacement rates.

Increasing the displacement rate reduces the influence of hydrogen embrittlement on the mechanical behaviour, even when high polarisation is applied as shown in Figure 6.11. In fact, at high displacement rates, the J_Q value is only reduced to 31% compared with the corresponding value in air. The effect of displacement rate also characterises the mechanical behaviour in air, where J_Q increases as the displacement rate decreases. This trend overlaps with the hydrogen-induced response, highlighting the critical role of strain rate in crack growth.

6.4.4 Velocity of crack propagation and strain rate

The test velocity is a crucial parameter influencing the rate of crack propagation under all conditions investigated, in accordance with the discussion in Section 6.3.2. Figure 6.12 shows the force versus testing time (left) and the crack growth versus testing time (right).

The correctness of the estimated final crack length (Δa) was confirmed by comparison with the experimentally measured value (marked with a cross on the graphs), obtained after opening the sample in liquid nitrogen. Apart from minor differences due to fitting and experimental uncertainties, the results are in good agreement.

As previously discussed, the crack propagation behaviour is comparable for the two conditions, AIR/PRECH-AIR and ENV/PRECH-ENV. In all cases, during the initial cycles the crack is affected by blunting, and no significant growth occurs. Crack

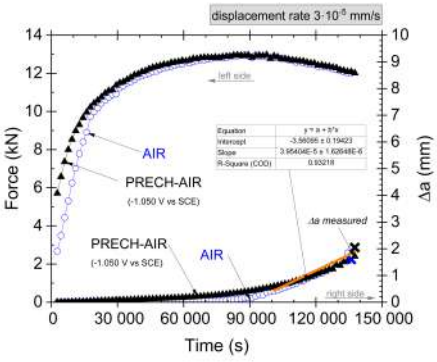

(a) AIR and PRECH-AIR at slow displacement rate.

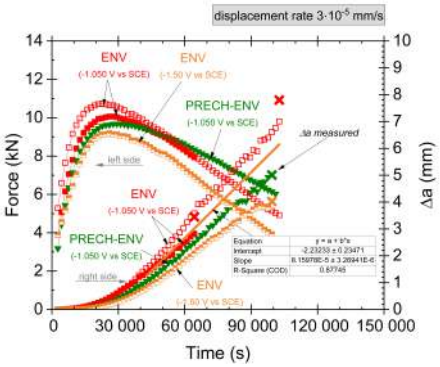

(b) ENV and PRECH-ENV at slow displacement rate.

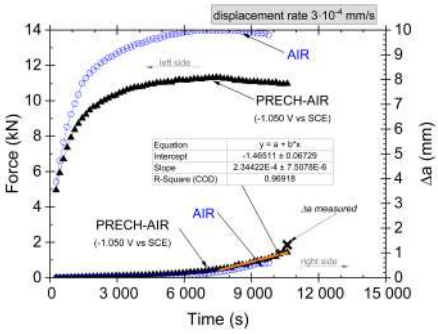

(c) Tests in AIR and PRECH-AIR at standard displacement rate.

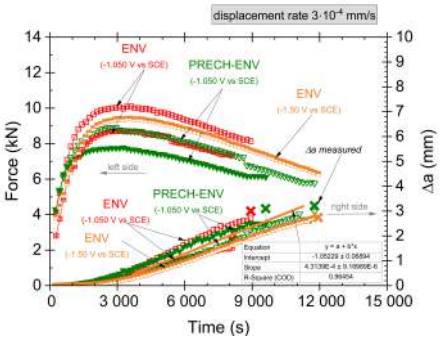

(d) ENV and PRECH-ENV at standard displacement rate.

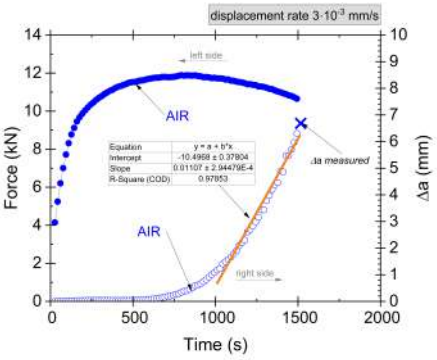

(e) AIR and PRECH-AIR at fast displacement rate.

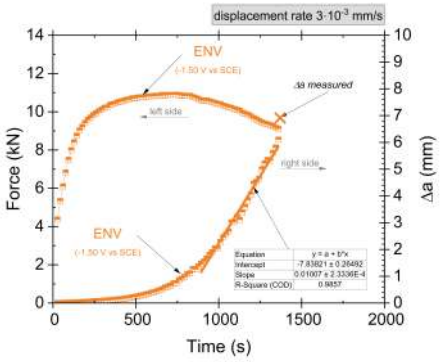

(f) ENV and PRECH-ENV at fast displacement rate.

Figure 6.12: Elaboration of load versus testing time (right) and crack growth versus testing time (left) under different test conditions. (a) and (b) slow displacement rate; (c) and (d) standard displacement rate; (e) and (f) fast displacement rate.

extension begins once the load reaches its maximum value, as also confirmed by Venzi [199]. In general, the slope (and thus the crack growth rate) increases with increasing displacement rate, even for the tests conducted in air, highlighting the influence of test velocity on the results. The crack growth behaviour is linear and monotonic. Therefore, a linear fit (indicated by the orange line in the graph) was used to estimate the slope, which represents the crack growth rate. For the slow displacement rate, the slope for AIR/PRECH-AIR ($4 \cdot 10^{-5}$ mm/s) is approximately half that of ENV/PRECH-ENV ($8 \cdot 10^{-5}$ mm/s). This difference decreases with increasing test velocity, becoming nearly identical ($1 \cdot 10^{-2}$ mm/s) under fast displacement rate conditions. These results indicate that, to clearly observe hydrogen embrittlement effects, it is essential to perform tests at slow displacement rates and under in situ hydrogen charging conditions.

Additionally, increasing the polarisation does not alter the crack growth process. In all cases, higher polarisation does not affect the crack growth behaviour: the slope of the curve remains comparable to that observed at lower polarisation. Any slight variations in the slope are likely attributable to test reproducibility, result dispersion and material inhomogeneity.

In the linear stage of crack propagation, the process remains stable, as indicated by the homogeneous fractographic analysis and the constant stress intensity factor (K_{JQ}), as shown in Figure 6.13.

The initial data points are influenced by a low propagation velocity due to the blunting effect at the crack tip. Crack propagation occurs at an approximately constant K_{JQ} value under the different conditions. As expected, at the same displacement rate, the crack velocity increases in the presence of hydrogen. This reduces the characteristic K_{JQ} value (in agreement with the estimated J_Q) and indicates more brittle behaviour. As the displacement rate increases, the difference between the tests performed with and without hydrogen becomes less pronounced, and at higher rates, the two curves tend to overlap, highlighting the importance of displacement rate in hydrogen-assisted cracking.

The accumulation of data points at the end of each branch indicates that the process is characterised by a specific crack growth rate and associated mechanical behaviour, defined by a constant K_{JQ}. The points accumulate at different heights, reflecting distinct characteristic crack growth rates under each condition investigated (displacement rate and hydrogen charging).

The propagation process is characterised by a specific and constant stress intensity factor, allowing the identification of a characteristic geometrical condition for crack

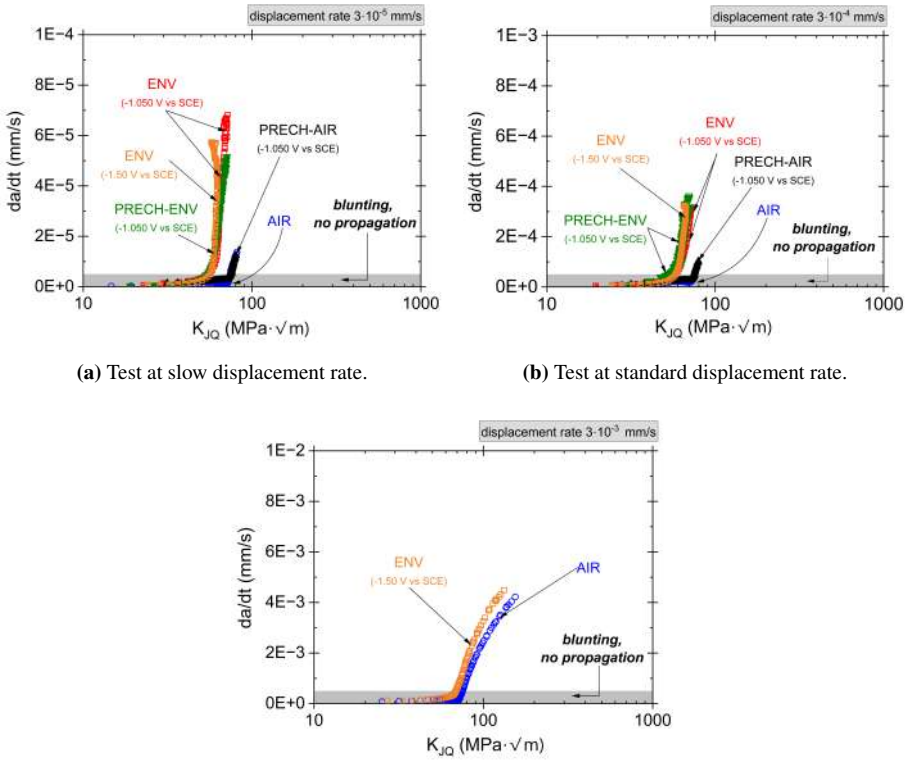

(a) Test at slow displacement rate.

(b) Test at standard displacement rate.

(c) Test at fast displacement rate.

Figure 6.13: Stress intensity factor as a function of crack growth rate under different displacement rates and hydrogen conditions.

growth. Figure 6.14 presents the Crack Tip Opening Displacement (CTOD) and Crack Tip Opening Angle (CTOA) as functions of crack extension (Δa).

In the present study, the CTOD is not constant during propagation, which is consistent with the relatively small specimen size and the resulting plane stress condition. Necking effects alter the local stress and strain fields, preventing propagation at a constant tip opening displacement. Nevertheless, the characteristic propagation angle obtained following Venzi's analysis remains consistent, as it is independent of necking [195, 199]. During propagation, the CTOA remains nearly constant as show in the graphs and hypothesised by [195, 200]. Initially, the angle increases due to elastic deformation and crack tip blunting, both associated with very small Δa values. As the crack grows, the angle decreases slightly and stabilises. However, achieving a fully constant angle is not always possible with this geometry.

In the slow displacement rate AIR test (without hydrogen), the ligament length is insufficient, and the test terminates prematurely due to the large CTOD reached, limited by the clip gauge at the same crack extension (Δa). Under identical conditions, hydrogen charging decreases the crack tip angle and produces smaller CTOD and COD values, enabling further crack growth and the attainment of the characteristic propagation angle. At higher displacement rates, however, a more complete curve with a stable propagation angle is achieved even without hydrogen, demonstrating that the local crack growth process is influenced by the global displacement rate.

In all cases, the effect of hydrogen embrittlement is evident under slow displacement rates and continuous hydrogen supply. The crack tip opening angle remains smaller than that of the uncharged condition at the same rate. As the displacement rate increases, this difference becomes negligible, confirming that hydrogen embrittlement effects are significant only under slow rate conditions. The correlation between CTOA and crack growth velocity further indicates that the local deformation results a crucial parameter to analyse the assisted hydrogen cracking.

By estimating the strain rate from CTOD or CTOA data, as reported in Section 6.3.3, the influence of hydrogen embrittlement on crack growth velocity becomes evident. Strain rates derived from these two parameters are reproducible and comparable (Figure 6.15-a-b), as they are correlated through geometric relationships, as discussed.

Hydrogen-assisted cracking occurs only at low strain rates, while at higher strain rates its effect is negligible. In particular, the influence of hydrogen becomes noticeable at approximately $1 \cdot 10^{-4}$ mm/s. Above this value, mechanical behaviour dominates the process, and the contribution of hydrogen-assisted mechanisms is minimal. At lower strain rates, the effect of hydrogen becomes significant: at the same strain rate, the

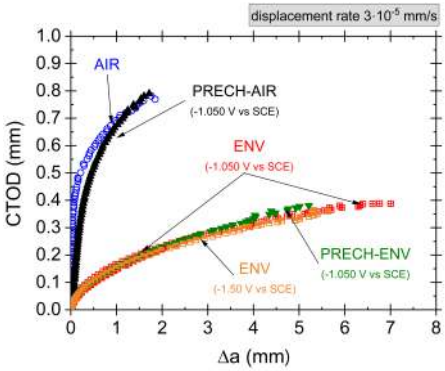

(a) CTOD at slow displacement rate.

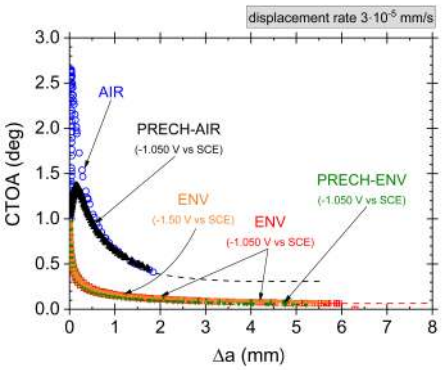

(b) CTOA at slow displacement rate.

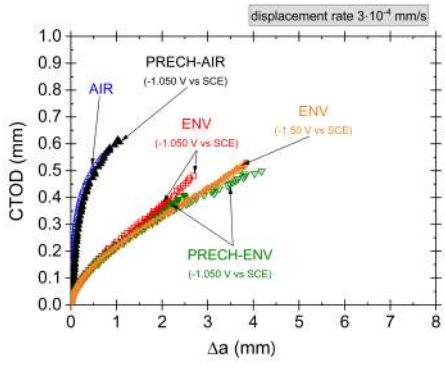

(c) CTOD at standard displacement rate.

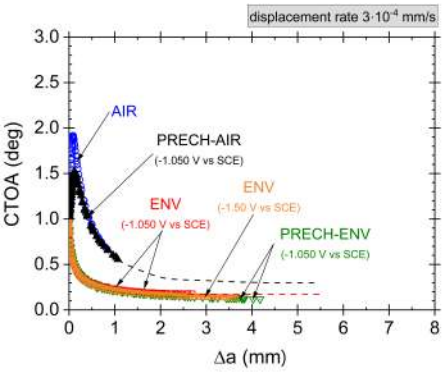

(d) CTOA at standard displacement rate.

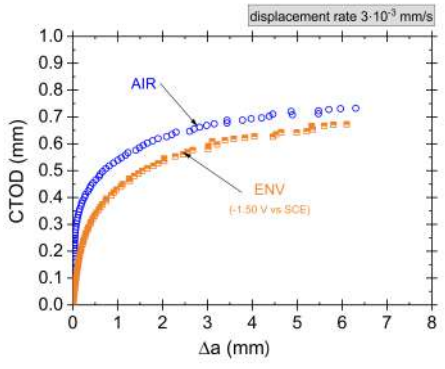

(e) CTOD at fast displacement rate.

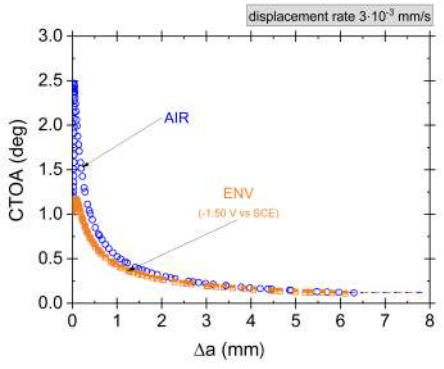

(f) CTOA at fast displacement rate.

Figure 6.14: Comparison of different conditions on Crack Tip Opening Displacement (CTOD) and Crack Tip Opening Angle (CTOA).

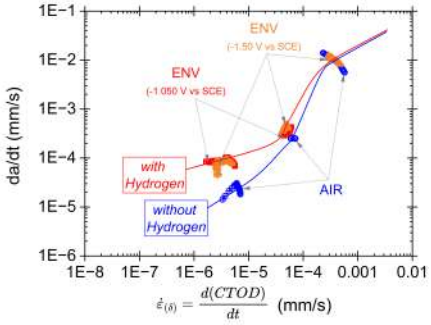

(a) Strain rate estimated from CTOD with and without hydrogen

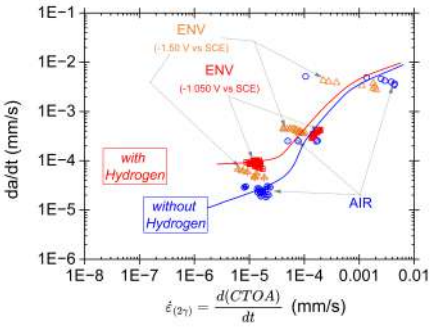

(b) Strain rate estimated from CTOA with and without hydrogen

Figure 6.15: Comparison of strain rate for different analysis methods with and without hydrogen on steel A.

crack propagation velocity can be up to four times higher under continuous hydrogen supply.

To evaluate the effect of hydrogen on crack propagation in synergy with mechanical stress, a parameter was introduced to quantify the susceptibility to hydrogen-assisted cracking (under hydrogen charging during testing). This parameter, referred to as the Hydrogen-Assisted Cracking Index (HACx), is defined in Equation (6.17):

$$HACx = 1 - \frac{\dot{a}_{AIR}}{\dot{a}_H} \tag{6.17}$$

where $\dot{a}_H$ and $\dot{a}_{AIR}$ represent the crack growth rates measured under hydrogen charging and in air, respectively. The HACx value ranges from 0 to 1: HACx = 0 indicates no susceptibility to hydrogen-assisted cracking, while HACx = 1 corresponds to full susceptibility, as illustrated in Figure 6.16.

Hydrogen-assisted cracking is strongly influenced by the synergistic interaction between hydrogen charging and slow strain rate. Under slow strain-rate conditions and continuous hydrogen supply (HACx→1), crack propagation is facilitated by hydrogen, which reduces the material's ability to deform plastically and consequently limits ductility. The crack-tip angle becomes smaller and more acute, promoting crack propagation at lower energy levels (low J_Q and K_{JQ}). When the strain rate increases (HACx→0), crack propagation is primarily governed by the displacement rate, and fracture initiates in a ductile tearing mode. The characteristic crack-propagation angle is larger compared with the critical tearing opening angle (CTOA) observed under hydrogen charging conditions. Therefore, in this case, hydrogen does not significantly

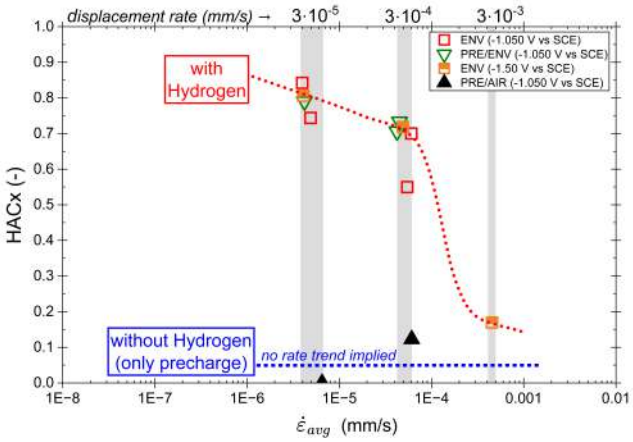

Figure 6.16: Hydrogen Assisted Cracking index.

restrict the plastic deformation available at the crack tip. Moreover, if hydrogen charging is not synergistic with mechanical loading, the HACx remains close to zero and is independent of the strain rate. Under such conditions (for instance, during pre-charging without concurrent mechanical loading), hydrogen does not effectively hinder the plasticity mechanisms at the crack tip.

6.5 C(T) material, geometry and experimental lay out

The material employed for the fabrication of the specimens is the same recently ferrite–pearlite steel extracted from the steel A previously described (Section 3.1). This material is identical to that used for the SE(B) specimens discussed earlier (Section 6.1.1), ensuring full consistency between the two testing methodologies. The use of specimens machined from the same pipe segment enables a comparison of the fracture and hydrogen-assisted cracking behaviour across different geometries, limiting the influence of material variability.

The specimens were manufactured according to ASTM E1820 in compact tension (C(T)) geometry, with fracture plane orientation "C–L" as defined in ASTM E399. The crack propagation direction is parallel to the longitudinal axis of the pipe. The specimen dimensions were 10 mm in thickness (B) and 25 mm in width (W), with a W/B ratio of 2.5 (Figure 6.17).

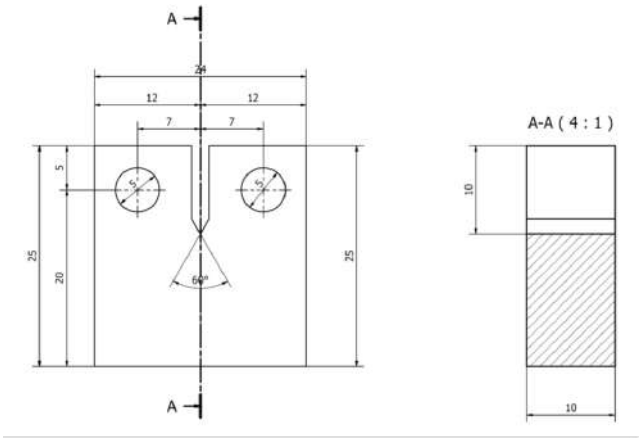

Figure 6.17: C(T) specimen geometry.

The crack length was monitored using a Direct Current Potential Drop (DCPD) system. Holes were drilled to allow electrical connection (Figure 6.18).

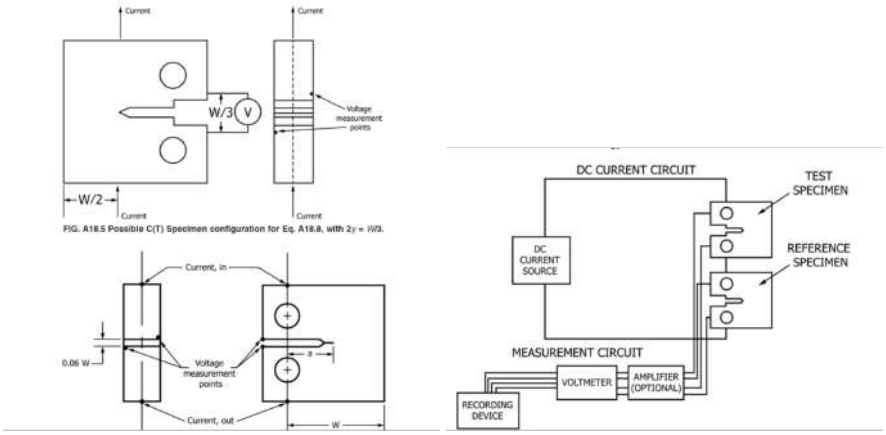

Figure 6.18: Position of wires for correct DCPD signal measurement.

A 0.8 mm silver wire carried the current, while a 0.5 mm wire measured the potential. The wires exited the autoclave (Figure 6.19-a-b) through a Conax feedthrough and were insulated with PTFE tubing (Figure 6.19-c). Two twin samples were placed in the autoclave: one tested mechanically, the other used as reference (Figure 6.19-d). The samples were connected in series electrically.

(a) Autoclave control area.

(b) Autoclave.

(c) Detail of the electrical connection for DCPD measurements in the autoclave.

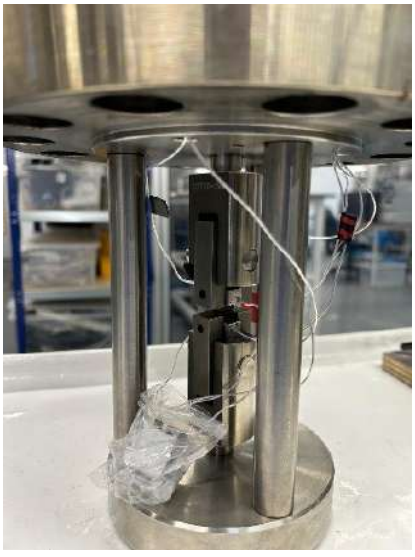

(d) Part to be inserted into the autoclave body, showing properly tested samples and a reference sample.

Figure 6.19: Experimental layout of autoclave with C(T) specimens in Manchester laboratories.

6.5.1 Experimental procedure for C(T) in autoclave

The experimental procedure consists of two phases: pre-cracking and fracture toughness testing.

Precracking

Pre-cracking was performed using a vibrophore. The minimum crack length required by the standard was 9 mm, and the maximum permitted was 14 mm. The process was divided into two stages reported in Table 6.3 to operating in decreasing ΔK as discussed in Ṫhe specimen was inspected every 100000 cycles and flipped to ensure homogeneous propagation.

Table 6.3: Pre-cracking parameters applied to the C(T) specimens.

# Stage	Static Force	Dynamic Force	Maximum Force	R	Frequency	Cycles
	[kN]	[kN]	[kN]		[Hz]	[-]
1	2.75	2.25	5.00	0.1	≈ 63	≈ 600000
2	1.65	1.35	3.00	0.1	≈ 58	≈ 300000

Fracture toughness testing

Elastic-plastic fracture mechanics tests were performed following ASTM E1820 (Procedure 1). The test was conducted in displacement control at rate of $3 \cdot 10^{-5}$ mm/s. A constant current of 1 A was applied for DCPD monitoring. At the end of each test, the specimens were opened in liquid nitrogen.

6.5.2 Mechanical fracture test procedure in autoclave

The mechanical fracture test procedure consisted of a sequence of controlled operations designed to ensure stable loading conditions and consistent environmental exposure throughout the experiment.

The first step involved the assembly of both the test specimen and the reference sample inside the autoclave, ensuring correct alignment and appropriate electrical isolation. This was followed by the calibration of the two LVDTs, which was necessary to obtain accurate displacement measurements during the test. Prior to applying the full mechanical load, a preload of approximately 2.5 kN was applied to the specimen. This operation minimised the compliance of the testing machine, the grips, and any

possible clearances within the loading train. In this way, the measured displacement primarily reflected the deformation of the specimen itself. The monotonic mechanical test commenced only once the applied load exceeded the maximum load used during the pre-cracking phase, thereby ensuring continuity in loading conditions.

The next step consisted of purging the system. For the test conducted under hydrogen pressure, the autoclave was purged with ten cycles of nitrogen at 5 bar, followed by five additional cycles with hydrogen at 5 bar. This procedure ensured that all gas lines were thoroughly cleaned and that any residual oxygen was eliminated before introducing hydrogen. After purging, the autoclave was pressurised with hydrogen to a final pressure of 150 bar, establishing the required environmental conditions for the fracture toughness test. For the test performed under inert nitrogen pressure, the procedure was the same: the system was purged with nitrogen and subsequently pressurised to 150 bar of nitrogen.

Finally, the slow strain rate (SSR) monotonic tensile test was carried out. The displacement rate was set to $3 \cdot 10^{-5}$ mm/s. The machine then began opening the specimen under controlled displacement. Typically, the maximum applied force reached approximately 15 kN, with a maximum relative displacement of about 2 mm. Throughout the entire duration of the test, the internal pressure was maintained constant.

6.6 Theory and calculations on C(T)

6.6.1 Explanation of calculation procedure

The data analysis was performed in accordance with the ASTM E1820 standard. In this context, crack growth was directly monitored using the Direct Current Potential Drop (DCPD) system, and all parameters were evaluated for each data point recorded during the test. Because the monotonic opening test induces continuous crack propagation, the stress field at the crack tip remains tensile throughout. Consequently, it was not necessary to define a specific time or point corresponding to a loading cycle, as the test does not involve cyclic loading but instead a purely monotonic opening. All calculations were carried out using dedicated MATLAB scripts developed specifically for this work Appendix B. The procedure consisted of a series of successive steps aimed at accurately defining the parameters required to identify the correct point at which crack growth initiates and to reliably associate the measured signal with the actual crack extension. This approach ensured that the estimated Δa was properly

aligned with the experimentally measured crack growth, providing consistency and accuracy in the evaluation of the fracture mechanics parameters.

Determination of V_0 and $V_{elastic}$

The parameters V_0 and $V_{elastic}$ represent the initiation of crack growth. A graph of applied load versus DCPD voltage was generated, following the example provided in Figure 6.20-a. A linear fit was performed on the portion of the curve showing a sharp initial increase. The critical value, referred to as V_{elastic}, corresponds to the point where the force versus DCPD curve starts to deviate from linearity, marking the upper limit of the linear region (Figure 6.20-b).

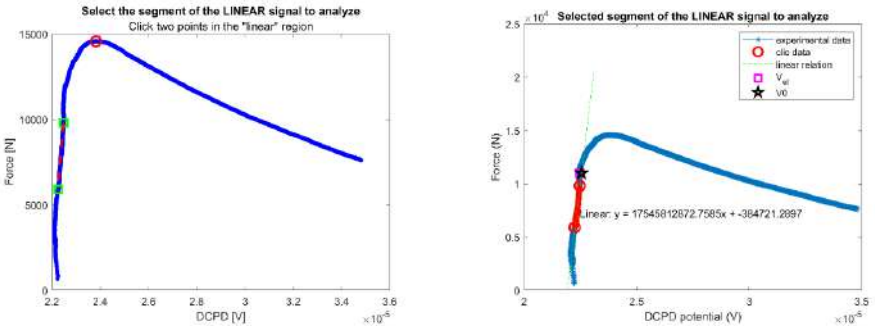

(a) V_0 identification. **(b)** V_{elastic} identification.

Figure 6.20: Identification of V_0 and V_{elastic}.

Blunting correction

The code adjusts the values in order to identify the optimal linear segment of the curve and to correctly associate the signal with the onset of crack propagation, taking into account the effect of crack tip blunting.

Adjusted crack length

The estimated crack length was validated against experimental measurements obtained using the polygonal gauge after specimen opening in liquid nitrogen. The objective is to recalibrate the signal by correlating it with a range of actual Δa values corresponding to the experimental data Figure 6.21.

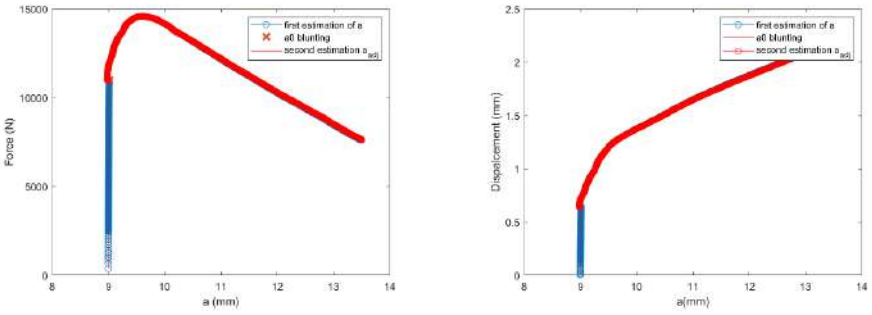

(a) First adjustment of crack length. **(b)** Second adjustment of crack length.

Figure 6.21: Validation of the estimated crack length against experimental measurements. The calibration aligns the measured signal with the corresponding range of actual Δa values.

Stress intensity factor K

The estimation of K and J integral it is made following the approach describe in the ASTM 1820 for the basic test method. The K was evaluated at each individual data point in accordance with Equation (6.18), yielding the results shown in Figure 6.22.

$$K_i = \frac{P_i}{\sqrt{BB_N W}} f\left(\frac{a_i}{W}\right) \tag{6.18}$$

with P is the load measured, $B = B_N$ is the thickness, W the width and $f(a_i/W)$ is a dimensionless geometry function that depends on both constants and the crack length-to-width ratio

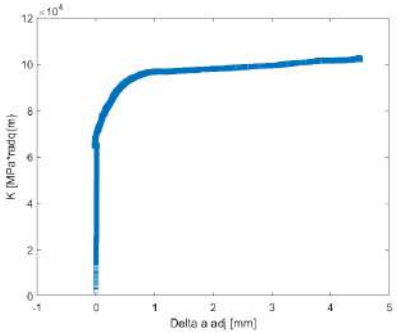

Figure 6.22: Evaluation of K_i via Matlab.

The J-integral curve is defined in the same way as in Equation (6.19), as the sum of the elastic and plastic contributions of the energy supplied to the specimen to promote crack growth.

$$J_{tot,i} = J_{el,i} + J_{pl,i} \tag{6.19}$$

Therefore, it is necessary to estimate the elastic ($J_{el,i}$, Equation (6.20)) and plastic ($J_{pl,i}$, Equation (6.21)) components as follows:

$$J_{el,i} = \frac{K_i^2(1-\nu^2)}{E} \tag{6.20}$$

$$J_{pl,i} = \left[J_{pl,i-1} + \left(\frac{\eta_{pl,i-1}}{b_{i-1}}\right)\frac{A_{pl,i} - A_{pl,i-1}}{B_N}\right]\left[1 - \gamma_{i-1}\left(\frac{a_i - a_{i-1}}{b_{i-1}}\right)\right] \tag{6.21}$$

In this case the quantity $J_{\mathrm{pl,i}}$ represents the total crack growth-corrected plastic J at point i. It is calculated in two steps: first, by incrementing the existing value $J_{\mathrm{pl,(i-1)}}$, and second, by adjusting the total accumulated value to account for the increment in crack growth. The difference $A_{\mathrm{pl,(i)}} - A_{\mathrm{pl,(i-1)}}$ corresponds to the increment of the plastic area under the force versus plastic load-line displacement curve between lines of constant displacement at points $i-1$ and i. The slope of the elastic line is determined from the load versus crosshead displacement data Figure 6.23.

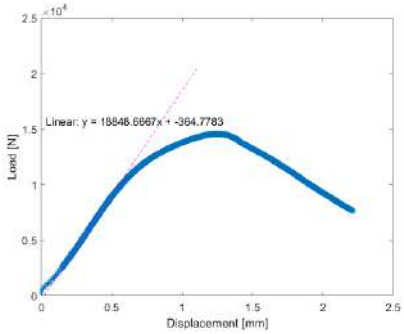

Figure 6.23: Evaluation of plastic area (A_{pl}).

6.6.2 CTOD, CTOA and crack growth rate for C(T)

The procedure is analogous to that used for SE(B) specimens Section 6.3.3. However, for C(T) specimens, the CTOD is calculated according to the standard law specific to their geometry, while the CTOA is estimated using the geometric relation from CTOD (Equation (6.10)), rather than the method proposed by Venzi, which was developed for SE(B) specimens and is not applicable to C(T) specimens.

Once the CTOD and CTOA values are determined, the crack propagation rate and the strain rate can be estimated in the same manner as for SE(B) specimens (Section 6.3.2), by evaluating the temporal variation of the relevant parameters.

6.7 Results and discussion C(T) in hydrogen gas

6.7.1 Experimental results

The experimental results are presented in Figure 6.24. The C(T) specimens exhibit behaviour similar to that of the SE(B) specimens. The initial portion of the curves, characterised predominantly by elastic deformation, overlaps for all tests. After reaching the maximum load, the curves begin to linear decrease (Figure 6.24-a). The difference in slope in this region is attributed to the presence of hydrogen gas during testing.

To apply the procedure for estimating crack growth, it is necessary to evaluate the response as a function of the DCPD signal (Figure 6.24-b). The DCPD signals start from different initial values, most likely due to variations in the initial conditions. The increase in electrical resistance and in the measured potential difference indicates crack growth.

Following the procedure outlined in Section 6.6, it is possible to estimate Δa and construct the corresponding J-Δa curves (Figure 6.25).

In this case as well, a clear difference is observed between tests performed with hydrogen charging and those carried out without it. The presence of hydrogen during mechanical testing reduces the material's ability to absorb energy, as the plastic deformation at the crack tip is diminished. Consequently, the curve is flatter and a lower amount of energy is required to achieve the same crack extension Δa. This effect is attributable to hydrogen; tests performed under nitrogen pressure (an inert gas without hydrogen) exclude any influence of the applied pressure, allowing the results to be directly compared as demonstrate by fracture analysis (Figure 6.26).

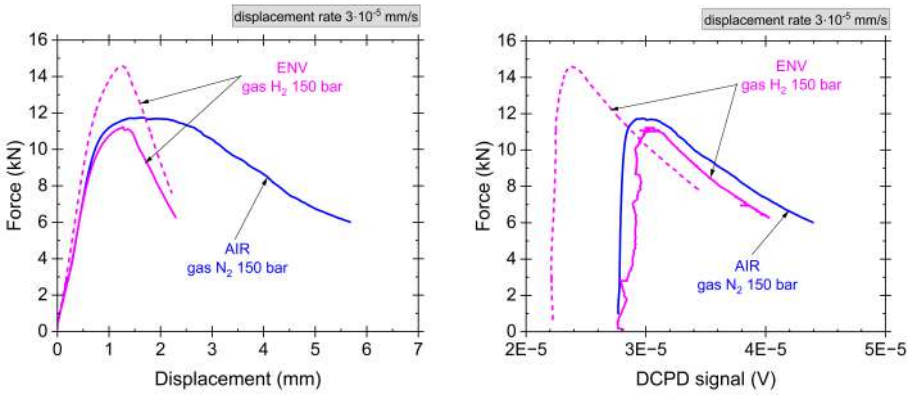

(a) Load–displacement response plotted against pull-rod displacement.

(b) Corresponding experimental data plotted against the DCPD signal.

Figure 6.24: Experimental results for the C(T) specimens tested at 150 bar in hydrogen (magenta curves) and nitrogen (blue curve).

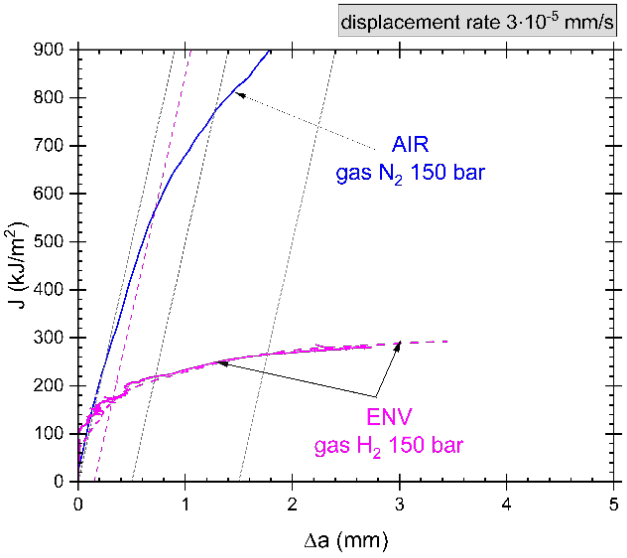

Figure 6.25: J-integral curves for the C(T) specimens tested with and without hydrogen charging (magenta and blue lines, respectively) at a displacement rate of $3 \cdot 10^{-5}$ mm/s.

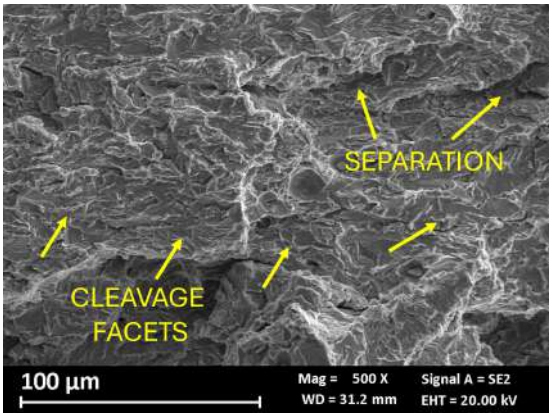

Figure 6.26: Fractographic analysis of the C(T) specimen surface from the test conducted under hydrogen gas charging at 150 bar, at a displacement rate of $3 \cdot 10^{-5}$ mm/s.

The fracture surface exhibits the typical features of hydrogen-assisted cracking. As also observed on the surface of the SE(B) specimens (Figure 6.7), quasi-cleavage facets are present, dimples are limited, and the fracture is of a mixed mode.

6.7.2 J_Q estimation, Hydrogen Embrittlement Ratio and comparison

Thus, the initiation energy J_Q associated with this process is in agreement with the previous results, as shown in Figure 6.27 and in reported in Table 6.4.

Table 6.4: Evaluation of J_Q and Hydrogen Embrittlement Ratio (HER) for the slow displacement rate ($3 \cdot 10^{-5}$ mm/s) in gaseous charging for steel A.

Test Condition	J_Q [kJ/m^2]	HER%
Nitrogen gas (150 bar)	565	–
Hydrogen gas (150 bar)	160 155	71.7 % 72.6 %

The J_Q value under nitrogen at 150 bar, tested at a displacement rate of $3 \cdot 10^{-5}$ mm/s, is comparable to that of SE(B) specimens tested in AIR. This indicates that the pressure of an inert gas does not affect the mechanical behaviour. In contrast, testing the C(T) specimens under the same displacement rate at 150 bar of hydrogen results

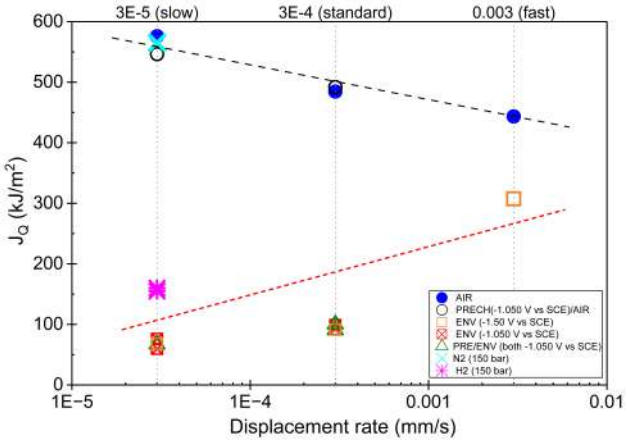

Figure 6.27: J_Q values for C(T) specimens in hydrogen gas compared with previously reported results for SE(B) specimens on the same material.

in a decrease of J_Q. Hydrogen induces a brittle phenomenon and reduces the crack initiation energy.

The hydrogen embrittlement ratio (HER%), estimated as reported in Equation (6.16), is 71.7% and 72.5% relative to nitrogen for the two tests performed. These values are comparable; however, they are slightly lower than those obtained for SE(B) specimens subjected to continuous cathodic charging at -1.050 V vs SCE (88-90%). This difference could be attributed to the calculation procedure. The standard suggests that estimating V_0 from the F-DCPD curve may be less conservative compared with method that used the load-line displacement measured with a clip gauge). Furthermore, differences in specimen geometry and test type (monotonic loading versus the compliance-based approach used for SE(B)) may introduce slight variations in the estimation of J_Q. Nevertheless, although the results exhibit a slight dispersion, they are in good agreement and consistently show the same trend, indicating that hydrogen promotes embrittlement regardless of whether the charging is electrochemical or gaseous.

6.7.3 Crack growth rate of C(T)

To analyse the crack growth behaviour of the C(T) specimens under gaseous charging, the graph in Figure 6.28 was constructed.

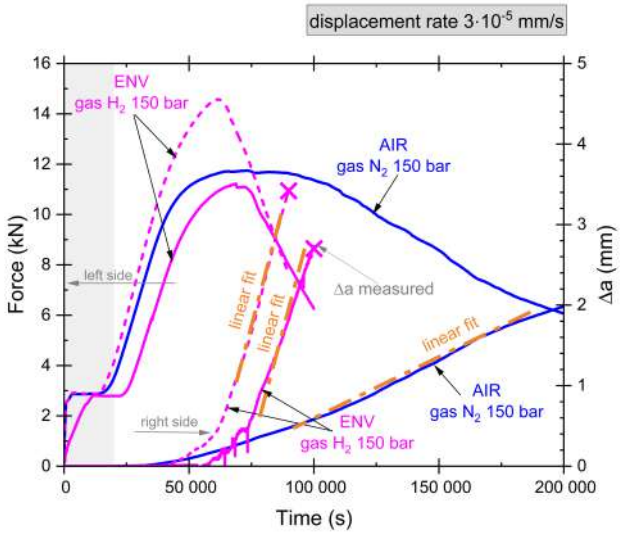

Figure 6.28: Elaboration of load versus testing time (left) and crack growth versus testing time (right), in hydrogen gas charging (magenta line) and nitrogen (blue line) both at 150 bar.

The initial branch of the load–displacement curves was affected by the compliance of the tensile testing machine (indicated in grey in the graph) and was therefore not considered during data processing. The applied load in this region was lower than that used during the final pre-cracking step, which induced a residual preload at the crack tip, thereby causing an error in the estimation of crack growth; consequently, this portion of the curve was disregarded.

As confirmation of the quality of the fitting procedure, the experimentally measured Δa values, obtained after opening the specimens in liquid nitrogen, are also reported on the graph. In all cases investigated, Δa begins to increase linearly after the maximum load is reached. The slope of this portion of the curve depends on the presence of hydrogen: with hydrogen, the slope is high, whereas under nitrogen the crack growth rate is slow.

The crack propagation process is stable and is therefore characterised by an approximately constant K_{JQ} value, as shown in Figure 6.29.

By estimating the crack growth rate as described in Section 6.3.2, it is evident that K_{JQ} remains nearly constant as the crack growth rate increases. This indicates that the process is governed by a stable mechanical behaviour. The value in the inert (nitrogen) condition is slightly higher than that obtained under hydrogen charging, as expected.

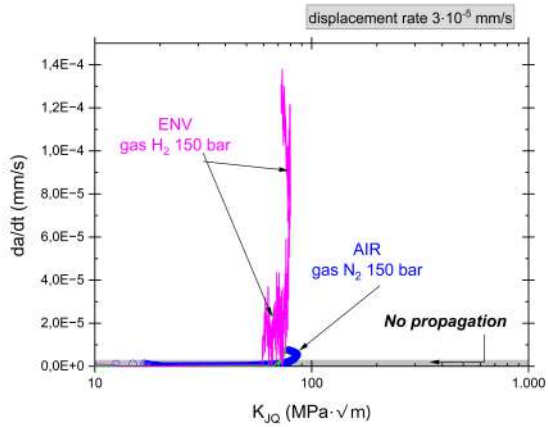

Figure 6.29: Stress Intensity Factor as a function of crack growth rate under hydrogen (magenta) and nitrogen (blue) pressure.

At the upper end of the vertical branch, the data points are densely clustered, showing that the crack propagates at an approximately constant velocity, demonstrated by the high concentration of points in this region, and therefore under an almost constant K_{JQ}.

Additionally, the propagation is characterised by a constant CTOA, as shown in Figure 6.30.

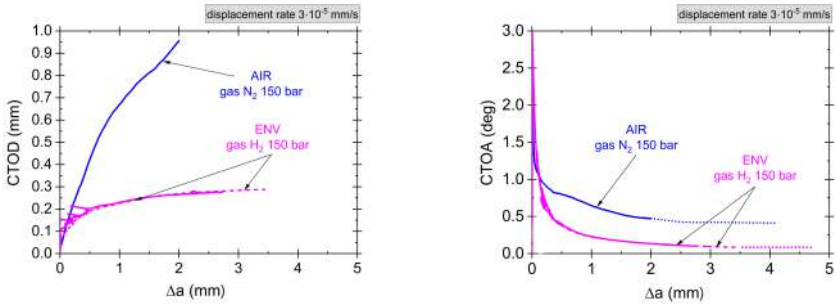

(a) Crack Tip Opening Displacement (CTOD) in hydrogen and nitrogen pressure.

(b) Crack Tip Opening Angle (CTOA) in hydrogen and nitrogen pressure.

Figure 6.30: Comparison of Crack Tip Opening Displacement (CTOD) and Crack Tip Opening Angle (CTOA) for C(T) specimens under hydrogen and nitrogen pressure.

In this case, the CTOD analysis (estimated according to the standard for the C(T) geometry) does not show a constant value for the nitrogen tests, whereas it remains reasonably constant under hydrogen charging. Nevertheless, the CTOA values were

estimated using the (Equation (6.10) by geometric method). They exhibit a stable propagation angle along the branch corresponding to the monotonically decreasing portion of the curve in Figure 6.28. Unfortunately, the signal from one test is slightly noisy, and therefore the CTOA estimation for small Δa in that case is not fully reliable. Nevertheless, the signal stabilises as propagation progresses and provides a reasonable and consistent measure during the stable phase. Indeed, the two tests performed in hydrogen (solid and dashed magenta lines) overlap closely.

Hydrogen reduces the deformation capacity at the crack tip, resulting in a lower propagation angle in its presence, as expected. This outcome is consistent with the fractographic analysis and aligns with the J_Q and K_{JQ} parameters discussed.

6.7.4 Comparison of strain rate and HACx

In this case as well, the strain rate was estimated in accordance with Section 6.6.2. Figure 6.31 reports the average strain rate along the stable crack growth region as a function of crack extension.

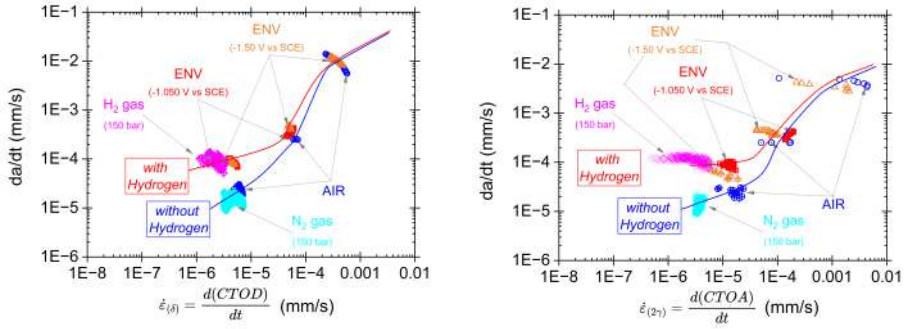

(a) Strain rate estimated by CTOD versus crack growth rate.

(b) Strain rate estimated by CTOA versus crack growth rate.

Figure 6.31: Strain rate estimated by CTOD (a) and CTOA (b) versus crack growth rate.

The tests performed on the C(T) specimens overlap well with the SE(B) results. The test carried out at a slow strain rate under 150 bar of nitrogen shows a low crack growth rate, whereas under 150 bar of hydrogen the crack growth rate is much higher at the same strain rate. These results are consistent with those obtained on SE(B) specimens and overlap with the interpretation line derived from the SE(B) tests.

Hydrogen supplied either as gaseous hydrogen or by electrochemical charging, provided that the appropriate equivalence is applied based on Sieverts's law Equa-

tion (1.13), produces comparable results. Combining CTOA and strain-rate analysis enables a meaningful comparison between the different specimen geometries and the different hydrogen charging methods as confirming by HACx estimate for these test (Figure 6.32).

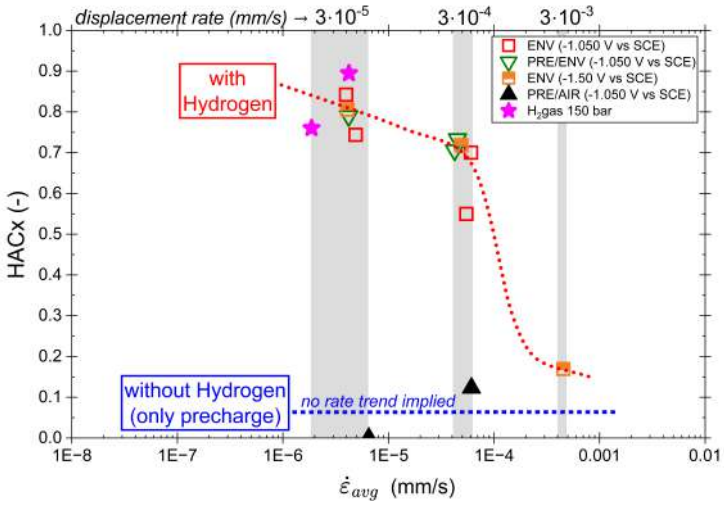

Figure 6.32: Hydrogen Assisted Cracking (HAC) index for C(T) specimens under gaseous hydrogen charging, compared with SE(B) specimens under electrochemical charging.

Chapter 7

Further assessment of fracture behaviour of steel B under electrochemical charging

In this chapter, the results of elastic–plastic fracture mechanics tests for steel B carried out under electrochemical hydrogen charging are presented. These tests were performed on SE(B) specimens machined from the steel B described in Chapter 3. The experimental methodology and testing apparatus are the same as those employed for the fracture mechanics tests on SE(B) specimens of steel A in Section 6.2.1 and Section 6.2.2. Likewise, the theoretical approach and calculation procedures adopted here are identical to those applied to SE(B) specimens of steel A, as detailed in Section 6.3. The following sections present the experimental results, which are discussed and compared with those previously obtained from SE(B) specimens of steel A.

7.1 Results and discussion

7.1.1 Experimental results

Figure 7.1 shows the experimental results obtained for SE(B) specimens machined from the steel B and tested in air (AIR), under continuous cathodic polarisation during the entire mechanical test (ENV), and under the same conditions but with an additional 24 h pre-charging at the same potential (PRECH-ENV).

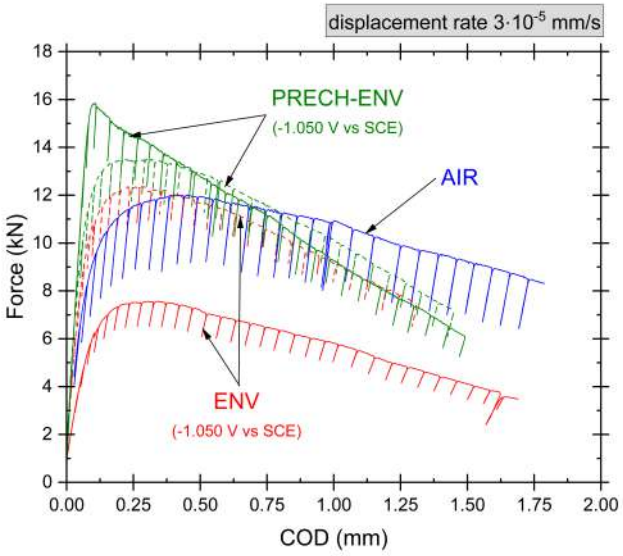

Figure 7.1: Experimental results of tests conducted in air, environment, precharging-environment at $3 \cdot 10^{-5}$ mm/s.

In all cases investigated, the initial portion of the curves, dominated by elastic behaviour, is nearly identical for all conditions. After reaching the maximum load, the curves exhibit a monotonic decrease characterised by a similar slope. As previously observed for the steel A, no significant differences arise between the ENV and PRECH-ENV conditions.

The curves are not perfectly superimposed because, for this material, the pre-cracking procedure was particularly difficult to control. Consequently, the reproducibility of the crack length (which strongly influences the mechanical response in terms of maximum load) is reduced. However, this does not compromise the stability nor the reproducibility of the analysis in terms of crack-growth energy.

The differences between AIR and hydrogen-charged tests are more limited in this material, even though the displacement rate adopted here is the slowest one used ($3 \cdot 10^{-5}$ mm/s).

7.1.2 J curves, J_Q and Hydrogen embrittlement ratio

Figure 7.2 shows the J-resistance curves obtained following the procedure described in Section 6.3.

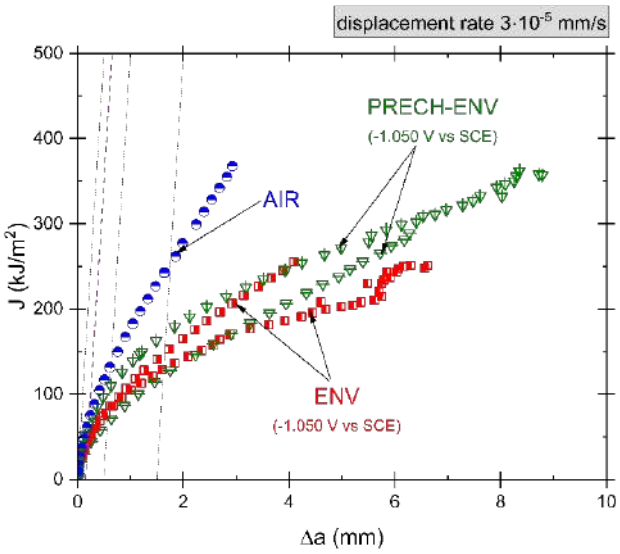

Figure 7.2: J-integral curves for different scenarios for the test rate $3 \cdot 10^{-5}$ mm/s

In this case, the J–Δa curves are noticeably more compressed towards lower values when compared with those obtained for the steel A. In particular, even the test performed in air assumed a very low initiation value, with $J_Q = 69.4$ kJ/m^2 (Table 7.1), in contrast with the corresponding air test on SE(B) in steel A, which exhibited $J_Q = 576$ kJ/m^2.

Table 7.1: Evaluation of J_Q and Hydrogen Embrittlement Ratio (HER) for the slow displacement rate ($3{\cdot}10^{-5}$ mm/s), steel B.

TEST CONDITION	J_Q [kJ/m^2]	HER%
AIR	69.4	–
ENV	51.44	25.9%
(-1.050 V vs SCE)	39.6	42.9%
PRECH-ENV	39.55	43%
	48.31	30.4%

This behaviour indicates a limited ductility during crack propagation, even in the absence of hydrogen, most likely attributable to the material's age and microstructure (Chapter 3), which contains inclusions that compromise its plasticity.

The curves obtained under cathodic polarisation are essentially superimposed onto the air curve, at least in the initial portion, which is the region used to determine the crack-initiation energy. Moreover, only minor differences are observed along the remainder of the curves, indicating that hydrogen charging has a comparatively limited influence on the overall J-resistance behaviour of the steel B.

Fractographic analysis of the specimen surfaces corroborates the observations inferred from the J–Δa curves (Figure 7.3). The fracture surfaces of specimens tested under cathodic polarisation (ENV) and under cathodic precharging maintained during the mechanical test (PRECH-ENV) are comparable and exhibit very similar features. The material, which is particularly rich in elongated inclusions along the rolling direction, promotes defect propagation with localised tearing adjacent to the inclusion zones. Crack propagation is poorly ductile: the presence of dimples is limited and interspersed with relatively large, flat quasi-cleavage facets, which facilitate rapid crack growth with limited plastic deformation, as also observed in the fracture surfaces of specimens tested in air, thus confirming the previously discussed results.

7.1.3 Crack propagation rate, CTOD and CTOA

By elaborating the curves as described in Section 6.3, it is possible to construct the plot shown in Figure 7.4, which confirms that crack propagation is monotonic after reaching the maximum load for each curve and test condition. This indicates that crack growth is stable and exhibits plastic behaviour.

The tests performed under cathodic polarisation are comparable to those conducted in air and show slightly higher slopes. This observation corroborates the previous analysis: the steel B exhibits limited ductility even in air, resulting in relatively rapid crack growth. Nevertheless, the propagation behaviour remains comparable under different environmental conditions, as confirmed by the similar slopes observed in the stable propagation region.

It can again be assumed that a configuration exists which remains stable during crack propagation, as shown in Figure 7.5. In the initial portion of the curve, negligible crack growth rates are observed. Once a characteristic K_{JQ} value is reached, the crack begins to propagate, and the propagation rate rapidly increases until reaching approximately constant values, as indicated by the densely clustered points at the end of the vertical part.

Notably, in this case, no significant differences are observed between the behaviour in air and under hydrogen loading, in contrast to the results obtained for the steel A. This observation further confirms the findings reported so far regarding the limited

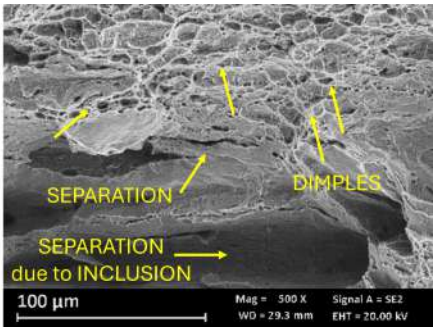

(a) Surface of test in AIR.

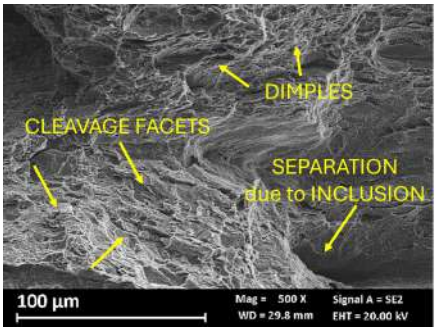

(b) Surface of test in ENV at -1.050 V vs SCE.

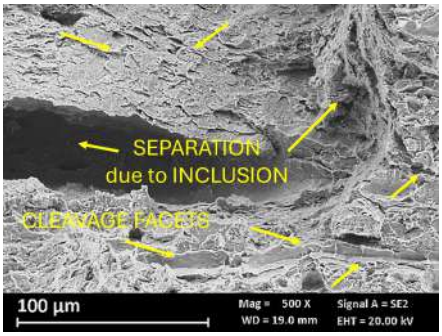

(c) Surface of test in PRECH-ENV both at -1.050 V vs SCE.

Figure 7.3: Fractographic analysis of SE(B) specimens from the steel B under different conditions.

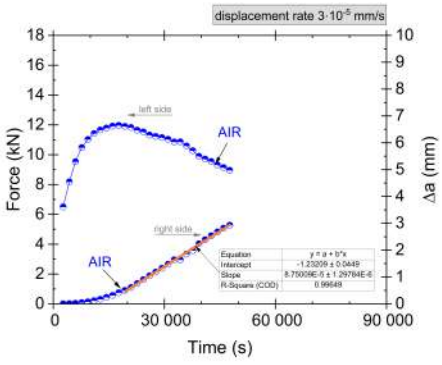

(a) Elaboration under AIR environment.

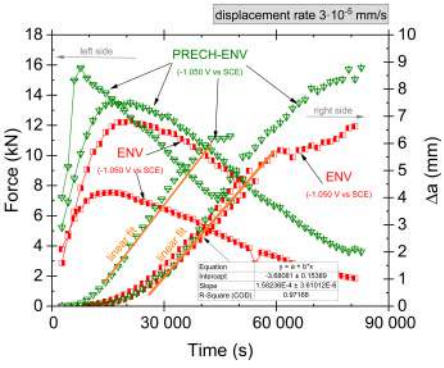

(b) Elaboration under environmental hydrogen exposure (ENV).

Figure 7.4: Elaboration of load versus testing time (right) and crack growth versus testing time (left) under different test conditions at $3 \cdot 10^{-5}$ mm/s displacement rate.

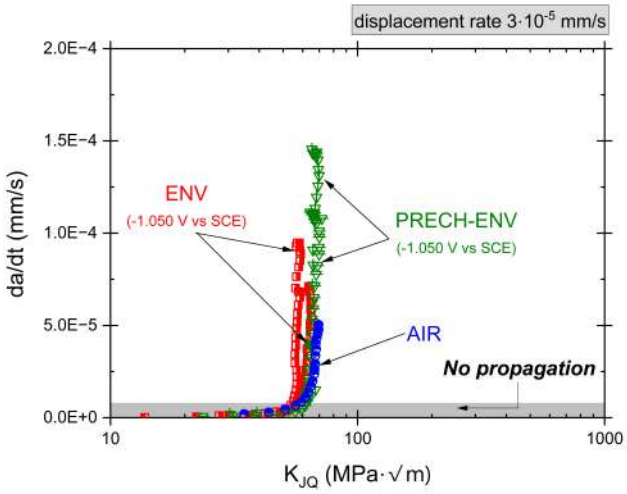

Figure 7.5: Stress Intensity Factor as a function of crack growth rate under different hydrogen conditions, test rate $3 \cdot 10^{-5}$ mm/s

ductility and relatively rapid crack propagation of the steel B. These conclusions are also supported by the CTOD and CTOA analyses shown in Figure 7.6.

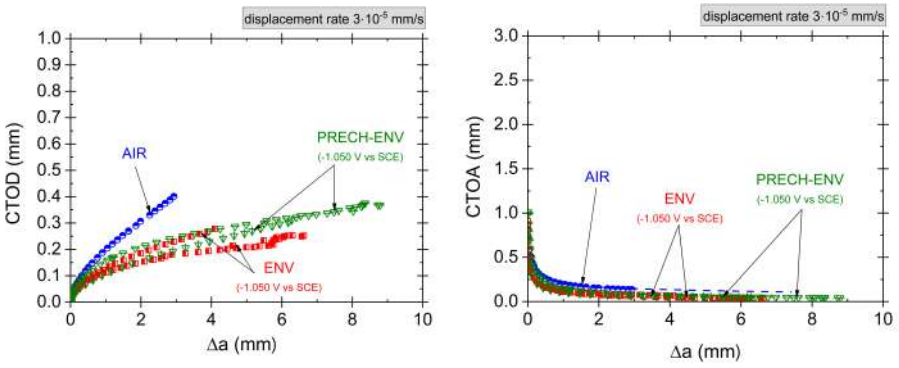

(a) CTOD under air and environmental conditions. **(b)** CTOA under air and environmental conditions.

Figure 7.6: Comparison of different conditions on crack tip opening displacement and crack tip opening angle at $3 \cdot 10^{-5}$ mm/s displacement rate.

7.1.4 Strain rate

By analysing the time evolution of the CTOD and CTOA parameters, the crack propagation rate can be estimated, as discussed in Section 6.4.4. The results are presented in Figure 7.7.

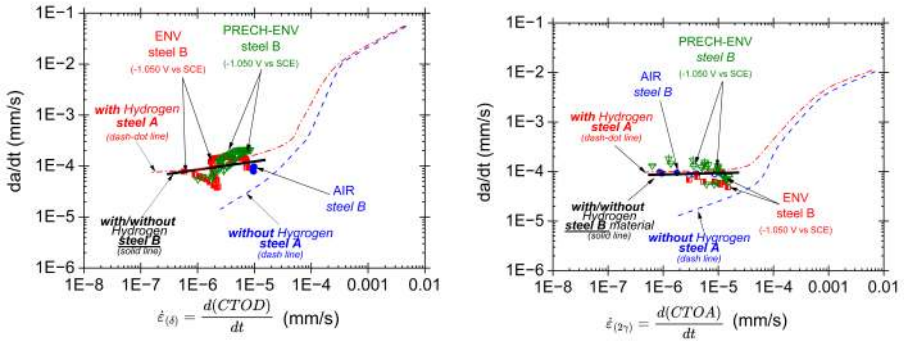

(a) Strain rate estimated from CTOD. **(b)** Strain rate estimated from CTOA.

Figure 7.7: Strain rate diagram versus crack growth rate in different scenarios investigated of steel B.

As observed, there are once again no significant differences in the estimated strain rates, whether derived from CTOD or CTOA. Furthermore, the data points for tests conducted in air are practically superimposed on those obtained under environmental conditions, as highlighted by the solid black line in the figure.

A slight effect is noticeable, whereby tests conducted under hydrogen or with precharging exhibit marginally higher crack propagation rates at comparable strain rates than those in air. However, in this case, the results are essentially overlapping. This behaviour is further emphasised when these values are compared with the performance of the steel A, represented by the dashed interpretative lines in the figure. For the steel A, a pronounced difference is observed between tests conducted with and without hydrogen, whereas for the steel B this variation is limited, if not negligible.

7.1.5 HACx interpretation

To evaluate the effect of hydrogen on the steel B, it is possible to estimate the value of the hydrogen-assisted cracking parameter, as defined in Equation (6.17) and shown in Figure 7.8.

In this case, there is evidently no significant difference between the values estimated in air and in hydrogen for the steel B, with all values converging to approximately 0.6

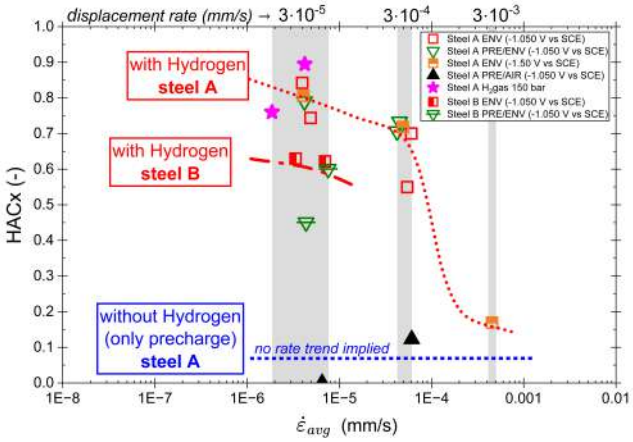

Figure 7.8: Comparison of different Hydrogen Assisted Cracking index estimated from steel A and B.

at comparable strain rates. However, these values are lower than the corresponding values observed for the steel A under all loading conditions, whether electrochemical (even at higher polarisation potentials) or gaseous.

This behaviour can be attributed to the inherently limited ductility of the steel B, even in air, which is comparable to its behaviour in the presence of hydrogen. Consequently, when the crack propagation rates in hydrogen and in air are similar, the hydrogen index approaches zero, indicating that hydrogen has little influence on the propagation behaviour. Conversely, if the ratio becomes large—i.e., a small propagation rate in air and a significantly higher one in hydrogen—the denominator becomes negligible and the index tends towards one, corresponding to maximum susceptibility.

Therefore, the hydrogen index should be interpreted as a parameter quantifying the aggravating effect of hydrogen at the crack tip on the propagation rate. By itself, it does not provide information on the absolute mechanical properties of the material. A relatively low index simply indicates that hydrogen does not significantly alter the crack growth rate compared with air. However, if the material already exhibits limited ductility in air, and thus relatively high crack propagation rates under air conditions, the propagation rate in a hydrogen-containing environment will be similar to that in air. As a result, the index remains low.

This implies that, for materials with inherently low ductility, the contribution of hydrogen to crack growth acceleration is limited, as the material is already mechanically

unable to absorb significant deformation energy before crack propagation occurs. Accordingly, the hydrogen index must be considered in conjunction with other parameters describing the mechanical behaviour of the material, such as Charpy impact toughness, tensile properties, and other relevant mechanical characterisation results.

Conclusion

The study provided a comprehensive assessment of hydrogen interactions with pipeline steels. In particular, for the steels investigated, and based on the results obtained and the discussion presented, the following key observations can be summarised:

- Hydrogen reduces the fracture resistance, as measured by J_Q and K_{JQ}, with values decreasing during tests under hydrogen charging. This effect depends on the strain rate at the crack tip, and thus on the displacement rate.
- The influence of hydrogen depends by the synergistic effect of hydrogen charging during the mechanical test, whereas pre-charging followed by testing in air alone has a negligible effect. Therefore, *in situ*-hydrogen charging during testing is necessary to properly evaluate the effect of hydrogen, whether introduced in the gas phase or by electrochemical means.
- The equivalence between gas-phase and electrochemical hydrogen charging was evaluated through hydrogen uptake and permeation experiments. To achieve the same hydrogen uptake under cathodic protection conditions corresponding to a potential of -1.050 VvsSCE, a hydrogen pressure of 150 bar is required, which matches the conditions under which the specimens were tested.
- The crack growth rate increases in presence of hydrogen by approximately a factor of three only at low strain rates (10^{-5} mm s^{-1}), whereas its effect is negligible at higher displacement rates.
- Crack propagation under in-situ hydrogen charging was associated with a lower crack tip opening angle (CTOA) compared with air or nitrogen environments, indicating brittle propagation of semi-cleavage typical of hydrogen embrittlement.
- A parameter, denoted as *HACx*, was defined to quantify the susceptibility to hydrogen embrittlement. Steel B, despite exhibiting a lower initial fracture

toughness, shows a smaller relative reduction in fracture resistance compared with Steel A. Nevertheless, Steel A demonstrates superior overall performance in the presence of hydrogen.

References

[1] V Masson-Delmotte et al. *Global Warming of 1.5°C: IPCC Special Report on Impacts of Global Warming of 1.5°C*. IPCC, 2022.

[2] D. W. Barns, J. A. Edmonds, and J. M. Reilly. *Use of the Edmonds-Reilly model to model energy-related greenhouse gas emission*. Tech. rep. EEA, 2011.

[3] V. E. Onyebuchi et al. "A systematic review of key challenges of CO transport via pipelines". In: *Renewable and Sustainable Energy Reviews* 81 (2018), pp. 2563–2583. DOI: 10.1016/j.rser.2017.06.064.

[4] Z Hausfather. *Global CO2 Emissions Have Been Flat for a Decade, New Data Reveals. Carbon Brief; 2021*. 2021.

[5] N. Yang et al. "Experimental investigation of the characteristics of combustion in the full hydrogen blending range of methane-hydrogen mixtures in a MILD model combustor". In: *International Journal of Hydrogen Energy* 65 (2024), pp. 252–261. ISSN: 0360-3199. DOI: https://doi.org/10.1016/j.ijhydene.2024.04.013.

[6] S. Xu et al. "Effect of hydrogen-blending ratio and wall temperature on establishment, NO formation, and heat transfer of hydrogen-enriched methane MILD combustion". In: *Fuel* 369 (2024), p. 131787. ISSN: 0016-2361.

[7] M. Sofian et al. "A review on hydrogen blending in gas network: Insight into safety, corrosion, embrittlement, coatings and liners, and bibliometric analysis". In: *International Journal of Hydrogen Energy* 60 (2024), pp. 867–889. DOI: 10.1016/j.ijhydene.2024.02.166.

[8] N. Bullerdiek, U. Neuling, and M. Kaltschmitt. *Powerfuels: Status and Prospects*. Springer Nature, 2024.

[9] B. Tiar et al. "Navigating Algeria towards a sustainable green hydrogen future to empower North Africa and Europe's clean hydrogen transition". In: *International Journal of Hydrogen Energy* 61 (2024), pp. 783–802. DOI: 10.1016/j.ijhydene.2024.02.328.

[10] A. Laureys et al. "Use of existing steel pipeline infrastructure for gaseous hydrogen storage and transport: A review of factors affecting hydrogen induced degradation". In: *Journal of Natural Gas Science and Engineering* 101 (May 2022), p. 104534. DOI: 10.1016/j.jngse.2022.104534.

[11] R.P. Gangloff and B.P. Somerday. *Gaseous Hydrogen Embrittlement of Materials in Energy Technologies*. Vol. 1. Woodhead Publishing, 2012. DOI: 10.1016/B978-1-84569-677-1.50024-7.

[12] X. Wu et al. “From the perspective of new technology of blending hydrogen into natural gas pipelines transmission: Mechanism, experimental study, and suggestions for further work of hydrogen embrittlement in high-strength pipeline steels”. In: *International Journal of Hydrogen Energy* 47 (2022), pp. 8071–8090. DOI: 10.1016/j.ijhydene.2021.12.108.

[13] M. Röthig et al. “A review of gas phase inhibition of gaseous hydrogen embrittlement in pipeline steels”. In: *International Journal of Hydrogen Energy* 60 (2024), pp. 1239–1265. DOI: 10.1016/j.ijhydene.2024.02.245.

[14] B. Meng et al. “Hydrogen effects on X80 pipeline steel in high-pressure natural gas/hydrogen mixtures”. In: *International Journal of Hydrogen Energy* 42 (2017), pp. 7404–7412. DOI: 10.1016/j.ijhydene.2016.05.145.

[15] C. Mendibide et al. “Effect of degraded environmental conditions on the service behavior of an X65 pipeline steel not designed for hydrogen transport”. In: *International Journal of Hydrogen Energy* 52 (2024), pp. 1019–1032. DOI: 10.1016/j.ijhydene.2023.05.309.

[16] H. Yang et al. “Effects of defect on the hydrogen embrittlement behavior of X80 pipeline steel in hydrogen-blended natural gas environments”. In: *Int J Hydrogen Energy* 58 (2024), pp. 158–173. DOI: 10.1016/j.ijhydene.2024.01.107.

[17] J. Sánchez-Laínez et al. “Enabling the injection of hydrogen in high-pressure gas grids: Investigation of the impact on materials and equipment”. In: *International Journal of Hydrogen Energy* 52 (2024), pp. 1007–1018. DOI: 10.1016/j.ijhydene.2023.05.220.

[18] Laurent B. et al. “Industrial consequences of hydrogen embrittlement”. In: *Mechanics-Microstructure-Corrosion Coupling*. Elsevier, 2019, pp. 223–244.

[19] M. Nagumo. *Fundamentals of hydrogen embrittlement*. Springer, 2016. DOI: 10.1007/978-981-10-0161-1.

[20] S. Lynch. “Hydrogen embrittlement phenomena and mechanisms”. In: *Corrosion Reviews* 30 (2012), pp. 105–123. DOI: 10.1515/CORRREV-2012-0502.

[21] X. Li et al. “Review of Hydrogen Embrittlement in Metals: Hydrogen Diffusion, Hydrogen Characterization, Hydrogen Embrittlement Mechanism and Prevention”. In: *Acta Metallurgica Sinica (English Letters)* 33 (2020), pp. 759–773. DOI: 10.1007/s40195-020-01039-7.

[22] D. Hardie et al. “Hydrogen embrittlement of stainless steel overlay materials for hydrogenators”. In: *Corrosion Science* 46 (2004), pp. 3089–3100. DOI: 10.1016/j.corsci.2004.03.017.

[23] J. Hoschke et al. “A review of hydrogen embrittlement in gas transmission pipeline steels”. In: *Corrosion Reviews* 41 (2023), pp. 277–317. DOI: 10.1515/CORRREV-2022-0052.

[24] M. Cabrini et al. “Hydrogen embrittlement behavior of HSLA line pipe steel under cathodic protection”. In: *Corrosion Reviews* 29 (2011), pp. 261–274. DOI: 10.1515/CORRREV.2011.009.

[25] A. Hamed et al. “Assessing the hydrogen embrittlement susceptibility of an existing L360NB natural gas pipeline steel for 100% hydrogen transport”. In: *Corrosion Science* 244 (2025). DOI: 10.1016/j.corsci.2024.112648.

[26] L. B. Peral et al. “Effect of electrochemical charging on the hydrogen embrittlement susceptibility of a low-alloyed tempered martensitic steel submitted to high internal pressure”. In: *International Journal of Hydrogen Energy* 63 (2024), pp. 657–667. DOI: 10.1016/j.ijhydene.2024.03.034.

[27] R.N. Iyer and H.W. Pickering. “Mechanism and kinetics of electrochemical hydrogen entry and degradation of metallic systems”. In: *Annual Review of Materials Science* 20 (1990), pp. 299–338.

[28] R.K. Dayal and N. Parvathavarthini. “Hydrogen embrittlement in power plant steels”. In: *Sadhana* 28 (2003), pp. 431–451.

[29] A. Pundt and R. Kirchheim. “Hydrogen in metals: microstructural aspects”. In: *Annual Review of Materials Research* 36.1 (2006), pp. 555–608.

[30] S. Myers et al. “Hydrogen interactions with defects in crystalline solids”. In: *Reviews of Modern Physics* 64 (1992), pp. 559–617.

[31] C. Borchers, T. Michler, and A. Pundt. “Effect of hydrogen on the mechanical properties of stainless steels”. In: *Advanced Engineering Materials* 10 (2008), pp. 11–23.

[32] J. Song and W.A. Curtin. “Atomic mechanism and prediction of hydrogen embrittlement in iron”. In: *Nature Materials* 12 (2013), pp. 145–151.

[33] H.K. Birnbaum. “Hydrogen effects on deformation and fracture: science and sociology”. In: *MRS Bulletin* 28.7 (2003), pp. 479–485.

[34] M. Dadfarnia et al. “Recent advances in the study of structural materials compatibility with hydrogen”. In: *Advanced Materials* 22.10 (2010), pp. 1128–1135.

[35] A. Barnoush and H. Vehoff. “Recent developments in the study of hydrogen embrittlement: hydrogen effect on dislocation nucleation”. In: *Acta Materialia* 58.16 (2010), pp. 5274–5285.

[36] R.P. Gangloff. “Science-based prognosis to manage structural alloy performance in hydrogen”. In: *Effects of Hydrogen on Materials: Proceedings of the 2008 International Hydrogen Conference*. Ed. by B. Somerday, P. Sofronis, and R. Jones. Conference held September 7–10, 2008. Jackson Lake, Wyoming, USA, 2008.

[37] Z. Peng et al. “Effect of Slow Strain Rates on the Hydrogen Migration and Different Crack Propagation Modes in Pipeline Steel”. In: *Steel Research International* 94 (2023). DOI: 10.1002/srin.202300070.

[38] E. Entezari et al. “Experimental Study on Hydrogen Embrittlement Behavior of X80 and X70 Pipeline Steels Evaluated by Hydrogen Permeation and Slow Strain Rate Tensile Tests”. In: *Journal of Failure Analysis and Prevention* (2024). DOI: 10.1007/s11668-024-02042-1.

[39] C. Wang et al. “Study on hydrogen embrittlement susceptibility of X80 steel through in-situ gaseous hydrogen permeation and slow strain rate tensile tests”. In: *International Journal of Hydrogen Energy* 48 (2023), pp. 243–256. DOI: 10.1016/j.ijhydene.2022.09.228.

[40] H.J. Kim et al. “Pre-strain and hydrogen charging effect on the plastic and fracture behavior of quenching and partitioning (Q&P) steel”. In: *Acta Mater* 263 (2024). DOI: 10.1016/j.actamat.2023.119524.

[41] F. Konert et al. “Evaluation of the impact of gaseous hydrogen on pipeline steels utilizing hollow specimen technique and CT”. In: *Int J Hydrogen Energy* 59 (2024), pp. 874–879. DOI: 10.1016/j.ijhydene.2024.02.005.

[42] A. M. Marshall, A. Klar, and RJ. Mair. “Tunneling beneath buried pipes: view of soil strain and its effect on pipeline behavior”. In: *Journal of Geotechnical and Geoenvironmental Engineering* 136.12 (2010), pp. 1664–1672.

[43] D. Wijewickreme, H. Karimian, and D. Honegger. “Response of buried steel pipelines subjected to relative axial soil movement”. In: *Canadian Geotechnical Journal* 46.7 (2009), pp. 735–752.

[44] L. Li et al. “Effect of corrosion and hydrogen embrittlement on microstructure and mechanical properties of mild steel”. In: *Construction and Building Materials* 170 (2018), pp. 78–90.

[45] S.K. Dwivedi and M. Vishwakarma. “Hydrogen embrittlement in different materials: a review”. In: *International Journal of Hydrogen Energy* 43 (2018), pp. 21603–21616.

[46] G. Pluvinage. “Mechanical properties of a wide range of pipe steels under influence of pure hydrogen or hydrogen blended with natural gas”. In: *International Journal of Pressure Vessels and Piping* 190 (2021), p. 104293.

[47] J. O’M. Bockris and P. K. Subramanyan. “The equivalent pressure of molecular hydrogen in cavities within metals in terms of the overpotential developed during the evolution of hydrogen”. In: *Electrochimica Acta* 16 (1971), pp. 2169–2179. DOI: 10.1016/0013-4686(71)85027-2.

[48] J. O’M Bockris and A. Azzam. “The kinetics of the hydrogen evolution reaction at high current densities”. In: *Transactions of the Faraday Society* 48 (1952), pp. 145–160.

[49] A. Atrens et al. “Electrochemical studies of hydrogen diffusion and permeability in Ni”. In: *Corrosion Science* 20 (1980), pp. 673–684. DOI: 10.1016/0010-938X(80)90102-X.

[50] D. Landolt. *Corrosion et chimie de surfaces des matériaux*. Lausanne: Presses Polytechniques et Universitaires Romandes, 1993, pp. 413–462.

[51] A. Staykov, J. Yamabe, and B. Somerday. “Effect of Hydrogen Gas Impurities on the Hydrogen Dissociation on Iron Surface”. In: *International Journal of Quantum Chemistry* 114.10 (2014), pp. 626–635. DOI: 10.1002/qua.24586.

[52] J. Lennard-Jones. “Processes of Adsorption and Diffusion on Solid Surfaces”. In: *Transactions of the Faraday Society* 28 (1932), pp. 333–359.

[53] A. A. Pisarev. “Hydrogen Adsorption on the Surface of Metals”. In: *Gaseous Hydrogen Embrittlement of Materials in Energy Technologies*. Ed. by Richard P. Gangloff and Brian P. Somerday. Vol. 1. Woodhead Publishing, 2012, pp. 3–33.

[54] D. A. Jones. *Principles and Prevention of Corrosion*. Upper Saddle River, NJ: Prentice Hall, 1992.

[55] M. Pourbaix. *Atlas of electrochemical equilibria*. Pergamon press, 1966.

[56] P. Marcus. *Corrosion Mechanisms in Theory and Practice: Third Edition*. CRC Press, 2011, pp. 1–905.

[57] H. Kaesche. *Metallic Corrosion*. Original title in German, translated edition. NACE International, 2003.

[58] Q. Liu et al. "Determination of the hydrogen fugacity during electrolytic charging of steel". In: *Corrosion Science* 87 (2014), pp. 239–258. DOI: 10.1016/j.corsci.2014.06.033.

[59] J. O'M. Bockris, J. McBreen, and L. Nanis. "The Hydrogen Evolution Kinetics and Hydrogen Entry into α-Iron". In: *Journal of the Electrochemical Society* 112 (1965), p. 1025. DOI: 10.1149/1.2423335.

[60] J. McBreen, L. Nanis, and W. Beck. "A Method for Determination of the Permeation Rate of Hydrogen Through Metal Membranes". In: *Journal of the Electrochemical Society* 113 (1966), p. 1218. DOI: 10.1149/1.3087209.

[61] J. O'M. Bockris, M. A. Genshaw, and M. Fullenwider. "The Electro-permeation of Hydrogen into Metals". In: *Electrochimica Acta* 15 (1970), pp. 47–60. DOI: 10.1016/0013-4686(70)90006-X.

[62] A. Lasia and D. Grégoire. "General Model of Electrochemical Hydrogen Absorption into Metals". In: *Journal of the Electrochemical Society* 142 (1995), pp. 3393–3399. DOI: 10.1149/1.2050267.

[63] W. Beck et al. "Diffusivity and Solubility of Hydrogen as a Function of Composition in Fe-Ni Alloys". In: (n.d.). No publication year or source specified.

[64] J. Rodrigues, J. Torres, and E. O. Vilar. "Hydrogen permeation in metlas and alloys: a brief review". In: *International Journal of Development Research* 12 (09 Sept. 2022), pp. 58509–58516. DOI: https://doi.org/10.37118/ijdr.25006.09.2022.

[65] R. Ash and R. M. Barrer. "Diffusion with a concentration discontinuity: The hydrogen-palladium system". In: *Journal of Physics and Chemistry of Solids* 16.3–4 (1960), pp. 246–252.

[66] I. A. Bagotskaya. "Effect of the solution composition on the diffusion rate of electrolytic hydrogen through metallic diaphragms. I. Diffusion of hydrogen through iron diaphragms". In: *Zhurnal Fizicheskoi Khimii* 36.12 (1962), pp. 2667–2673.

[67] A. N. Frumkin. In: *Advances in Electrochemistry and Electrochemical Engineering*. Ed. by P. Delahay. Vol. 3. New York: Interscience, 1963, p. 287.

[68] J. M. Chen and J. K. Wu. "The application of electroplating for prevention of hydrogen embrittlement in AISI 4140 steel". In: *Plating and Surface Finishing* 79 (1992), pp. 74–74.

[69] C. Montella. "EIS study of hydrogen insertion under restricted diffusion conditions: I. Two-step insertion reaction". In: *Journal of Electroanalytical Chemistry* 497.1–2 (2001), pp. 3–17.

[70] C. Gabrielli et al. "Investigation of hydrogen adsorption-absorption into thin palladium films: I. Theory". In: *Journal of The Electrochemical Society* 151.11 (2004), A1925.

[71] A. Lasia. “Applications of electrochemical impedance spectroscopy to hydrogen adsorption, evolution and absorption into metals”. In: *Modern Aspects of Electrochemistry*. Boston, MA: Springer, 2002, pp. 1–49.

[72] C. San Marchi and B. P. Somerday. *SANDIA REPORT Technical Reference for Hydrogen Compatibility of Materials*. Tech. rep. Sandia National Laboratories, 2012.

[73] J. Venezuela et al. “Determination of the equivalent hydrogen fugacity during electrochemical charging of 3.5NiCrMoV steel”. In: *Corrosion Science* 132 (2018), pp. 90–106. DOI: 10.1016/j.corsci.2017.12.018.

[74] E. Koren et al. “Experimental comparison of gaseous and electrochemical hydrogen charging in X65 pipeline steel using the permeation technique”. In: *Corrosion Science* 215 (Feb. 2023). DOI: 10.1016/j.corsci.2023.111025. URL: https://doi.org/10.1016/j.corsci.2023.111025.

[75] K. Kiuchi and R. B. McLellan. “The solubility and diffusivity of hydrogen in well-annealed and deformed iron”. In: *Transactions of the Metallurgical Society of AIME* 14 (1983). Reprinted from earlier work, pp. 1545–1551.

[76] T. Michler, F. Schweizer, and K. Wackermann. “Review on the influence of temperature upon hydrogen effects in structural alloys”. In: *Metals* 11.3 (2021), p. 423. DOI: 10.3390/met11030423. URL: https://doi.org/10.3390/met11030423.

[77] C. San Marchi, B. Somerday, and S. Robinson. “Permeability, Solubility and Diffusivity of Hydrogen Isotopes in Stainless Steels at High Gas Pressures”. In: *International Journal of Hydrogen Energy* 32 (2007), pp. 100–116.

[78] W. Choo, J. Lee, and C. Cho. “Effect of grain size”. In: *Materials Science* 16 (1981), pp. 1285–1293.

[79] C. Wert. “Trapping of hydrogen in metals”. In: *Hydrogen in Metals II. Application-oriented Properties*. Springer-Verlag, 1978, pp. 305–330.

[80] J. Yao and J. Cahoon. “Theoretical modeling of grain boundary diffusion of hydrogen and its effect on permeation curves”. In: *Acta Metallurgica et Materialia* 39 (1991), pp. 119–126.

[81] G.T. Park et al. “Effect of microstructure on the hydrogen trapping efficiency and hydrogen induced cracking of linepipe steel”. In: *Corros Sci* 50 (2008), pp. 1865–1871. DOI: 10.1016/j.corsci.2008.03.007.

[82] A. J. Haq et al. “Effect of microstructure and composition on hydrogen permeation in X70 pipeline steels”. In: *International Journal of Hydrogen Energy* 38.5 (2013), pp. 2544–2556.

[83] M. Ichimura, Y. Sasajima, and M. Imabayashi. “Grain boundary effect on diffusion of hydrogen in pure aluminum”. In: *Materials Transactions JIM* 32 (1991), pp. 1109–1114.

[84] N. Yazdipour et al. “2D modelling of the effect of grain size on hydrogen diffusion in X70 steel”. In: *Computational Materials Science* 56 (2012), pp. 49–57.

[85] M Cabrini et al. “Effetto della diffusione dell’idrogeno sui fenomeni di EAC di acciai per pipeline in condizioni di protezione catodica”. In: *La Metallurgia Italiana* 2 (2008), pp. 15–22.

[86] O. Cogliati and M. Cabrini. “Effetto della microstruttura sulla diffusione dell’idrogeno in acciai al carbonio per pipeline”. In: *La Metallurgia Italiana* 3 (2003), pp. 13–20.

[87] M. Cabrini et al. “Hydrogen diffusion and EAC of pipeline steels under cathodic protection”. In: *16th European Conference of Fracture*. Alexandroupolis, Greece, 2006.

[88] L. Tau and S. Chan. “Effects of ferrite/pearlite alignment on the hydrogen permeation in a AISI 4130 steel”. In: *Materials Letters* 29 (1996), pp. 143–147.

[89] M. Luppo and J. Ovejero-Garcia. “The influence of microstructure on the trapping and diffusion of hydrogen in a low carbon steel”. In: *Corrosion Science* 32.10 (1991), pp. 1125–1133.

[90] V. Gadgeel and D. Johnson. “Gas-Phase Hydrogen Permeation and Diffusion in Carbon Steels as a Function of Carbon Content from 500 to 900 K”. In: *Journal of Materials for Energy Systems* 2 (1979), pp. 32–40.

[91] V. Olden, A. Senumstad Hauge, and O. Magne Akselsen. “The Influence of Plastic Strain on the Effective Hydrogen Diffusion Coefficient and Trapping in Base Metal and Weld Simulated Heat Affected Zone of an X70 Pipeline Steel”. In: *Proceedings of the Twenty-second International Offshore and Polar Engineering Conference*. 2012.

[92] M. Skjellerudsveen et al. “Effect of microstructure and temperature on hydrogen diffusion and trapping in X70 grade pipeline steel and its weldments”. In: *Proceedings of the 2010 EUROCORR*. Moscow, Russia, 2010.

[93] W. Zhao et al. “Insights into the role of CO in inhibiting hydrogen embrittlement of X80 steel weld at different hydrogen blending ratios”. In: *International Journal of Hydrogen Energy* 50 (2024), pp. 292–302. DOI: 10.1016/j.ijhydene.2023.10.167.

[94] D. Guedes et al. “The role of plasticity and hydrogen flux in the fracture of a tempered martensitic steel: A new design of mechanical test until fracture to separate the influence of mobile from deeply trapped hydrogen”. In: *Acta Materialia* 186 (2020), pp. 133–148. DOI: 10.1016/j.actamat.2019.12.045.

[95] J. H. Sir. William. “On some remarkable changes produced in iron and steel by the action of hydrogen and acids”. In: *Nature* 11 (1875), pp. 393–393.

[96] A. Oudriss et al. “Consequence of the diffusive hydrogen contents on tensile properties of martensitic steel during the desorption at room temperature”. In: *Materials Science and Engineering: A* 598 (2014), pp. 420–428. DOI: 10.1016/j.msea.2014.01.039.

[97] R. L. S. Thomas, J. R. Scully, and R. P. Gangloff. “Internal hydrogen embrittlement of ultrahigh-strength AERMET 100 steel”. In: *Metallurgical and Materials Transactions A* 34 (2003), pp. 327–344. DOI: 10.1007/s11661-003-0334-3.

[98] A. B. Hagen et al. “Experimental determination of equivalent hydrogen gas pressure from electrochemical hydrogen charging”. In: *International Journal of Hydrogen Energy* 82 (2024), pp. 1146–1156. DOI: 10.1016/j.ijhydene.2024.02.117.

[99] A. Zafra et al. “Comparison of hydrogen diffusivities measured by electrochemical permeation and temperature-programmed desorption in cold-rolled pure iron”. In: *J Nat Gas Sci Eng* 98 (2022). DOI: 10.1016/j.jngse.2021.104365.

[100] E. Masato, H. Daisuke, and T. Toshimi. “Modeling Thermal Desorption Analysis of Hydrogen in Steel”. In: *ISIJ International* 46 (2006), pp. 1381–1387.

[101] E.I. Galindo-Nava, B.I.Y. Basha, and P.E.J. Rivera-Díaz-del-Castillo. “Hydrogen transport in metals: Integration of permeation, thermal desorption and degassing”. In: *J Mater Sci Technol* 33 (2017), pp. 1433–1447. DOI: 10.1016/j.jmst.2017.09.011.

[102] A. Demarez, A.G. Hock, and F.A. Meunier. “Diffusion of hydrogen in mild steel”. In: *Acta Metallurgica* 2 (1954), pp. 214–223. DOI: 10.1016/0001-6160(54)90162-5.

[103] J. Ovejero-García. “Hydrogen microprint technique in the study of hydrogen in steels”. In: *J Mater Sci* 20 (1985), pp. 2623–2629. DOI: 10.1007/BF00556094.

[104] C. Poole. *Gas Chromatography*. Elsevier, 2021.

[105] L. Cupertino-Malheiros et al. “Hydrogen uptake kinetics of cathodic polarized metals in aqueous electrolytes”. In: *Corrosion Science* 231 (2024), p. 111959.

[106] “Method of measurement of hydrogen permeation and determination of hydrogen uptake and transport in metals by an electrochemical technique”. In: (2014). International Standard ISO 17081.

[107] “Standard Practice for Evaluation of Hydrogen Uptake, Permeation, and Transport in Metals by an Electrochemical Technique”. In: (2003). ASTM G148-97.

[108] H. Addach et al. “Study of the electrochemical permeation of hydrogen in iron”. In: *Corros Sci* 51 (2009), pp. 263–267. DOI: 10.1016/j.corsci.2008.10.024.

[109] M. Yan and Y. Weng. “Study on hydrogen absorption of pipeline steel under cathodic charging”. In: *Corros Sci* 48 (2006), pp. 432–444. DOI: 10.1016/J.CORSCI.2005.01.011.

[110] R McKibben et al. “A potentiostatic double-step method for measuring hydrogen atom diffusion and trapping in metal electrodes—I. Theory”. In: *Acta metallurgica* 35.1 (1987), pp. 253–262.

[111] B.G. Pound, G.A. Wright, and R.M. Sharp. “A potentiostatic double-step method for measuring hydrogen atom diffusion and trapping in metal electrodes-II. Experimental”. In: (1987).

[112] R. Oriani. “The diffusion and trapping of hydrogen in steel”. In: *Acta Metallurgica* 18.1 (1970), pp. 147–157.

[113] J. P. Hirth. “Effects of Hydrogen on the Properties of Iron and Steel”. In: *Metallurgical Transactions A* 11A (1980), pp. 861–890.

[114] J. O’M. Bockris et al. “The effect of stress on the chemical potential of hydrogen in iron and steel”. In: *Acta Metallurgica* 19 (1971), pp. 1209–1217.

[115] W. Choo and J. Lee. “Effect of cold working on the hydrogen trapping phenomena in pure iron”. In: *Metallurgical Transactions A* 14.7 (1983), pp. 1299–1305.

[116] S. Xie and J. P. Hirth. “Permeation of hydrogen, trapping, and damage in spheroidized AISI 1090 steel”. In: *Corrosion* 38.9 (Sept. 1982), pp. 486–493.

[117] T. Radhakrishnan and L. Shreir. “Hydrogen permeation through iron and steel by electrochemical transfer—II. Influence of metallurgical factors on hydrogen permeation”. In: *Electrochimica Acta* 12.7 (July 1967), pp. 889–903.

[118] R. M. Hudson and G. L. Straagand. “Effect of cold drawing on hydrogen behavior in steel”. In: *Corrosion* 16.5 (May 1960), 253t–258t.

[119] E. Fallahmohammadi, F. Bolzoni, and L. Lazzari. “Measurement of lattice and apparent diffusion coefficient of hydrogen in X65 and F22 pipeline steels”. In: *Int J Hydrogen Energy* 38 (2013), pp. 2531–2543. DOI: 10.1016/j.ijhydene.2012.11.059.

[120] W. Qu et al. “Effect of plastic deformation at room temperature on hydrogen diffusion of S30408”. In: *International Journal of Hydrogen Energy* 44.17 (2019), pp. 8751–8758.

[121] W. Beck et al. “Hydrogen permeation in metals as a function of stress, temperature and dissolved hydrogen concentration”. In: *Proceedings of the Royal Society*. A 290.1421 (1966), pp. 220–235.

[122] M. Cabrini, G. Razzini, and M. Tarenzi. “Hydrogen Permeation and Embrittlement of a Low Alloyed Steel”. In: *Proceedings of NACE International Conference “Corrosion in Natural and Industrial Environments: Problems and Solutions”*. Grado (Gorizia), Italy, 1995.

[123] M. Cabrini, S. Maffi, and G. Razzini. “Evaluation of Hydrogen embrittlement behaviour by means of permeation current measurement in slow strain rate conditions of a micro-alloyed steel”. In: *Electrochemical Methods in Corrosion Research VI Pts 1 and 2*. Vol. 289-292. Materials Science Forum. Zurich-Uetikon: Transtec Publications LTD, 1998, pp. 1245–1256.

[124] John Tien et al. “Hydrogen transport by dislocations”. In: *Metallurgical and Materials Transactions A* 7.6 (1976), pp. 821–829.

[125] J. Svoboda, F. D. Fischer, and P. Fratzl. “Determination of trapping parameters and the chemical diffusion coefficient from hydrogen permeation experiments”. In: *Corrosion Science* 82 (2014), pp. 93–100. DOI: 10.1016/j.corsci.2013.12.018.

[126] P. Sofronis and R. McMeeking. “Numerical analysis of hydrogen transport near a blunting crack tip”. In: *J. Mech. Phys. Solids* 37.3 (1989), pp. 317–350.

[127] A. Krom et al. “The effect of strain rate on hydrogen distribution in round tensile specimens”. In: *Mater. Sci. Eng. A* 271.1-2 (1999), pp. 22–30.

[128] A. Krom and A. Bakker. “Hydrogen trapping models in steel”. In: *Metall. Mater. Trans. B* 31 (2000), pp. 1475–1482.

[129] A. Taha and P. Sofronis. “A micromechanics approach to the study of hydrogen transport and embrittlement”. In: *Eng. Fract. Mech.* 68.6 (2001), pp. 803–833.

[130] Y. Liang and P. Sofronis. “Toward a phenomenological description of hydrogen-induced decohesion at particle/matrix interfaces”. In: *J. Mech. Phys. Solids* 51 (2003), pp. 1509–1531.

[131] H. Kotake et al. “Transient hydrogen diffusion analyses coupled with crack-tip plasticity under cyclic loading”. In: *Int. J. Pressure Vessels Piping* 85.8 (2008), pp. 540–549.

[132] O. Aslan. “Numerical modeling of hydrogen diffusion in metals accounting for large deformations”. In: *Int. J. Hydrogen Energy* 40.44 (2015), pp. 15227–15235.

[133] A. Alvaro et al. “Hydrogen embrittlement susceptibility of a weld simulated X70 heat affected zone under H2 pressure”. In: *Materials Science and Engineering: A* 597 (2014), pp. 29–36.

[134] F. Bolzoni, M. Cabrini, and C. Spinelli. “Hydrogen diffusion and hydrogen embrittlement behaviour of two high strength pipeline steels”. In: *Proceedings of Eurocorr 2001*. Riva del Garda (Bs), Italy, 2001.

[135] G. Frankel and R. M. Latanision. “Hydrogen transport during deformation in nickel: Part I. Polycrystalline nickel”. In: *Metallurgical Transactions A* 17.5 (1986), pp. 861–867.

[136] M. Cabrini et al. “Hydrogen diffusion in low alloy steels under cyclic loading”. In: *Corrosion Reviews* (2019), 10.1515/corrrev-2019–0008.

[137] M. Cabrini et al. “Hydrogen permeation in X65 steel under cyclic loading”. In: *Corrosion Reviews* 13.10 (2020), art. 2309.

[138] H. Niazi et al. “High pH stress corrosion cracking initiation and crack evolution in buried steel pipelines: A review”. In: *Engineering Failure Analysis* (2021). DOI: 10.1016/j.engfailanal.2020.105013. URL: https://doi.org/10.1016/j.engfailanal.2020.105013.

[139] M. Cabrini et al. “Environmentally assisted cracking and hydrogen diffusion in traditional and high-strength pipeline steels”. In: *Corrosion Reviews* 33.6 (2015), pp. 529–545. DOI: 10.1515/corrrev-2015-0051. URL: https://doi.org/10.1515/corrrev-2015-0051.

[140] H. Nykyforchyn et al. “Pipeline durability and integrity issues at hydrogen transport via natural gas distribution network”. In: *Procedia Structural Integrity* 33 (2021), pp. 646–651.

[141] R. Zhang et al. “Effects of natural gas impurities on hydrogen embrittlement susceptibility and hydrogen permeation of X52 pipeline steel”. In: *Engineering Failure Analysis* 159 (2024), pp. 108–111.

[142] C.S. Zhou et al. “Hydrogen uptake induced by CO2 enhances hydrogen embrittlement of iron in hydrogen blended natural gas”. In: *Corrosion Science* 207 (2022), pp. 9879–9884.

[143] M.B. Djukic et al. “Hydrogen embrittlement of low carbon structural steel”. In: *Procedia Materials Science* 3 (2014), pp. 1167–1172.

[144] Y. Katz, N. Tymiak, and W. W. Gerberich. “Nanomechanical probes as new approaches to hydrogen/deformation interaction studies”. In: *Engineering Fracture Mechanics* 68 (2001), pp. 619–646.

[145] W. W. Gerberich, P. G. Marsh, and J. W. Hoehn. “Hydrogen induced cracking mechanisms – are there critical experiments?” In: *Hydrogen effects in materials*. Ed. by N. R. Moody and J. W. Hoehn. Warrendale, PA: TMS, 1996.

[146] D. F. Teter, I. M. Robertson, and H. K. Birnbaum. “The effects of hydrogen on the deformation and fracture of β-titanium”. In: *Acta Materialia* 49 (2001), pp. 4313–4320.

[147] R. A. Oriani and P. H. Josephic. “Equilibrium aspects of hydrogen-induced cracking of steels”. In: *Acta Metallurgica* 22.9 (1974), pp. 1065–1074.

[148] R. R. Fessler, T. P. Groeneveld, and A. R. Elsea. “Stress-Corrosion and Hydrogen-Stress Cracking in Buried Pipelines”. In: *Stress Corrosion Cracking and Hydrogen Embrittlement of Iron Base Alloys*. Ed. by R. W. Staehle et al. NACE-5. Houston, TX: NACE, 1977, p. 135.

[149] C. S. Carter and M. V. Hyatt. “Review of Stress Corrosion Cracking in Low Alloy Steels with Yield Strength Below 150 ksi”. In: *Stress Corrosion Cracking and Hydrogen Embrittlement of Iron Base Alloys*. Ed. by R. W. Staehle et al. NACE-5. Houston, TX: NACE, 1977, pp. 524–600.

[150] A. Punter, A. T. Fikkers, and G. Vanstaen. “Hydrogen-Induced Stress Corrosion Cracking on a Pipeline”. In: *Materials Performance* 31 (1992), pp. 24–28.

[151] M. Cabrini et al. “Unique HSC Scenario Leads to Gas Line Failure”. In: *Oil Gas J.* 6 (2000), pp. 61–65.

[152] L. Barsanti et al. “Hydrogen Embrittlement Resistance of X100 Steels for Long Distance High Pressure Pipelines”. In: *Environment-Induced Cracking of Materials - Prediction, Industrial Developments and Evaluation*. Ed. by S. Shipilov et al. Vol. 1. Oxford, UK: Elsevier, 2007, pp. 291–391.

[153] G. Demofonti et al. “Eni TAP Project mechanical damage and Environmental Assisted Cracking - Full scale methodology overview”. In: *Proceedings of the International Conference on New Developments on Metallurgy and Applications of High Strength Steels*. CD-ROM. Buenos Aires, 2008.

[154] R.N. Parkins and S. Zhou. “The stress corrosion cracking of C-Mn steel in CO2-HCO3-CO32- solutions. II: Electrochemical and other data”. In: *Corros Sci* 39 (1997), pp. 175–191. DOI: 10.1016/S0010-938X(97)89248-7.

[155] L.B. Peral et al. “Hydrogen uptake and diffusion kinetics in a quenched and tempered low carbon steel: experimental and numerical study”. In: *Int J Hydrogen Energy* 48 (2023), pp. 35347–35365. DOI: 10.1016/j.ijhydene.2023.05.286.

[156] S. Trasatti. “ELECTROCHEMICAL THEORY | Hydrogen Evolution”. In: *Encyclopedia of Electrochemical Power Sources*. Elsevier, 2009.

[157] L. Gritti et al. “Data-driven optimisation of variation of residual concentration to estimate the hydrogen diffusion coefficient and uptake via MATLAB”. In: *Data in Brief - International Journal of Hydrogen Energy* (2025). DOI: 10.1016/j.ijhydene.2025.02.400..

[158] A. Thomas and J.A. Szpunar. “Hydrogen diffusion and trapping in X70 pipeline steel”. In: *Int J Hydrogen Energy* 45 (2020), pp. 2390–2404. DOI: 10.1016/j.ijhydene.2019.11.096.

[159] C. Hurley et al. “Numerical modeling of thermal desorption mass spectroscopy (TDS) for the study of hydrogen diffusion and trapping interactions in metals”. In: *Int J Hydrogen Energy* 40 (2015), pp. 3402–3414. DOI: 10.1016/j.ijhydene.2015.01.001.

[160] E. Wallaert et al. “Thermal desorption spectroscopy evaluation of the hydrogen-trapping capacity of NbC and NbN precipitates”. In: *Metall Mater Trans A Phys Metall Mater Sci* 45 (2014), pp. 2412–2420. DOI: 10.1007/s11661-013-2181-1.

[161] Y.S. Chen et al. “Hydrogen trapping and embrittlement in metals – A review”. In: *Int J Hydrogen Energy* (2024). DOI: 10.1016/j.ijhydene.2024.04.076.

[162] E. Koren et al. “Hydrogen diffusivity in X65 pipeline steel: Desorption and permeation studies”. In: *Int J Hydrogen Energy* 61 (2024), pp. 1157–1169. DOI: 10.1016/j.ijhydene.2024.03.027.

[163] F. Vucko et al. “Palladium coating on quenched-tempered martensitic steel for hydrogen electrochemical permeation tests”. In: (). Accessed: 2025-11-20.

[164] M. A. V. Devanathan and Z. Stachurski. “The Mechanism of Hydrogen Evolution on Iron in Acid Solutions by Determination of Permeation Rates”. In: *Journal of The Electrochemical Society* 111 (1964), p. 619. DOI: 10.1149/1.2426195.

[165] L. Gritti et al. “A novel approach for estimating hydrogen uptake and diffusion coefficient”. In: *, Int J Hydrogen Energy* 112 (2025), pp. 347–353. DOI: 10.1016/j.ijhydene.2025.02.400..

[166] M. Devanathan and Z. Stachurski. “The adsorption and diffusion of electrolytic hydrogen in palladium”. In: *Proceedings of the Royal Society of London. Series A, Mathematical and Physical Sciences* 270 (1962), pp. 90–102.

[167] U. Hadam and T. Zakroczymski. “Absorption of hydrogen in tensile strained iron and high-carbon steel studied by electrochemical permeation and desorption techniques”. In: *International Journal of Hydrogen Energy* 34 (2009), pp. 2449–2459. DOI: 10.1016/j.ijhydene.2008.12.021.

[168] K. Okuno and K. Takai. “Determination of hydrogen diffusibility and embrittlement susceptibility of high-strength steel evaluated at different temperatures based on the local equilibrium theory”. In: *Acta Materialia* 246 (2023), p. 118725. DOI: 10.1016/j.actamat.2023.118725.

[169] K. Arhar et al. “Evaluation of Hydrogen Bubble Growth on a Platinum Microelectrode Under Varying Electrical Potential”. In: *Applied Sciences* 15 (2025), p. 4107. DOI: 10.3390/app15084107.

[170] A. Turnbull and M.K. Gardner. “Electrochemical polarization studies of BS 4360 50D steel in 3.5% NaCl”. In: (1982). Unpublished / Report.

[171] J. Srinivasan et al. “Electrochemical Polarization: I. A Theoretical Analysis of the Shape of Polarization Curves”. In: *Journal of The Electrochemical Society* 56 (1957).

[172] R.-H. Song, S.-I. Pyun, and R.A. Oriani. “The hydrogen permeation through passivating film on iron by modulation method”. In: *Electrochimica Acta* 36 (1991), pp. 825–831.

[173] J.C. Nelson and R.A. Oriani. “Current transients caused by potential jumps applied to passivating films on nickel”. In: *Electrochimica Acta* 35 (1990), pp. 1719–1726. DOI: 10.1016/0013-4686(90)87071-9.

[174] HC Ma et al. “Influence of iron oxides and calcareous deposits on the hydrogen permeation rate in X65 steel in a simulated groundwater”. In: *International Journal of Hydrogen Energy* 46.9 (2021), pp. 6669–6679.

[175] J. Yamabe, T. Awane, and S. Matsuoka. “Investigation of hydrogen transport behavior of various low-alloy steels with high-pressure hydrogen gas”. In: *International Journal of Hydrogen Energy* 40 (2015), pp. 11075–11086. DOI: 10.1016/j.ijhydene.2015.07.006.

[176] A.J. Kumnick and H.H. Johnson. “Steady state hydrogen transport through zone refined irons”. In: *Metallurgical Transactions A* 6 (1975), pp. 1087–1091. DOI: 10.1007/BF02661363.

[177] P. Manolatos, M. Jerome, and J. Galland. “Necessity of a palladium coating to ensure hydrogen oxidation during electrochemical permeation measurements on iron”. In: *Electrochimica Acta* 40 (1995), pp. 867–871.

[178] P. Castaño Rivera, V.P. Ramunni, and P. Bruzzoni. “Hydrogen trapping in an API 5L X60 steel”. In: *Corrosion Science* 54 (2012), pp. 106–118. DOI: 10.1016/j.corsci.2011.09.008.

[179] M. Enomoto, D. Hirakami, and T. Tarui. “Modeling Thermal Desorption Analysis of Hydrogen in Steel”. In: *ISIJ International* 46 (2006), pp. 1381–1387.

[180] A.J. Griffiths and A. Turnbull. “On the effective diffusivity of hydrogen in low alloy steels”. In: (1995). Unpublished / Report.

[181] A. Turnbull. “Hydrogen diffusion and trapping in metals”. In: *Gaseous Hydrogen Embrittlement of Materials in Energy Technologies*. Ed. by R.P. Gangloff and B.P. Somerday. Woodhead Publishing, 2012. Chap. 4, pp. 89–128.

[182] T. Zakroczymski. “Adaptation of the electrochemical permeation technique for studying entry, transport and trapping of hydrogen in metals”. In: *Electrochimica Acta* 51 (2006), pp. 2261–2266. DOI: 10.1016/j.electacta.2005.02.151.

[183] R. Wang. “Effects of hydrogen on the fracture toughness of a X70 pipeline steel”. In: *Corrosion Science* 51 (2009), pp. 2803–2810. DOI: 10.1016/J.CORSCI.2009.07.013.

[184] Marina Cabrini, Sergio Lorenzi, and Tommaso Pastore. “Cyclic voltammetry evaluation of inhibitors for localised corrosion in alkaline solutions”. In: *Electrochimica acta* 124 (2014), pp. 156–164.

[185] E. Akiyama and S. Li. “Electrochemical Hydrogen Permeation Tests under Conventional Potentiostatic Hydrogen Charging Conditions Conventionally Used for Hydrogen Embrittlement Study”. In: *ECS Transactions* 75 (2017), pp. 23–31. DOI: 10.1149/07529.0023ecst.

[186] Q. Liu et al. “Equivalent Hydrogen Fugacity during Electrochemical Charging of 980DP Steel Determined by Thermal Desorption Spectroscopy”. In: *Advanced Engineering Materials* 20 (2018). DOI: 10.1002/adem.201700469.

[187] J. Venezuela et al. “Equivalent hydrogen fugacity during electrochemical charging of some martensitic advanced high-strength steels”. In: *Corrosion Science* 127 (2017), pp. 45–58. DOI: 10.1016/j.corsci.2017.08.011.

[188] J. L. Crolet and G. Maisonneuve. “Construction of a universal scale of severity for hydrogen cracking”. In: (2000), NACE–00127.

[189] G. R. Murtagian, D. H. Johnson, and H. A. Ernst. “Dynamic crack propagation in steel line pipes. Part I: Experimental investigation”. In: *Engineering Fracture Mechanics* 72 (2005), pp. 2519–2534. DOI: 10.1016/j.engfracmech.2005.03.003.

[190] H. Reza Hajibagheri, A. Heidari, and R. Amini. “An experimental investigation of the nature of longitudinal cracks in oil and gas transmission pipelines”. In: *Journal of Alloys and Compounds* 741 (2018), pp. 1121–1129. DOI: 10.1016/j.jallcom.2017.12.311.

[191] J. R. Rice. “A Path Independent Integral and the Approximate Analysis of Strain Concentration by Notches and Cracks”. In: *Journal of Applied Mechanics* 35 (1968), pp. 379–386.

[192] JC Newman Jr, MA James, and U Zerbst. “A review of the CTOA/CTOD fracture criterion”. In: *Engineering Fracture Mechanics* 70.3-4 (2003), pp. 371–385.

[193] X-K. Zhu and J. A. Joyce. “Review of fracture toughness (G, K, J, CTOD, CTOA) testing and standardization”. In: *Engineering fracture mechanics* 85 (2012), pp. 1–46.

[194] A. Martinelli and S. Venzi. “Dependence of JIC, tearing modulus, CTOA, and total fracture energy on specimen dimension”. In: *Engineering Fracture Mechanics* 68.14 (2001), pp. 1575–1590.

[195] A. Martinelli and S. Venzi. “Tearing modulus, J-integral, CTOA and crack profile shape obtained from the load-displacement curve only”. In: *Engineering Fracture Mechanics* 53 (1996), pp. 263–277. DOI: 10.1016/0013-7944(95)00100-X.

[196] X. Feaugas and D. Delafosse. “Hydrogen and Crystal Defects Interactions: Effects on Plasticity and Fracture”. In: *Mechanics - Microstructure - Corrosion Coupling: Concepts, Experiments, Modeling and Cases*. Elsevier, 2019, pp. 199–222. DOI: 10.1016/B978-1-78548-309-7.50009-0.

[197] D. Guedes et al. “The Role of Plasticity and Hydrogen Flux in the Fracture of a Tempered Martensitic Steel: A New Design of Mechanical Test until Fracture to Separate the Influence of Mobile from Deeply Trapped Hydrogen”. In: *Acta Materialia* 186 (2020), pp. 133–148. DOI: 10.1016/j.actamat.2019.12.045.

[198] H. Yu et al. “Hydrogen Embrittlement as a Conspicuous Material Challenge: Comprehensive Review and Future Directions”. In: *Chemical Reviews* 124 (2024), pp. 6271–6392. DOI: 10.1021/acs.chemrev.3c00624.

[199] A Martinelli, E Monti, and S Venzi. “Relationship between J and a during whole crack propagation”. In: *Engineering fracture mechanics* 40.6 (1991), pp. 1165–1178.

[200] X. K. Zhu, P. S. Lam, and Y. J. Chao. “Constraint-dependent CTOA determination for stable ductile crack growth”. In: *Engineering Fracture Mechanics* 271 (2022), p. 108651. DOI: 10.1016/j.engfracmech.2022.108651.

Appendix A

Data-driven optimisation of hydrogen diffusion coefficient and uptake using MATLAB

This appendix presents the data collected during hydrogen uptake tests carried out at the University of Bergamo and the MATLAB code developed to estimate key hydrogen uptake parameters. The experimental approach involves two steps: electrochemical charging of the metallic sample via cathodic polarisation at potentials below the equilibrium potential for hydrogen evolution, followed by discharging under anodic polarisation at potentials above the equilibrium potential.

During discharging, the time-dependent anodic current reflects the flux of diffusible hydrogen leaving the sample, which depends on the initial hydrogen concentration, the diffusion coefficient, and the time elapsed between charging and discharging.

Using a data-driven optimisation, the characteristic parameters of hydrogen diffusion (apparent diffusion coefficient, hydrogen uptake, and waiting time) can be obtained. While the current data assume a cylindrical geometry, the method can be adapted to other geometries via simulation.

A.1 Background

Thank this data it is possible elaborate directly the experimental data detected via method explained in Chapter 4 and [165]. The data driven optimisation code can be

employed to estimate the initial hydrogen concentration C_0, the diffusion coefficient D, and the time interval t_0 between the end of the charging phase and the start of the initial discharging phase based on experimental electrochemical discharging curves as explained in [165]. The experimental data should be normalized as described in [165] by assigning the appropriate values to C_0, D, and t_0. The normalized experimental data can be adjusted to align with the reference target curve by modifying the normalization parameters C_0, D, and t_0. Optimization is employed to minimize the relative error function, which is computed as the difference between the two curves. The procedure was implemented using MATLAB code. The experimental curves and MATLAB procedure is accessible on Mendeley Data [157]. The iterative process utilizes the *fminsearch* function, a nonlinear optimization solver based on the Nelder–Mead simplex algorithm. This method involves a simplex of n+1 points, ordered by the decreasing value of the objective function. The worst point is discarded and replaced by a new point according to specific criteria.

A.2 Experimental and calculation technique details

The experimental data were acquired following the procedure described in Chapter 4 and using the experimental apparatus also described in Chapter 4. The following provides some details on the calculation procedure.

A.2.1 Pre-processed data

To generate the pre-processed data, it was necessary following this protocol. It was estimated the net current due to hydrogen oxidation I_{adj}, the experimental value of the discharging current was depurated by subtracting the passivation current curve measured during the early phase (1)

$$I_{adj} = I - I_{pass} \tag{A.1}$$

where I is current measured during discharging step, while I_{pass} is current measured during passivation. The integral sum of this curve, over testing time, allows to estimate charge exchanged Q_{adj}. It was possible to evaluate the charge evolution over time $Q_{adj}(t_i)$ as follow in Equation (A.2)

$$Q_{adj} = \int_0^{end} I_{adj}\, dt \tag{A.2}$$

$$Q_{adj}(t_i) = \sum_{t=0}^{end} Q_{adj}(t_{i-1}) + \frac{\left(I_{adj}(t_i) + I_{adj}(t_{i+1})\right) \cdot (t_i - t_{i+1})}{2} \tag{A.3}$$

Therefore, the diffusible hydrogen concentration egress from the sample can be calculate as follow

$$C_{egress,\ adj}(t_i) = \frac{Q_{adj}(t_i) \cdot AW_H}{F \cdot m_{samp}} \cdot 10^6 \tag{A.4}$$

with AW_H is the atomic weight of hydrogen, F is Faraday's constant and m_{samp} is the mass of sample in grams. To estimate the average residual diffusible hydrogen concentration that remain into the sample $C_{res,\ \ adj}(t_i)$, considering a certain initial concentration at the end of charging, the following evaluation is necessary

$$C_{res,\ \ adj}(t_i) = C_{egress,\ adj}(t = end) - C_{egress,\ adj}(t_i) \qquad [ppm] \tag{A.5}$$

where $C_{egress,\ adj}(t = end)$ is the maximum final value of egress concentration and $C_{egress,\ adj}(t_i)$ is the egress concentration over time. The relative time t and the average residual diffusible hydrogen concentration $C_{egress,\ adj}$ are pre-processed data must be uploaded in the data-driven optimisation MATLABE code.

A.2.2 Target curve

The tri-dimensional diffusion of hydrogen from the sample during electrochemical discharge was simulated through the FEM model using *COMSOL Multiphysics* in cylindrical coordinates. The specific cylinder geometry of the sample adopted in this work was considered. The diffusion process in the metal is described by Fick's second law (A.6), where C e t are the hydrogen concentration and time, respectively.

$$\begin{cases} \dfrac{\partial C}{\partial t} - D\nabla^2 C = 0 \\ C_0^* = \text{constant}, \quad D = \text{constant} \quad \text{(I.C.)} \\ C_s = 0 \quad \text{on surfaces} \qquad\qquad \text{(B.C.)} \end{cases} \tag{A.6}$$

The model includes the initial conditions (*I.C.*) of homogeneous hydrogen concentration C_0^* and constant diffusion coefficient D. During discharging, the boundary condition (*B.C.*) on the metal–solution surface imposes the concentration C_s to be equal to zero. The simulations conducted varying diffusion coefficients D and initial concentrations C_0^*.

The flux of hydrogen leaving all sample surfaces is then obtained using Fick's first law (A.7), given the concentration gradient normal to the external sample surface.

$$\phi^*_{egress} = -D \cdot \nabla C \tag{A.7}$$

The mole of egress hydrogen ($n^*_{egress}(t)$) was obtained through the integration of the flux over time. Thus, to obtain the average residual concentration (C^*_{res}) that remains in the sample at a certain time, considering an initial concentration C^*_0 at the end of charging, the following evaluation is necessary (A.8):

$$C^*_{res}(t) = \sum_{t=0}^{\infty} \frac{n^*_{egress}(t=\infty) - n^*_{egress}(t)}{Volume} \qquad \left[\frac{mol}{m^3}\right] \tag{A.8}$$

About the simulation to discretise the geometry, the axisymmetric property of the problem was exploited. As a result, a mesh was generated over a single rectangular section, with one side aligned along the cylinder's axis. The mesh was automatically generated using a quadrilateral mesh generator, which primarily creates quadrilateral elements. However, in regions of the geometry where it deems necessary, the generator may also introduce triangular elements. In this specific case, the computational plane consisted of 1647 quadrilateral elements. The simulation solved a total of 2009 degrees of freedom, with an integration time step of 60000 seconds. It is important to note that the flux was applied over all surfaces. The simulation parameters can be modified depending on the intended application. The values presented here were used to analyse this specific geometry.

To obtain the target curve shown in the data, the results of simulated tests, time t^* and residual diffusion hydrogen concentration simulated $C^*_{res}(t)$ must be normalised as describe in [165] introducing the normalised time $\widehat{T}$ and normalised concentration $\widehat{C}^*(t)$ using Equations (A.9) and (A.10).

$$\widehat{C}^*(t) = \frac{C^*_{res}(t)}{C^*_{res}(t=0)} \equiv \frac{C^*_{res}(t)}{C^*_0} \tag{A.9}$$

$$\widehat{T} = \frac{t \cdot D}{r^2} \tag{A.10}$$

The diffusion coefficient D and initial hydrogen concentration C^*_0 are that imposed during the simulation, $\widehat{T}$ and $\widehat{C}^*(t)$ formed the target curve (that it is independent by D and C^*_0 as described in [165].

A.3 Data-driven optimisation Matlabe code

The code used to process the pre-processed data and the target curve to obtain the optimal values of D, C_0, and t_0 from the experimental data is as follows:

```
%% &&&&&&&&&&&&&&&&&&&&&&&&&&&&&&&&&&&&&&&&&&&&&&&&&&&&&&&&&&&&&&&&&&&&&&&& %%
%%                              Hyfit                                        %%
%                       SCRIPT TO ESTIMATE                                    %
%     INITIAL CONCENTRATION, DIFFUSION COEFFICENT and TIME                    %
%                        WITH AMODEL CURVE                                    %
%                          -by Luca Gritti-                                   %
%                            18-06-2024                                       %
%% &&&&&&&&&&&&&&&&&&&&&&&&&&&&&&&&&&&&&&&&&&&&&&&&&&&&&&&&&&&&&&&&&&&&&&&& %%

%% INFO: the script used 'fminsearch' to optimise the parmaeters D and C0
%% Explanation of the code:
% 1) Data
%     Fix the time to start the test (t0), radious of sample and error
    stopped
% 2) IMPORT MATRIX DataIN
%     Import and display experimental data.
% 3) CURVE MODEL
%     Import automatically data od model curve.
% 4)SCRIPT
%     4.1)Estimation of initial parametrers
%         Estimate automatically initial parameters D and C0 to first
    iteration.
%     4.2) (A) Mnimisation of ERRtotnorm
%           Use 'fminsearch' to find optimal D and C0 values that minimize
    ERRtotnorm with t0.
%     4.3) (B) Mnimisation of ERRtotnorm
%           Use 'fminsearch' to find optimal t0 that minimize ERRtotnorm
    with D and C0 previously optimise.
%     4.2) (C) Mnimisation of ERRtotnorm
%           Use 'fminsearch' to find optimal D and C0 values to second time
     that minimize ERRtotnorm with t0 optimised.

%  5) Graphical representation of results with optimized parameters and
%     displays results with optimized parameters
%  6) Function to calculate ERRtotnorm implemented in 'fminsearch'

% This approach allows to optimize the parameters D, C0 and t0 in order to
     minimize
% ERRtotnorm, changing the tolerance as needed by optimset.

%% ------------------------------------------------------------ %%

clc
clear all
```

```
close all

%% Data
t0 = 0.1; % s  <--Waiting time between Charge and Dscharge
R = 0.0065; % m <--Radious of sample (or caracteristic length)

ERRstopped=0.4; %[] <-- The parameter is estimated by comparing the
    normalized model curves. Corresponds to the maximum normalized time
    that ensures complete overlap of the model curves.

%% IMPORT MATRIX DataIN
%Change the address of the %addpath  function by updating it with the
    one
%where the       DataInBrief_Hydrogen_discharging       folder was added

%Find the current script folder (automatically)
fullScriptPath = mfilename('fullpath');
mainFolder = fileparts(fullScriptPath);
addpath(genpath(mainFolder)); %add the path to general folder

[filename, path] = uigetfile('*.*', 'Selecte the experimental data file to
     import');
% if you do not want to click on the file to select, you can add the
% following instructions and cooment with %  the previous line
% filename='name:of:file_to_import.txt';

address=string(strcat(mainFolder,'\Preprocessed data\',filename));%create
    a string to import data

DataIN = importfile(address, [4, Inf]);
%DataIN=[relative time (s)| Residual concetration (ppm)]
%Don't change the name of 'DataIn'; Update the address of 'importfile'
    function

%% CURVE MODEL: import target curve
%-------------------------------------------
ModelNorm=importdata ('Target_curve.txt');
Tmodel = ModelNorm.data(:,1);
Cmodel = ModelNorm.data(:,2);
%-------------------------------------------

%% SCRIPT
%% Estimation of initial parametrers C0 and D
C0_init =DataIN(1,2)+t0*1.5; % ppm

s=find(DataIN(:,2)<DataIN(1,2)/3,1,'first'); %row where the first measured
     concentration becomes a third
D_init=((DataIN(s,1)*t0)*(R^2))/((DataIN(s,1)+t0)*10^10);%m2/s

%% (A) Minimisation of ERRtotnorm on D and C0
options = optimset('TolFun', 1e-12, 'TolX', 1e-6,'MaxFunEvals',1500); %
    Imposta la tolleranza
params_init = [D_init, C0_init];
```

```
84 params_opt = fminsearch(@(params) calculate_ERRtotnorm(params, DataIN,
       Tmodel, Cmodel, t0, R, ERRstopped), params_init, options);
85
86 D_opt = params_opt(1);
87 C0_opt = params_opt(2);
88
89 %% (B) Minimisation of ERRtotnorm on t0 and usind D_opt and C0_opt
90 optionsB = optimset('TolFun', 1e-10, 'TolX', 1e-6,'MaxFunEvals',1500); %
       Update the tolerance
91 params_init_time = [t0];
92 params_optB = fminsearch(@(params) calculate_ERRtotnormTIME(params, DataIN
       , Tmodel, Cmodel,D_opt, C0_opt, R, ERRstopped), params_init_time,
       optionsB);
93
94 t0_opt = params_optB(1);
95
96 %% (C) Minimisation of ERRtotnorm on D and C0 with t0_opt
97 options = optimset('TolFun', 1e-12, 'TolX', 1e-6,'MaxFunEvals',1500); %
       Update the tolerance
98 params_init2 = [D_opt, C0_opt];
99 params_opt2 = fminsearch(@(params) calculate_ERRtotnorm(params, DataIN,
       Tmodel, Cmodel, t0_opt, R, ERRstopped), params_init2, options);
100
101 D_opt2 = params_opt2(1);
102 C0_opt2 = params_opt2(2);
103
104 disp(['Name:', filename]);
105 fprintf('t0 optimised: %.6e\n', t0_opt);
106 fprintf('D optimised: %.6e\n', D_opt2);
107 fprintf('C0 optimised: %.6f\n', C0_opt2);
108
109
110 %% Graphical representation of results with optimized parameters
111
112 Data=[DataIN(:,1)+t0_opt, DataIN(:,2)];
113
114 Tnorm_opt = (Data(:,1) * D_opt2) / (R^2);
115 line_stop=find (Tnorm_opt<ERRstopped,1,'last');
116 Cinterp_norm_opt = interp1(Tmodel, Cmodel, Tnorm_opt);
117
118 figure
119 subplot (1,2,1)
120 plot(Tmodel, Cmodel, '-.m','linewidth',1.5, 'DisplayName', 'Normalise
       Model')
121 hold on
122 plot(Tnorm_opt, Cinterp_norm_opt, '.k', 'DisplayName', 'Optimized
       interpolation normalized')
123 hold on
124 plot([Tnorm_opt(1),Tnorm_opt(find (Tnorm_opt<ERRstopped,1,'last')) ], [
       Cinterp_norm_opt(1),Cinterp_norm_opt(find (Tnorm_opt<ERRstopped,1,'
       last')) ], 'g+','linewidth',1,'MarkerSize',15,'DisplayName', 'stopped
        to calculate error')
125
```

```
xlabel('Normalised Time  $\hat{T}=\frac{D \cdot t}{radius^2}$ [-]','Interpreter','Latex')
ylabel('Normalised Concetration $\hat{C}=\frac{C}{C0}$ [-]','Interpreter','Latex')
legend show
hold off

subplot(1,2,2)
plot(Data(:,1), Data(:,2), 'xb','MarkerSize',5, 'DisplayName', 'Experimental Data')
hold on
plot( Tnorm_opt(1:line_stop)*(R^2)/D_opt2, Cinterp_norm_opt(1:line_stop)*C0_opt2 ,'-r','linewidth',2, 'DisplayName', 'Fitting interpolant curve')
hold on
plot( [Tnorm_opt(1)*(R^2)/D_opt2, Tnorm_opt(find (Tnorm_opt<ERRstopped,1,'last'))*(R^2)/D_opt2 ], [Cinterp_norm_opt(1)*C0_opt2, Cinterp_norm_opt(find (Tnorm_opt<ERRstopped,1,'last'))*C0_opt2 ] ,'g+','linewidth',1,'MarkerSize',15,'DisplayName', 'stopped to calculate error')
hold on
plot( 0, C0_opt2 ,'p', 'MarkerSize',10,'MarkerEdgeColor','r','MarkerFaceColor','r', 'DisplayName', 'C0 estimated')
hold on
plot( [0, Tnorm_opt(1)*(R^2)/D_opt2 ], [C0_opt2,Cinterp_norm_opt(1)*C0_opt2 ] , '--r','linewidth',1, 'DisplayName','lost in waiting time' )


xlabel('Time [s]','Interpreter','Latex')
ylabel('Concetration [ppm]','Interpreter','Latex')
legend show

format short
text( Data(end,1)-0.3*Data(end,1), 2/3*C0_opt2, 'Results of Fitting','FontSize',10,'FontWeight','bold')
text (Data(end,1)-0.3*Data(end,1), 2/3*C0_opt2-0.1*2/3*C0_opt2, strcat('t_o_p_t=',num2str(round(t0_opt,2)),' s'),'FontSize',9)
text (Data(end,1)-0.3*Data(end,1), 2/3*C0_opt2-0.2*2/3*C0_opt2, strcat('D_o_p_t=',num2str(D_opt2),' m^2/s'),'FontSize',9)
text (Data(end,1)-0.3*Data(end,1), 2/3*C0_opt2-0.3*2/3*C0_opt2, strcat('C0_o_p_t=',num2str(round(C0_opt2,2)),' ppm'),'FontSize',9)

hold off

%% Function to calculate ERRtotnorm
function err = calculate_ERRtotnorm(params, DataIN, Tmodel, Cmodel, t0, raggio,ERRstopped)
    D = params(1);
    C0 = params(2);

    Data = [DataIN(:,1) + t0, DataIN(:,2)]; % Time spostato |C depurata della passivit
    Tnorm = (Data(:,1) * D) / (raggio^2);
```

```
162     Cinterp_norm = interp1(Tmodel, Cmodel, Tnorm);
163     error_calc_line=find (Tnorm<ERRstopped,1,'last');
164     ERRnorm = abs( (Data(1:error_calc_line,2)/C0) - Cinterp_norm(1:
            error_calc_line)) ./ Cinterp_norm(1:error_calc_line);
165     err = sum(ERRnorm);
166 end
167
168 function err_time = calculate_ERRtotnormTIME(params, DataIN, Tmodel,
        Cmodel,D, C0, raggio, ERRstopped)
169     t0 = params(1);
170
171     DataNew = [DataIN(:,1) + t0, DataIN(:,2)]; % Time spostato |C depurata
            della passivit
172     Tnorm = (DataNew(:,1) * D) / (raggio^2);
173     Cinterp_norm = interp1(Tmodel, Cmodel, Tnorm);
174     error_calc_line=find (Tnorm<ERRstopped,1,'last');
175     ERRnorm = abs( (DataNew(1:error_calc_line,2)/C0) - Cinterp_norm(1:
            error_calc_line)) ./ Cinterp_norm(1:error_calc_line);
176     err_time = sum(ERRnorm);
177 end
```

Listing A.1: Codice MATLAB di esempio

A.4 Limitations

In the realisation of the experimental apparatus, it is necessary to ensure a homogeneous distribution of the current field on the specimen during the electrochemical charging and discharging phases in order to guarantee the axial-symmetry and homogeneity conditions imposed in the model assumptions.

There are no particular limitations with regard to the theoretical data of the simulations. In order to obtain a good target curve, it is necessary to create adequate discretisation of the geometry to be simulated so as to have low residuals at the end of the simulation

Appendix B

J integral with DCPD approach–Matlab code

```matlab
%% &&&&&&&&&&&&&&&&&&&&&&&&&&&&&&&&&&&&&&&&&&&&&&&&&&&&&&&&&& %%
% %%             J INTEGRAL with DCPD APPROACH                %%
% %%    via mechanical fracture tests on C(T) specimens       %%
% %%           according to standard ASTM E 1820-21           %%
% %%                      (by Lke)                            %%
% %                      25-06-2025                           %%
%% &&&&&&&&&&&&&&&&&&&&&&&&&&&&&&&&&&&&&&&&&&&&&&&&&&&&&&&&&& %%

clear all
close all
clc

%% IMPORT MATRIX DataEXP-> you have need to build: DataEXP=[time(s)|displacement(mm)|force(N)|DCPD(V)]
% %Find the current script folder (automatically)
fullScriptPath = mfilename('fullpath');
mainFolder = fileparts(fullScriptPath);
addpath(genpath(mainFolder)); %add the path to general folder

[filename, path] = uigetfile('*.*', 'Selecte the experimental data file to import');
% if you do not want to click on the file to select, you can add the
% following instructions and cooment with %  the previous line
% filename='test5.txt';
address=string(strcat(mainFolder,'\Dati\',filename));%create a string to import data
DataExp = importfile3(address, [2, Inf]);
% DataExp=[DataExp(:,1),DataExp(:,2),DataExp(:,3),DataExp(:,11)]; %[Displcement[mm]|Dissplacement(mm)||Force(N)|DCPD(V)]

% addpath 'C:\Users\utente\Desktop\C(T)_UniBg_DCPD_GAS\Elab_Jint\function'
```

```
% addpath 'C:\Users\utente\Desktop\C(T)_UniBg_DCPD_GAS\Elab_Jint\dati'
                                                    %20000
% DataExp = importfile3("C:\Users\utente\Desktop\C(T)_UniBg_DCPD_GAS\
    Elab_Jint\Dati\CT_UniBg_150bar_2.dat", [2, Inf]);

% Aritmetic Average of results%%%%%%%%%%%%%%%%%%%%%%%%%%%%%%%%%%%%
med=50;%ogni quanto medio 110 %500

DataExp=DataExp(1: length(DataExp)-rem(length(DataExp),med),:);
n=0;%count

for i=1:med:length(DataExp)-1
    n=n+1;
     %media dei dati sperimentali
     Time(n) =mean( DataExp  (  (i:(i+med)-1),1  )   );
     DAT(n,1)=mean( DataExp  (  (i:(i+med)-1),2  )   );
     DAT(n,2)=mean( DataExp  (  (i:(i+med)-1),3  )   );
     DAT(n,3)=mean( DataExp  (  (i:(i+med)-1),4  )   );

     %estimation delta time (excel)
     if n>1
     Delta_time(n)= Time(n)-Time(1);
     end

end
DataExp=[];
DataExp=[DAT(:,1),DAT(:,3),DAT(:,2)]; %[Displcement[mm]|DCPD(V)|Force(N)]

figure
subplot(2,1,1)
plot(DataExp(:,1),DataExp(:,3));
xlabel('Displacement [mm]')
ylabel('Force (N)')
subplot(2,1,2)
plot(DataExp(:,2),DataExp(:,3));
xlabel('DCPD [V]')
ylabel('Force (N)')

%% DATA TO CUSTOMISE

Tol=1; %tolerance for take more or less points in the line fitting
       %if you use Tol=1 the program only takes points within the segment
            (maybe not all)

y= 10*2/3; %mm >> half distance between  the voltage measurements points (
    e.g. 2y=W/3) pg 57

P_top=5000; %[N] ----->range of values to estimate the linear elastic
P_bottom=3500; %[N]    portion of the force-displacement curve"
%-----------------------------------------------------------------
% GEOMETRICAL AND MATERIAL DATA
W=20; %mm
B=10; %mm
BN=10; %mm
```

```
78
79  E=210000; %MPa
80  nu=0.28; %Poisson
81  sigma_ys=430; %MPa
82  sigma_tr=565; %Mpa
83
84  %Crack measurments (experimental)
85  a_precrak=9.48; %mm %hp
86  ain_meas=9.48;
87  afin_meas=12.21;
88
89  %% ------------------------------------------------------------%%
90  %%                      <=    CODE    =>                       %%
91  %% ------------------------------------------------------------%%
92
93  %% ESTIMATION V_el and V0
94  [V_el,P_Vel,line_Vel,V0,Poly] = DCPD_estimating1(DataExp(:,2),DataExp(:,3)
        ,Tol); %V= stimato sul95% del P max          %V= stimato sul P_Vel <-
        questo
95  %% Relation between DCPD and crack size a
96
97  %Blunting correction
98  a0=a_precrak;
99  sigma_Y=(sigma_ys+sigma_tr)/2; %Mpa
100
101 %per V<=V_el --> linear elastic branch
102 for i=1:line_Vel %linear elastic branch
103     U=a0/W; %parameter
104     fforma= ( (2+U) * (0.886+4.64*U-13.32*U^2+14.72*U^3-5.6*U^4) ) / ((1-U
            )^(3/2));
105     K_el(i)=DataExp(i,3)/((B*BN*W)^0.5) * fforma; %MPa*(mm)^0.5
106     J_el(i)=(K_el(i)^2*(1-nu))/E; % (MPa*mm)==(kJ/m2)
107     a(i)=a0+J_el(i)/(2*sigma_Y); %mm
108 end
109
110 a0_bl= a(end);
111
112 %per V>V_el --> elastic-plastic branch
113 for i=(line_Vel+1):length (DataExp(:,2))
114
115    % %formula 1
116     num(i)= cosh((pi*y)/(2*W));
117     denom(i)= cosh(  (DataExp(i,2)/V0)*acosh(  (cosh((pi*y)/(2*W))) / (cos
            ((pi*a0_bl)/(2*W)))  )       );
118     a(i)= ( (2/pi)*acos( num(i)/denom(i) ) ) *W;
119
120 % % %formula2 prevista da normativa
121 % % A0=0.5766;
122 % % A1=1.9169;
123 % % A2=-1.0712;
124 % % A3=1.6898;
125 % %
126 % % Vseg=V0/( A0+A1*(a0_bl/W)+A2*(a0_bl/W)^2+A3*(a0_bl/W)^3);
127 % %
```

```
% % R=[];
% % R=DataExp(i,2)/Vseg;
% % a(i)=W*( -0.5051+0.8857*R-0.1398*R^2+0.0002398*R^3 );

% % %formula3 andrebbero calcolati tanti v segnati diversi ma non si sa
    come
% % Vsig=V0/(3.4916*((a0_bl/W)^2.8523)+0.5);
% % a(i)=W*( 0.2864*( (DataExp(i,2)/Vsig)-0.5) )^0.3506;


end

figure
plot(a,DataExp(:,3),'-o')
hold on
plot(a0_bl,DataExp(line_Vel,3),'X','MarkerSize', 10, 'LineWidth', 2)
xlabel('a (mm)')
ylabel('Force (N)')
legend ('first estimation of a', 'a0 blunting')


%% A adjusted (for V>Vo o V> V_el)

for i=(line_Vel+1):length(a)
  a_correct(i-(line_Vel))= ( (afin_meas-a0_bl)/(a(end)-a0_bl) )*(a(i)-
      a0_bl)+a0_bl;
end

a_adj=[a(1:line_Vel), a_correct];

hold on
plot (a_adj(1:line_Vel),DataExp((1:line_Vel),3),'-r')
plot (a_adj(line_Vel:end),DataExp((line_Vel:end),3),'-or')
legend ('first estimation of a', 'a0 blunting','second estimation a_a_d_j'
    )


figure
plot (a,DataExp(:,1),'-o')
hold on
plot (a_adj(1:line_Vel),DataExp((1:line_Vel),1),'-r')
hold on
plot (a_adj(line_Vel:end),DataExp((line_Vel:end),1),'-or')

xlabel('a(mm)')
ylabel('Dispalcement (mm)')
legend ('first estimation of a', 'a0 blunting','second estimation a_a_d_j'
    )

Data_adj=[DataExp(:,:),a_adj']; % [Displacement|DCPD|Force|a_adj]
                                % [    mm      | V |  N  | mm  ]

%% ----------------------------
%% ESTIMATION OF K AND J
```

```
%% ----------------------------

%Estimation of K
[K] = K_a_solver_B_DCPD(B,BN,W,Data_adj(:,3),a_adj); % K=[MPa*(mm^0.5)]

%Estimation of J_elastic, J_plastic and J_total
[J_el,J_pl, J, Delta_a_adj, A_pl,eta_pl, gamma] = Jsolver_B_DCPD1(P_top,
    P_bottom, line_Vel, Data_adj(:,1), W, BN, nu, E, Poly, K, Data_adj
    (:,2), Data_adj(:,3), a_adj, a_adj(1), B);

figure
plot (Delta_a_adj,K*(1000^0.5),'-s')
xlabel('Delta a adj [mm]')
ylabel('K [MPa*radq(m)')

figure
plot(Delta_a_adj,J,'-x')
xlabel('Delta a adj [mm]')
ylabel('J [kJ/m2]')

%% ----------------------------
% ESTIMATION OF JQ
%% ----------------------------

%Calcolo JQ corr ( A  9.6.1 e ss ad interim)
Jlim=(W-a(1))*sigma_Y/7.5;
[JQ,xout,yfit,C2] = JfitJQ3_DCPD(Delta_a_adj,J,Jlim, sigma_Y); %stampa
    anche un grafico


% SUMMARY
if isnan(JQ)==1 && isnan(xout)==1 && isnan(yfit)==1
else

RIS=[(1:length(Data_adj(:,1)))',Delta_time',Data_adj(:,1),Data_adj(:,2),
    Data_adj(:,3), A_pl', eta_pl', gamma', a', a_adj', Delta_a_adj', K',
    J_el', J_pl', J'];
RIS_tab= table ((1:length(Data_adj(:,1)))',Delta_time',Data_adj(:,1),
    Data_adj(:,2),Data_adj(:,3), A_pl', eta_pl', gamma', a', a_adj',
    Delta_a_adj', K', J_el', J_pl', J', ...
            'VariableNames',{'Event','Delta time [s]','Displacement [mm]',
                'Signal [mV]','Load [N]','A_pl','eta_pl','gamma', 'a [mm]
                ','a_adj [mm]' 'Delta a_adj [mm]','K','J elastico' ,'J
                plastico','J totale'})
end
```

Listing B.1: Codice MATLAB di esempio

Functions

Estimation of DCPD parameters

```
1
2     function [V_el,F_Vel,line_Vel,V0,Poly] = DCPD_estimating1(Signal,Force
          ,Tol)
3 % DCPD_estimating >>> Stima dei parmetri Vel e V0 e grafici
4 %
5 % INPUT => Signal: segnale DCPD
6 %           Force: Forza misurata
7 %           TOL: numero per modificare tolleranza per prendere punti che
8 %           bene approssimano la retta stimata dai dati nel segmetno
9 %           selezionato
10 %
11 % OUTPUT =>V_el: potenziale associato al compoartmanto elastico (primo
      distacco)
12 %           F_Vel: forza corrispondente a V elastico
13 %           line_Vel: riga del valore di V elastico
14 %           V_0: potenziale da usare per stima di crack growth (pg 53 ASTM
      1820-21)
15 %           P: vttore che contiene il fitting della retta F=m*DCPD+q -->P=
      [m|q]
16 %-------------------------------------------------------------
17 %INFO >>> La function esegue:
18 %            1) Selezione del tratto dove stimare V0 e Vel -tratto lineare
19 %            2) Fitting della retta che passa per i punti del segmento
20 %            3) STIMA LINEARIT  DEI PUNTI (tolleranza Toll)
21 %               (verifico se posso ampliare i punti da considerare nella
      retta al di fuori del segmetno preso)
22 %            4) Stima dei parmetri Vel e V0
23
24 %%                          CODICE
      %%
25 %% Matrice di lavoro
26 Data=[Signal, Force];
27
28 %% Selezione del tratto dove stimare V0 e Vel -tratto lineare
29
30 x=Data(:,1); %scrivo due vettori per invididuare i punti
31 y=Data(:,2);
32
33 [pos, xk, yk] = select_two_points_on_curve(x,y); %funzione per selezionare
       due punti dai dati sperimentali
34
35 figure
36 plot(Data(:,1), Data(:,2), '-*');
37 title('Selected segment of the LINEAR signal to analyze');
38 xlabel('DCPD potential (V)'); ylabel('Force (N)');
39 hold on
40 plot(xk, yk, 'ro', 'MarkerSize', 10, 'LineWidth', 2);
41
42 %% Fitting della retta che passa per i punti del segmento
43 pos=sort(pos);
44
45 for i=1:length (x)
46     if i>=pos(1) && i<=pos(2)
47         fitdata(i-(pos(1)-1),:)=Data(i,:);
```

```
    end
end

hold on
plot (fitdata(:,1), fitdata(:,2),'-*r')

Poly = polyfit( fitdata(:,1), fitdata(:,2),1); % coeff. m e q della retta

yfit = polyval(Poly,Data(:,1));

% rappresenzazione grafica dela retta-punti per disegnare la retta di
    fitting
hold on;
A2=0;
B2=max(Data(:,2))+max(Data(:,2))*0.4;
A1=(A2-Poly(2))/(Poly(1));
B1=(B2-Poly(2))/(Poly(1));

plot( [A1,B1], [A2, B2],'g--');
eqn = string(" Linear: y = " + Poly(1)) + "x + " + string(Poly(2));
text( (Data(pos(1),1)+Data(pos(2),1))/2, (Data(pos(1),2)+Data(pos(2),2))
    /2, eqn,"HorizontalAlignment","left","VerticalAlignment","top")

%% Stima dei parmetri Vel e V0

[xk] = sort(xk); %numeri e posizione
% Stima V_el
V_el=xk(2); %massimo dei punti considerati vicini alla retta


% F_Vel=y_closest(yy);
line_Vel=find(x<V_el,1,'last');
F_Vel=Data( line_Vel,2);
% line_Vel=find(V_el==Data(:,1)); %riga a cui corrisponde il valore di Vel
     nella matrice dati sperimentali

hold on
plot (V_el,F_Vel,'sm','MarkerSize',10, 'LineWidth',2)

%V0 stima
V0=(F_Vel-Poly(2))/Poly(1); %+(F_Vel-Poly(2))/Poly(1)*0.01;%stimato con F
    di V_el
%V0=( (max(Data(:,2))*0.95)-Poly(2))/Poly(1) %stimato con 95% di F max
    PROBLEMI NELLA STIM DELLA A

F_V0=Poly(1)*V0+Poly(2);

hold on
plot(V0,F_V0,'pk', 'MarkerSize',10, 'LineWidth',2)

%legend('experiemtnalt data','clic data','','','data considered to fit','
    line relation','points linearised','V_e_l_a_s_t_i_c','V_0');
legend('experimental data','clic data','','linear relation','V_e_l','V0');

```

```
96 end
```

Listing B.2: Codice MATLAB di esempio

Estimation of K

```
1     function [K] = K_a_solver_B_DCPD(B,BN,W,P,a_crack)
2 % K_a_solver >>> calcola il K e la compliance corretta metodo basic con
      DCPD
3 %
4 % INPUT => W, D, Hstar B, BN, Be,E   dati geometrici e di materiale
5 %           P: carico del ciclo -i
6 %           v: spostamento al ciclo -i
7 %           C_LL: compliance sperimentale
8 %           a: lunghezza della cricca
9 %
10 % OUTPUT =>v_pl: spostamento plastico stimato come differenza fra il toale
       e l'elastico
11 %                 che    stimato con la C_ll e P
12 %           b: ligament
13 %           v: spostamento al ciclo -i
14 %           aout: lunghezza della cricca calcolata con la C_LLc
15 %           C_LLc: compliance corretta con rotazione
16
17
18 for i=1:length(a_crack)
19
20     % 4 - Fattore intensificazione sforzi
21     U=a_crack(i)/W; %parametro
22     fforma= ( (2+U) * (0.886+4.64*U-13.32*U^2+14.72*U^3-5.6*U^4) ) / ((1-U
           )^(3/2));
23
24     K(i)=P(i)/((B*BN*W)^0.5) * fforma;
25
26 end
27
28 end
```

Listing B.3: Codice MATLAB di esempio

Fitting J curve

```
1
2 function [JQ,xout,yfit,C2] = JfitJQ3_DCPD(X,Y,Jlim, sigma_Y)
3 % JfitJQ3 => fitta i valori di Delta_a vs J per stimare il JQ
4 %          => rappresentazione grafica dei risultati e delle aree di
5 %              validit  dei punti da prendere per il fitting
6 %        =>=>IMP: utilizzo delle sotto funzioni per fare il fitting (
      FitJinRegionAB).
7 %               necessario vedere dove cadono e quanti sono i punti nelle
```

```
%            regioni A e B (ASTM 1820  A9 .6.4 e ss.) <=<=
%
% INPUT => X: valori sperimentali su asse x (=delta a(i))
%          Y: valori sperimentali su asse y (=J(i))
%          Jlim valore di Jlimite superiore
%          sigma_Y: sigma calcolato prima (media artimetica fra rottura e
%                   snervamento)
%
% OUTPUT => JQ: valore di JQ stimato dalla regressione con il fitting
%           xout: valori di Delta_a che cadono nella regione di
    qualificated Data*
%           yfit: valori di J fittati che cadono nella regione di
    qualificated Data*
%----------------------------------------
% (*) definita secondo norma, il fitting    fatto secondo la norma
%     norma di riferimeto ASTM E1820-21 [ A9 .6 pg 27-28]


%% COSTRUZIONE DELLE RETTE E NUMEROSIT  DEI PUNTI
% Individuo i punti che stanno fra le due rette (offset 0.15 e 1.5 di
% costruction line) con metodo dei punti che stanno sotto la prima retta e
     sopra
% la seconda retta

N=length(Y); %numero di cili

%Definisco le linee di costruzione per delimitare la regione di
%qualificazione dei dati (due rette oblique e retta orizzontale)

%Costruction Line "base" => servono per plottare le altre
X0=[0,X(N)]; %coord Costruction line da norma passa per zero
Y0=[2*sigma_Y*0, 2*sigma_Y*X(N)]; %coord Costruction line da norma passa
    per zero

%Construction Line traslata di 0.15
X1=[0+0.15; X(N)+0.15]; %coord x spostate di 0.15 (da norma) della 1
    retta di esclusione X==delta a
Y1=[0, 2*sigma_Y*X(N)]; %coord y della  1   retta di esclusione Y== J
                                    % le coordinate del valore della y
                                    % sono date dalla Costruntion Line da
                                    % norma

%Construction Line traslata di 0.2 (per fittare ilvalore di JQ con
%                                  regressione del fitting)
X3=[0+0.2;X(N)+0.2]; %coord x spostate di0.2 (da norma) della 1   retta di
     esclusione X==delta a
Y3=[0, 2*sigma_Y*X(N)]; %coord y della  1   retta di esclusione Y== J
                                    % le coordinate del valore della y
                                    % sono date dalla Costruntion Line da
                                    % norma

%Construction Line traslata di 1.5
X2=[0+1.5;X(N)+1.5]; %coord x spostate di 1.5 (da norma) della 2   retta
    di esclusione
```

```
Y2=[0, 2*sigma_Y*X(N)];%coord  della 2   retta di esclusione

%Construction Line traslata di 0.5 Line for region A and B
X4=[0+0.5;X(N)+0.5]; %coord x spostate di 1.5 (da norma) della 2   retta
    di esclusione
Y4=[0, 2*sigma_Y*X(N)];%coord  della 2   retta di esclusione

%Linea orizzontale superiore di Jlimite
SUP=[0,Jlim;
     X(N),Jlim]; %coord della retta orizzontaledi Jlim superiore


%Controllo che i valori di J sperimentali cadano fra le due rette oblique
    e
%sotto la retta orizzontale e butto gli altri valori (il fitting viene
%fatto solo su quelli)

for i=1:length(X)

   if Y(i)<Jlim %sotto retta orizzontale

          if Y(i)<2*sigma_Y*(X(i)-0.15) && Y(i)>2*sigma_Y*(X(i)-1.5) %fra
               rette oblique
                xoo(i)=X(i); %riporto il valore di Delta_a
                yoo(i)=Y(i); %riporto il valore di J
          else
                xoo(i)=NaN; %lascio NaN
                yoo(i)=NaN; %lascio NaN
          end

   else
     xoo(i)=NaN; %lascio NaN
     yoo(i)=NaN; %lascio NaN
   end

end

%tolgo i NaN
xout=xoo(~isnan(xoo)); %Delta_a che cadono fra le due retta e sotto la
    orizzontale Jlim
yout=yoo(~isnan(yoo)); %J che cadono fra le due retta e sotto la
    orizzontale Jlim

%VERIFICA DELLA NUMEROSIT  DEI PUNTI NELLE REGIONI
%Verifico che ci sia almeno un punto nella A region e nella B region (A
%region fra 0.15 e 0.5 lines e B region fra 0.5 e 1.5 lines)
% La retta passante per 0.5 ha eq. y=2*sigma_Y*(x-0.5)

NumA=0; %contatore numeri in A region
NumB=0; %contatore numeri in B region
Num0205=0; %contatore numeri fra lelinne di 0.2 e 0.5

for i=1:length(xout)

```

```
104     if yout(i)>2*sigma_Y*(xout(i)-0.5) %se ho almeno un valore che cade
            sopra la retta 0.5
105         NumA=NumA+1;
106     end
107
108     if yout(i)<2*sigma_Y*(xout(i)-0.5) %se ho almeno un valore che cade
            sotto la retta 0.5
109         NumB=NumB+1;
110     end
111
112     if yout(i)<2*sigma_Y*(xout(i)-0.2) && yout(i)>2*sigma_Y*(xout(i)-0.5)
113         Num0205=Num0205+1;
114     end
115
116 end
117
118 %% FITTING IN BASE ALLA NUMEROSIT  DEI PUNTI
119 if NumA>=1 && NumB>=1  %stesso identico modo di procedere del successivo
        !!!!
120 [JQ,xout,yfit,C2] = FitJinRegionAB(X,Y,Jlim, sigma_Y,N,SUP,xout,yout,X0,X1
        ,X2,X3,X4,Y0, Y1, Y2, Y3, Y4);
121
122 elseif NumA>=4 && NumB==0 && Num0205>=1 %stesso identico modo di procedere
        del precedente!!!!
123 [JQ,xout,yfit,C2] = FitJinRegionAB(X,Y,Jlim, sigma_Y,N,SUP,xout,yout,X0,X1
        ,X2,X3,X4,Y0, Y1, Y2, Y3, Y4);
124
125 else
126     NoFitJRegionA(X,Y,Jlim, sigma_Y,N,SUP,xout,yout,X0,X1,X2,X3,X4,Y0, Y1,
            Y2, Y3, Y4)
127
128     'LEGGERE ASTM 1820-21 A PG. 29  A9 .8, andare a fare riferimento come
            scritto alla AnnexA6 di pg 25'
129
130     JQ=NaN;
131     xout=NaN;
132     yfit=NaN;
133
134 end
135
136 end
```

Listing B.4: Codice MATLAB di esempio

Estimation of J_Q

```
1
2     function [JQ,xout,yfit,C2] = JfitJQ3_DCPD(X,Y,Jlim, sigma_Y)
3 % JfitJQ3 => fitta i valori di Delta_a vs J per stimare il JQ
4 %         => rappresentazione grafica dei risultati e delle aree di
5 %            validit  dei punti da prendere per il fitting
```

```
%       =>=>IMP: utilizzo delle sotto funzioni per fare il fitting (FitJinRegionAB).
%               necessario vedere dove cadono e quanti sono i punti nelle
%            regioni A e B (ASTM 1820  A9 .6.4 e ss.) <=<=
%
% INPUT => X: valori sperimentali su asse x (=delta a(i))
%          Y: valori sperimentali su asse y (=J(i))
%          Jlim valore di Jlimite superiore
%          sigma_Y: sigma calcolato prima (media artimetica fra rottura e
%                   snervamento)
%
% OUTPUT => JQ: valore di JQ stimato dalla regressione con il fitting
%           xout: valori di Delta_a che cadono nella regione di qualificated Data*
%           yfit: valori di J fittati che cadono nella regione di qualificated Data*
%-------------------------------------------------
% (*) definita secondo norma, il fitting    fatto secondo la norma
%     norma di riferimeto ASTM E1820-21 [ A9 .6 pg 27-28]


%% COSTRUZIONE DELLE RETTE E NUMEROSIT  DEI PUNTI
% Individuo i punti che stanno fra le due rette (offset 0.15 e 1.5 di
% costruction line) con metodo dei punti che stanno sotto la prima retta e sopra
% la seconda retta

N=length(Y); %numero di cili

%Definisco le linee di costruzione per delimitare la regione di
%qualificazione dei dati (due rette oblique e retta orizzontale)

%Costruction Line "base" => servono per plottare le altre
X0=[0,X(N)]; %coord Costruction line da norma passa per zero
Y0=[2*sigma_Y*0, 2*sigma_Y*X(N)]; %coord Costruction line da norma passa per zero

%Construction Line traslata di 0.15
X1=[0+0.15; X(N)+0.15]; %coord x spostate di 0.15 (da norma) della 1 retta di esclusione X==delta a
Y1=[0, 2*sigma_Y*X(N)]; %coord y della  1   retta di esclusione Y== J
                                    % le coordinate del valore della y
                                    % sono date dalla Costruntion Line da
                                    % norma

%Construction Line traslata di 0.2 (per fittare ilvalore di JQ con
%                                  regressione del fitting)
X3=[0+0.2;X(N)+0.2]; %coord x spostate di0.2 (da norma) della 1   retta di esclusione X==delta a
Y3=[0, 2*sigma_Y*X(N)]; %coord y della  1   retta di esclusione Y== J
                                    % le coordinate del valore della y
                                    % sono date dalla Costruntion Line da
                                    % norma

```

```
%Construction Line traslata di 1.5
X2=[0+1.5;X(N)+1.5]; %coord x spostate di 1.5 (da norma) della 2   retta
     di esclusione
Y2=[0, 2*sigma_Y*X(N)];%coord  della 2   retta di esclusione

%Construction Line traslata di 0.5 Line for region A and B
X4=[0+0.5;X(N)+0.5]; %coord x spostate di 1.5 (da norma) della 2   retta
     di esclusione
Y4=[0, 2*sigma_Y*X(N)];%coord  della 2   retta di esclusione

%Linea orizzontale superiore di Jlimite
SUP=[0,Jlim;
     X(N),Jlim]; %coord della retta orizzontaledi Jlim superiore


%Controllo che i valori di J sperimentali cadano fra le due rette oblique
     e
%sotto la retta orizzontale e butto gli altri valori (il fitting viene
%fatto solo su quelli)

for i=1:length(X)

   if Y(i)<Jlim %sotto retta orizzontale

          if Y(i)<2*sigma_Y*(X(i)-0.15) && Y(i)>2*sigma_Y*(X(i)-1.5) %fra
               rette oblique
                xoo(i)=X(i); %riporto il valore di Delta_a
                yoo(i)=Y(i); %riporto il valore di J
          else
                xoo(i)=NaN; %lascio NaN
                yoo(i)=NaN; %lascio NaN
          end

   else
     xoo(i)=NaN; %lascio NaN
     yoo(i)=NaN; %lascio NaN
   end

end

%tolgo i NaN
xout=xoo(~isnan(xoo)); %Delta_a che cadono fra le due retta e sotto la
     orizzontale Jlim
yout=yoo(~isnan(yoo)); %J che cadono fra le due retta e sotto la
     orizzontale Jlim

%VERIFICA DELLA NUMEROSIT  DEI PUNTI NELLE REGIONI
%Verifico che ci sia almeno un punto nella A region e nella B region (A
%region fra 0.15 e 0.5 lines e B region fra 0.5 e 1.5 lines)
% La retta passante per 0.5 ha eq. y=2*sigma_Y*(x-0.5)

NumA=0; %contatore numeri in A region
NumB=0; %contatore numeri in B region
Num0205=0; %contatore numeri fra lelinne di 0.2 e 0.5
```

```
101
102 for i=1:length(xout)
103
104     if yout(i)>2*sigma_Y*(xout(i)-0.5) %se ho almeno un valore che cade
            sopra la retta 0.5
105         NumA=NumA+1;
106     end
107
108     if yout(i)<2*sigma_Y*(xout(i)-0.5) %se ho almeno un valore che cade
            sotto la retta 0.5
109         NumB=NumB+1;
110     end
111
112     if yout(i)<2*sigma_Y*(xout(i)-0.2) && yout(i)>2*sigma_Y*(xout(i)-0.5)
113         Num0205=Num0205+1;
114     end
115
116 end
117
118 %% FITTING IN BASE ALLA NUMEROSIT  DEI PUNTI
119 if NumA>=1 && NumB>=1  %stesso identico modo di procedere del successivo
        !!!!
120 [JQ,xout,yfit,C2] = FitJinRegionAB(X,Y,Jlim, sigma_Y,N,SUP,xout,yout,X0,X1
        ,X2,X3,X4,Y0, Y1, Y2, Y3, Y4);
121
122 elseif NumA>=4 && NumB==0 && Num0205>=1 %stesso identico modo di procedere
        del precedente!!!!
123 [JQ,xout,yfit,C2] = FitJinRegionAB(X,Y,Jlim, sigma_Y,N,SUP,xout,yout,X0,X1
        ,X2,X3,X4,Y0, Y1, Y2, Y3, Y4);
124
125 else
126     NoFitJRegionA(X,Y,Jlim, sigma_Y,N,SUP,xout,yout,X0,X1,X2,X3,X4,Y0, Y1,
            Y2, Y3, Y4)
127
128     'LEGGERE ASTM 1820-21 A PG. 29  A9 .8, andare a fare riferimento come
            scritto alla AnnexA6 di pg 25'
129
130     JQ=NaN;
131     xout=NaN;
132     yfit=NaN;
133
134 end
135
136
137
138
139 end
```

Listing B.5: Codice MATLAB di esempio